

FMH606 Master's Thesis 2021

Process technology

# **Experimental investigation of artificial snow production in marginal geographic conditions**



Malene Nordbø

Faculty of Technology, Natural sciences and Maritime Sciences  
Campus Porsgrunn

**Course:** FMH606 Master's Thesis, 2021

**Title:** Experimental investigation of artificial snow production in marginal geographic conditions

**Number of pages:** 104

**Keywords:** Artificial snow production, nozzle theory, droplet model, experimental setup, image processing

**Student:** Malene Nordbø

**Supervisor:** Joachim Lundberg

**External partner:** Inventor Odd Ivar Lindløv

**Summary:**

This work aimed to perform both literature and experimental study of artificial snow production in marginal geographic conditions. The principal behind artificial snow formation is water which is discharged as a spray to cold air and becomes an agglomerate of frozen droplets. A snow-producing rig designed by a Norwegian developer was used to investigate the artificial snow production process. The innovative part of the snow-producing rig was a novel twin-fluid external annular sheet nozzle that enhances droplet breakup at low water and air pressure. A theoretical model was developed to analyze the trajectory and heat and mass balance of a single droplet discharged from the nozzle. One of the experiments performed during the project, resulted in 32 kg of 490 kg/m<sup>3</sup> density snow with a time interval of 1.5 h, which satisfied the goal density of 500 kg/m<sup>3</sup>. The snow was produced at low water and air pressure compared to existing technology. In addition, image processing was performed to analyze the size and velocity of the droplets in the spray by converting a high-speed camera recording into a MatLab code. The experimental measurements were further used to confirm the validity of the theoretical droplet model.

# Preface

A Norwegian inventor has developed a system for generating artificial snow with a novel twin-fluid external annular sheet nozzle. This project aimed to perform a literature study on artificial snow production and run experiments to verify the theory found.

The University of South-Eastern Norway, the Faculty of Technology, Natural Sciences, and Maritime Sciences at Campus Porsgrunn, gave the master thesis in cooperation with an external partner Odd Ivar Lindløv.

I want to thank my professor Joachim Lundberg for his excellent supervision and support. He has been available day and night during the project and used several hours to make the experiment work out. I am also very grateful for his assistance on teams and weekly meetings.

I would also like to thank the developer of the snow production rig and the nozzle, Odd Ivar Lindløv. He used several hours and sources to develop the snow production rig and sent equipment needed during the project. He has been available on teams, phone, and mail at all times. Besides, he supervised me during formal meetings.

Further, I would like to thank Øyvind Larsen for letting me use the machine hall at the university and belonging equipment. The IT support at campus Porsgrunn does also deserves a thank for helping me install SolidWorks.

Finally, I would like to thank my family members, André, Trude, Mona, and Ottar. This task and its results would not be possible to submit without their help and assistance with the experiments.

Porsgrunn, 19.05.2021

Malene Nordbø

# Contents

Preface .....	3
Contents.....	4
Nomenclature .....	6
<b>1 Introduction .....</b>	<b>12</b>
1.1 Background .....	12
1.2 Scope of this work .....	12
1.3 Challenges and limitations .....	12
1.4 Organization of thesis .....	13
<b>2 Literature study .....</b>	<b>14</b>
2.1 Water cycle .....	14
2.2 Natural snow .....	18
2.3 Artificial snow .....	20
2.3.1 <i>Snow quality</i> .....	22
2.3.2 <i>Previous studies</i> .....	23
2.4 Nedsnødd artificial snow system .....	24
2.5 Nozzle theory .....	25
2.5.1 <i>Compressible fluid</i> .....	25
2.5.2 <i>Incompressible fluid</i> .....	27
2.6 Droplet distribution.....	28
2.7 Droplet trajectory and heat transfer modes .....	29
<b>3 Experimental setup .....</b>	<b>37</b>
3.1 Experimental rig .....	37
3.2 Procedure .....	43
3.3 Image processing .....	44
3.3.1 <i>Camera setup</i> .....	44
3.3.2 <i>Photron setup</i> .....	45
3.3.3 <i>Analysis</i> .....	45
<b>4 Results .....</b>	<b>47</b>
4.1 Experimental results.....	47
4.1.1 <i>Water mass flow</i> .....	47
4.1.2 <i>Initial conditions for the airflow</i> .....	49
4.1.3 <i>Spray dimension</i> .....	50
4.1.4 <i>Droplet size, distribution, and velocity</i> .....	51
4.1.5 <i>Air and water outlet temperature</i> .....	53
4.1.6 <i>Snow shape and density</i> .....	54
4.1.7 <i>Energy consumption of the Nedsnødd nozzle</i> .....	<i>Feil! Bokmerke er ikke definert.</i>
4.2 Modeling results .....	56
4.2.1 <i>The motion of the droplets</i> .....	56
4.2.2 <i>Heat and mass transfer</i> .....	60
<b>5 Discussion .....</b>	<b>64</b>
5.1 Findings from the literature study: .....	64
5.2 Droplet size, distribution, and velocity.....	65
5.3 Heat and mass transfer .....	66

**6 Further work .....69**

**7 Conclusion .....70**

**8 References.....71**

**9 Appendices.....75**

**Appendix A .....76**

**Appendix B .....78**

**Appendix C .....82**

**Appendix D .....87**

**Appendix E .....95**

**Appendix F.....99**

**Appendix G .....101**

**Appendix H .....103**

**Appendix I.....104**

# Nomenclature

Symbol	Description	Unit
$A$	Cross-sectional area	[m <sup>2</sup> ]
$A_d$	The cross-sectional area of the droplet	[m <sup>2</sup> ]
$A_{a,n}$	Area of air channel within the nozzle	[m <sup>2</sup> ]
$A_w$	Area of water channel within the nozzle	[m <sup>2</sup> ]
$A_s$	Surface area of droplet	[m <sup>2</sup> ]
$\alpha$	Thermal diffusivity of air	[m <sup>2</sup> /s]
$\beta$	Shape parameter	[-]
$C$	Entrainment constant	[-]
$c$	Local speed of sound	[m/s]
$C_d$	Drag coefficient of the droplet	[-]
$C_p$	Specific heat capacity at constant pressure	[J/kg K]
$C_{p,a}$	Specific heat capacity of air	[J/kg K]
$C_{p,d}$	Specific heat capacity of water	[J/kg K]
$C_{p,e}$	Specific heat capacity of entrained air	[J/kg K]
$C_v$	Specific heat capacity at constant volume	[J/kg K]
$D$	Diameter of droplet	[m]
$D_i$	Size range	[m]
$D_0$	Initial droplet diameter	[m]
$D_{ab}$	Binary diffusion coefficient of air-water vapour	[m <sup>2</sup> /s]
$D_{max}$	Maximum droplet diameter	[m]
$D_{min}$	Minimum droplet diameter	[m]
$d_t$	Diameter of the buffer tank	[m]
$D_{v,f}$	Binary diffusion coefficient of vapor-fluid	[m <sup>2</sup> /s]
$D_{wn}$	Nozzle diameter of water sheet	[m]

## Nomenclature

$d_{10}$	Arithmetic mean diameter	[m]
$d_{32}$	Sauter mean diameter	[m]
$E$	Entrained mass	[kg/s]
$\epsilon$	Ratio of molecular weight of water vapor and dry air	[-]
$\vec{F}_b$	Boyancy force	[N]
$\vec{F}_D$	Drag force	[N]
$\vec{F}_g$	Gravity force	[N]
$F_{tot,x}$	Summation of forces acting in the x-direction	[N]
$F_{tot,y}$	Summation of forces acting in the y-direction	[N]
$g$	Gravitation acceleration	[m/s <sup>2</sup> ]
$H$	Total enthalpy	[kJ]
$h$	Specific enthalpy	[kJ/kg]
$h_0$	Stagnation enthalpy	[kJ/kg]
$h_{0in}$	Influent stagnation enthalpy	[kJ/kg]
$h_{0eff}$	Effluent stagnation enthalpy	[kJ/kg]
$h_c$	Convective heat transfer coefficient of the droplet	W/m <sup>2</sup> K
$H_{vap}$	Latent heat of water	[J/kg ]
$h_t$	Level of tank	[m]
$k$	Specific heat ratio	[-]
$k_a$	Thermal conductivity of air	[W/m K]
$L_l$	Liters of leakage	[m <sup>3</sup> ]
$Ma$	Mach number	[-]
$M_a$	Molar weight of dry air	[kg/mol]
$M_w$	Molar weight of water	[kg/mol]
$m_d$	Mass of droplet	[kg]
$\dot{m}$	Mass flow	[kg/s]

Nomenclature

$\dot{m}_{a,0}$	Initial airflow	[kg/s]
$\dot{m}_{d,0}$	Initial water mass flow	[kg/s]
$\dot{m}_e$	Mass flow of entrained air	[kg/s]
$\dot{m}_{in}$	Influent mass flow	[kg/s]
$\dot{m}_{eff}$	Effluent mass flow	[kg/s]
$\dot{m}_v$	Evaporation rate	[kg/s]
$\mu_a$	Dynamic viscosity of air	[Pa s]
$\mu_0$	Reference dynamic viscosity for thermal diffusivity	[Pa s]
$N_d$	Number of droplets	[Droplets/s]
$N_i$	Number of droplets in a specific size range	[-]
$Nu$	Nusselt number of the droplet	[-]
$n_w$	Moles of water in mixed air	[Mol/s]
$n_{tot}$	Total number of moles	[Mol/s]
$\eta$	Scale parameter, mean droplet size	[m]
$\nu_a$	Kinematic viscosity of air	[m <sup>2</sup> /s]
$P$	Ambient air pressure	[Pa]
$P_a$	The pressure of dry air	[Pa]
$P_\infty$	Ambient pressure	[Pa]
$P_{a,0}$	Influent air pressure to the nozzle	[bard]
$P_{d,0}$	Influent water pressure to the nozzle	[bar]
$P_v$	Vapor pressure	[Pa]
$P_d$	Saturated vapor pressure	[Pa]
$Pr$	Prandtl number of the droplet	[-]
$P_{ref}$	Reference pressure	[Pa]
$P_{sat@T}$	Saturated vapor pressure at a specific temperature	[Pa]
$P_{satT_{mix}}$	Saturated vapor pressure at $T_{mix}$	[Pa]



## Nomenclature

$P_{satT_{a,n}}$	Saturated vapor pressure for the airflow from the nozzle at $T_{a,n}$	[Pa]
$P_b$	Backpressure	[Pa]
$P_e$	Pressure at the exit of the nozzle	[Pa]
$P_w$	The partial pressure of water	[Pa]
$P_0$	Stagnation pressure	[Pa]
$P^*$	Critical pressure	[Pa]
$\vec{p}_a$	Momentum of air	[kg m/s]
$\vec{p}_d$	Momentum of droplets or water flow	[kg m/s]
$\vec{p}_e$	Momentum of entrained air	[kg m/s]
$Q_c$	Convective heat flux	[W/m <sup>2</sup> ]
$Q_c$	Evaporative heat flux	[W/m <sup>2</sup> ]
$Q_{rev}$	Heat with reversible process	[kJ]
$q_{in}$	Influnet heat transfer per unit mass	[kJ/kg]
$q_{eff}$	Effluent heat transfer per unit mass	[kJ/kg]
$R$	Gas constant	[kJ/kg · K]
$R_a$	Gas constant of air	[kJ/kg · K]
$R_u$	Universal gas constant	[kJ/kmol · K]
$Re$	Reynolds number	[-]
$RH$	Relative humidity	[%]
$RH_0$	Initial relative humidity air	[%]
$RH_{mix}$	Relative humidity of mixed air	[%]
$r_d$	Droplet radius	[m]
$r_0$	Radius of airflow-exit at the nozzle	[m]
$r_{wi}$	Inner radius of the water channel in the nozzle	[m]
$r_{wo}$	Outer radius of the water channel in the nozzle	[m]
$\rho$	Density	[Kg/m <sup>3</sup> ]

## Nomenclature

$\rho_a$	Density of air	[Kg/m <sup>3</sup> ]
$\rho_\infty$	Density of the ambient air	[Kg/m <sup>3</sup> ]
$\rho_{mix}$	Density of the air mixture	[Kg/m <sup>3</sup> ]
$\rho_d$	Density of droplet	[Kg/m <sup>3</sup> ]
$\rho_0$	Stagnation density	[Kg/m <sup>3</sup> ]
$S$	Total Entropy	[Kj/K]
$s$	Specific entropy	[kJ/ kg K]
$Sc$	Schmidt number	[-]
$T$	Temperature	[°C]
$T_{a,n}$	Temperature of the effluent airflow out from the nozzle	[°C]
$T_\infty$	Ambient temperature	[°C]
$T_d$	Temperature of droplet	[°C]
$T_f$	Final temperature	[°C]
$T_{mix}$	Temperature of the air mixture	[°C]
$T_{ref}$	Reference temperature	[°C]
$T_{wb}$	Wet-bulb temperature	[°C]
$T_0$	Stagnation temperature	[°C]
$t$	Time	[s]
$t_t$	Time to change water level in tank	[s]
$U$	Internal energy	[kJ]
$u_{a,0}$	Initial air velocity	[m/s]
$u_d$	Droplet velocity	[m/s]
$u_{d,0}$	Initial droplet velocity	[m/s]
$u_{rx}$	Velocity of air in the x-direction	[m/s]
$u_{ry}$	Velocity of air in the y-direction	[m/s]
$u_{eff}$	Effective droplet velocity	[m/s]

Nomenclature

$u_x$	Droplet velocity in the x-direction	[m/s]
$u_{x,eff}$	Effective droplet velocity in the x-direction	[m/s]
$u_{x,w}$	Wind speed in the x-direction	[m/s]
$u_y$	Droplet velocity in the y-direction	[m/s]
$u_{y,eff}$	Effective droplet velocity in the y-direction	[m/s]
$u_{y,w}$	Wind speed in the y-direction	[m/s]
$u_{x,air}$	Velocity of mixed air in the x-direction	[m/s]
$v$	Local speed	[m/s]
$u_d$	Droplet velocity	[m/s]
$V_d$	Volume of droplet	[m <sup>3</sup> ]
$V_t$	Volume of buffer tank	[m <sup>3</sup> ]
$\dot{V}_d$	Volume flow of water or droplets	[m <sup>3</sup> /s]
$W$	Work	[kJ]
$w_{eff}$	Effluent work per unit mass	[kJ/kg]
$w_{in}$	Influent work per unit mass	[kJ/kg]
$x$	Distance in x direction	[m]
$x_d$	Quantity, specific droplet size	[-]
$x_{01}$	Initial position of nozzle in the x-direction	[m]
$x_{02}$	Initial velocity of nozzle in the x-direction	[m/s]
$y_{01}$	Initial position of nozzle in the y-direction	[m]
$y_{02}$	The initial velocity of nozzle in the y-direction	[m/s]
$y_{w,n}$	Fraction of water in the airflow from the nozzle	[-]
$y_{ent}$	Fraction of water in the ambient air	[-]
$z_{in}$	Influent elevation	[m]
$z_{eff}$	Effluent elevation	[m]

---

# 1 Introduction

## 1.1 Background

A Norwegian inventor has developed a system for generating artificial snow. The concept is to optimize snow production for geographical locations where so-called 'marginal' conditions for snow production dominate the weather picture. By producing artificial snow, liquid water is discharged as a spray to cold air and becomes an agglomerate of frozen droplets. Artificial snow production differs from natural snow because natural snow has kernel growth and several orders of magnitude longer falling times than artificial snow. Several factors affect the production of artificial snow: air temperature and humidity, water temperature and velocity, water droplet size distribution, and possible amount of nucleation kernels to enhance growth.

Existing equipment for snow production has the disadvantage of high price and tendency to produce too wet snow, often supplied with a lack of documentation of the characteristics of the spray. Existing equipment often utilizes flat fan sprays with broad droplet size distributions. In this work, By enhancing the droplet breakup, artificial snow can be produced at reduced water and air pressures, which reduced the energy consumption and ultimately the cost of the snow. An experimental rig was used to determine the suitability of this type of spray for artificial snow production.

## 1.2 Scope of this work

The scope of this work is mainly to perform a literature study of artificial snow production and perform an experimental study on snow generation with the new Nedsnødd artificial snow system in marginal conditions. In addition, a Matlab model was developed to simulate the droplets discharged from the system.

## 1.3 Challenges and limitations

As the snow production system was relatively new, the supervisor, the student, and the developer used several hours to make the snow lance run correctly. The weather conditions such as temperature, relative humidity, and wind have highly influenced each experiment. The wind velocity and direction created unforeseen disturbances of the spray among the electrical devices and measurements used during the experiment. Also, the weather period highly influenced the result of the experiments. Several cold days in series were required to obtain frost in the ground and avoid snow melting. Since the cold season in Porsgrunn was relatively short during the project, from January to February, the student had to borrow a removable snow production rig created by the developer and run tests in Kviteseid and Arabygdi, a 3 hours' drive from Porsgrunn. The accuracy of the measurement devices used for monitoring the temperature of the weather, the relative humidity, and wind velocity was lacking. As the experiment was performed a few times only, the experimental hypothesis developed could not be appropriately answered as the investigation was based on a numereous of experiments.

## 1.4 Organization of thesis

The thesis is organized as follows:

- Chapter 2, Literature study: This contains a theory about natural and artificial snow production. A theoretical model is developed based on nozzle theory, thermodynamics, fluid dynamics, and transport processes simulating the Nedsnødd system's process.
- Chapter 3, Experimental setup: This chapter present a design of the experimental rig used and its procedure. In addition, the image processing procedure and its belonging calibration are presented.
- Chapter 4, Result: This chapter presents both experimental and modeling results.
- Chapter 5, Discussion
- Chapter 6, Further work: implications for further research is suggested
- Chapter 7, Conclusion

## 2 Literature study

The artificial snow production technology was first developed in the 1940s by a mistake where Dr. Ray Ringer studied the effect of rime icing on a jet engine in Canada. He sprayed water into the front of the jet engine, which was placed in a wind tunnel. This setup was used to obtain natural conditions for rime ice development. Instead of creating rime, he received snow and had to shut down the system to remove snow. Unfortunately, Dr. Ray Ringer did not patent his system.

In 1947, Wayne Pierce and his partners Art Hunt and Dave Richey formed the company Tey Manufacturing Company of Milford selling ski designs. The company was negatively affected by a warm winter season in 1949 and had to be innovative to endure the downturn. In 1950, Wayne Pierce developed the idea of making snow by blowing water droplets through freezing air. A paint spray compressor, a nozzle, and a garden hose were used for this application and lead to a compressed-air-and-water machine. Their company installed a few of their patented snowmaking machines without success and sold their patent rights to Emhart Corporation in 1956. The compressed air-and-water snow machine had its drawbacks with noise and energy consumptions.

In 1961, Alden Hanson designed and patented a snowmaking machine considered pioneering model for the so-called snow fan machine. He used a fan, water, and nucleating agents like, for instance, dust to produce snow. Later on, several inventors have developed snow machines based on developed technology in addition to trial-and-error tests.

Today, artificial snowmaking products are available worldwide, but the theory behind technology and process is not well documented or published. For this study, datasheets from different vendors and experimental studies performed in the Austrian Alps and at NTNU have been used to understand how artificial snow production technology works. [1]

This chapter presents the formation of natural snow, existing snow production technologies, nozzle theory, droplet distribution, trajectory, and thermal analyses.

As natural snow precipitation is one step of the water cycle in nature, it was a logical topic to investigate.

### 2.1 Water cycle

Atmospheric air contains dry air and moisture. The atmospheric pressure  $P_{atm}$  is thereby the sum of the pressure of dry air  $P_a$ , and the pressure of the water vapor, which is referred to as vapor pressure  $P_v$ . These pressures are so-called partial pressures, which represent the pressure exerted by the individual gas species. The atmospheric pressure is given by Equation (2.1) and is referred to simple  $P$  in this thesis. [2, p. 146]

$$P_{atm} = P_a + P_v \quad (2.1)$$

The atmospheric pressure is assumed to be constant in this thesis, with a value of 1,01325 bara. The vapor pressure varies depending on the environmental temperature and the relative humidity  $RH$ . The relative humidity represents the ratio between the actual amount of

moisture in the air at a given temperature and the maximum amount of moisture the air can hold.

It is given in percent, where 0 is dry air, and 100 is saturated air. Saturated air is a state where the air contains the maximum amount of water vapor at a given temperature. Equation (2.2) gives the relative humidity. [2, p. 147]

$$RH = \frac{P_v}{P_{v,sat@T}} \quad (2.2)$$

The saturated vapor pressure  $P_{v,sat@T}$ , is available in already made tables or by using Buck's formula as shown in Equation (2.3) for  $T > 0$  °C and Equation (2.4) for  $T < 0$  °C. [3]

$$P_{v,sat@T} = 611.21 \cdot e^{\left(\frac{18.678 - \left(\frac{T}{234.5}\right) \cdot T}{257.14 + T}\right)} \quad (2.3)$$

$$P_{v,sat@T} = 611.15 \cdot e^{\left(\frac{23.306 - \left(\frac{T}{333.7}\right) \cdot T}{279.82 + T}\right)} \quad (2.4)$$

By combining Equation (2.2) and (2.3) or (2.4), the partial vapor pressure for a specific relative humidity can be calculated. The relation between temperature, vapor pressure, and saturated vapor pressure is essential to understand during the study of snow formation.

The criterion for phase equilibrium for liquid water exposed to the atmosphere is that the air's vapor pressure is equal to the saturation vapor pressure at a specific temperature. The criterion is given by Equation (2.5). [2, p. 147]

$$P_v = P_{sat@T} \quad (2.5)$$

From this, it can be stated that if the vapor pressure is lower than the saturation pressure of water at a specific water temperature, water is to be evaporated. Evaporation is where the liquid state is transferred to a gaseous state. The rate of evaporation is proportional to the difference between the vapor and saturated pressure. By looking at the evaporation mechanism in detail, the liquid mass has a given temperature, a measurement of the average internal energy. When water molecules have attained sufficient kinetic energy, which is equal to or higher than the enthalpy of vaporization (the latent heat of vaporization)  $h_{fg}$ , the molecules eject themselves from the water surface. [4] [2, p. 125]

The enthalpy of vaporization represents the amount of energy required to vaporize a saturated liquid unit mass at a given pressure or temperature. As the water molecules leave the water surface, the temperature of the water mass decreases until it reaches the wet-bulb temperature  $T_{wb}$ , and further the ice-bulb temperature  $T_{ib}$ . The wet and ice-bulb temperature describe the point where evaporation is equal to the heat gained from the surrounded air. [5, p. 732]

Equation (2.6) is known as the Stull formula and is used to determine the wet-bulb temperature and ice-bulb temperature for humidity between 5% and 99% and temperatures between -20°C and 50°C. [6]

$$T_{wb} = T_{\infty} \cdot \text{atan} \left[ 0,151977 \cdot (RH + 8,313659)^{\frac{1}{2}} \right] + \text{atan}(T_{\infty} + RH) - \text{arctan}(RH - 1,676331) + 0,00391838 \cdot (RH)^{\frac{3}{2}} \cdot \text{arctan}(0,023101 \cdot RH) - 4,686035 \quad (2.6)$$

The snowmaking weather chart, given in Figure 2.1 is commonly used find the optimal ambient conditons to produce snow. On the vertical line to the left, the surrounded air temperature is presented in red color. The relative humidity is presented at the horizontal line at the top with a blue color. By defining the surrounding temperature and the relative humidity, the wet-bulb temperature in black can be found. Here, the wet-bulb temperature is categorized into three groups; blue gives good snow quality, purple gives poor snow quality, and red does not result in snow. It has to be pointed out that the selection of this categorization is not well documented. [7]

Temp C	Good Snow Quality					Poor Snow Quality					No Snowmaking									
	Humidity	10%	15%	20%	25%	30%	35%	40%	45%	50%	55%	60%	65%	70%	75%	80%	85%	90%	95%	100%
-9	-12	-12	-12	-12	-12	-12	-12	-11	-11	-11	-11	-11	-11	-10	-10	-10	-10	-9	-9	-9
-8	-12	-11	-11	-11	-11	-11	-11	-10	-10	-10	-10	-9	-9	-9	-9	-9	-9	-8	-8	-8
-7	-10	-10	-10	-9	-9	-9	-9	-9	-8	-8	-8	-8	-8	-7	-7	-7	-7	-7	-7	-7
-6	-10	-9	-9	-9	-9	-9	-8	-8	-8	-8	-8	-7	-7	-7	-6	-6	-6	-6	-6	-6
-5	-9	-9	-8	-8	-8	-8	-8	-7	-7	-7	-7	-6	-6	-6	-6	-5	-5	-5	-5	-5
-4	-8	-8	-8	-8	-7	-7	-7	-7	-7	-6	-6	-6	-6	-4	-4	-4	-4	-4	-4	-4
-3	-7	-7	-7	-7	-6	-6	-6	-6	-5	-5	-5	-5	-4	-4	-4	-4	-3	-3	-3	-3
-2	-7	-7	-6	-6	-6	-6	-5	-5	-5	-4	-4	-4	-4	-3	-3	-3	-3	-3	-3	-2
-1	-6	-6	-5	-5	-4	-4	-4	-3	-3	-3	-3	-3	-2	-2	-2	-2	-2	-1	-1	-1
0	-5	-5	-4	-4	-4	-4	-3	-3	-3	-3	-2	-2	-2	-2	-1	-1	-1	-1	0	0
1	-5	-4	-4	-4	-3	-3	-3	-3	-2	-2	-2	-2	-1	-1	-1	0	0	0	0	1
2	-4	-3	-3	-3	-2	-2	-2	-1	-1	-1	-1	0	1	1	1	1	1	1	1	2
3	-3	-3	-3	-2	-2	-2	-1	-1	-1	0	0	1	1	1	1	2	2	2	2	3
4	-2	-2	-1	-1	-1	0	0	1	1	1	1	2	2	2	3	3	3	3	4	4

Figure 2.1 Snowmaking weather chart [7]

If the evaporation is again considered, the water molecules can eject themselves even if the water has reached a solid state. The phase transition from solid to vapor is known as sublimation. As water molecules eject themselves from the water surface, the water molecules are diffused into the bulk of surrounded air. Equation (2.7) was used to determine the binary diffusion coefficient of water into the air. [8, p. 867].

$$D_{v,f}(T, P) = 0,26 \times 10^{-4} \left( \frac{T}{T_{ref}} \right)^{1,5} \left( \frac{P_{ref}}{P} \right) \quad (2.7)$$

The binary diffusion coefficient is a function of the reference temperature  $T_{ref}$ , and pressure  $P_{ref}$ , which is look-up-values for the temperature and pressure to which the water is exposed. [9, p. 936]. As a result of evaporation and diffusion, the relative humidity increases. If the relative humidity reaches 100%, the vapor pressure equals the saturated vapor pressure at the specific temperature, and the air is said to be saturated. This point is called the dew point. If the temperature decreases, water vapor condenses since the air can not hold the moisture. [5, p. 729]



## Literature study

By looking at the water vapor source, it is logical that water vapor concentration decreases with altitude in the atmosphere and contributes to cloud formation. Clouds contain particles of water substances such as water drops, ice particles, or both, suspended in a fluid.

Hydrometeor is a collective name of the condensed particle of water substance in clouds.

These hydrometeors are considered cloud particles when the updraft in the cloud is strong enough to prevent them from falling. When the updraft is not strong enough to prevent falling, the hydrometeors become precipitation particles.

The clouds are classified into three types. Liquid water clouds containing liquid water particles, ice clouds containing ice particles, and mixed clouds containing both ice and water particles. [10, p. 21]

If the cloud exists in an environment that is warmer than 0°C, the cloud consists mainly of liquid water. Since water is known to transform phase from liquid to solid when the temperature is less than 0 °C, the same phenomena are expected to occur as the cloud is exposed to cold temperature. Cloud observations show that the percentage of liquid water in the cloud converts to ice as the temperature decreases. However, ice particles were not formed in the cloud immediately when the temperature dropped below 0 °C. Even if the temperature was below -12 °C, 40 % of the cloud consisted of supercooled water drops. The cloud must exist at a temperature close to – 40 °C to obtain a 100 % content of ice particles. By this, it can be concluded that clouds are supercooled at low temperatures. Supercooling is a state where the liquid is below the freezing point at standard pressure but does not solidify. Frozen water is obtained if two requirements are fulfilled. Water molecules need to have low enough energy, which is a function of temperature. Further, the water molecules have to develop intermolecular bonds between each other to hold the solid-state. [11, p. 28] [12]

Cloud particles are usually distinguished into six types based on their size. The six types are listed in Table 2.1

Table 2.1: Precipitation particles and characteristic [11, p. 30]

Type	Size range	Characteristic
<i>Cloud drops</i>	≈ 3- 400μm	Water drops suspended in the air by the updraft
<i>Raindrops</i>	≈ 400μm – 3mm	Falling water drops against the updraft
<i>Ice crystals</i>	≈ 30 – 300 μm	Crystalline ice particles of hexagonal shape
<i>Snowflakes</i>	≈ 300μm – 1cm	Crystalline ice particles fall against the updraft in a single form or as snow aggregates.
<i>Graupel</i>	5 mm	Droplets that freeze partly on the surface of a falling snow crystal are called a rim. If the droplets cover all of the surfaces of the snow crystal, it is called graupel.
<i>Hail</i>	5mm – 15 cm	Increased size of graupel

## 2.2 Natural snow

As explained, clouds contain water vapor, supercooled droplets, and ice particles if the temperature is low enough. Two types of snow can develop from such a cloud, crystal growth by freezing or by sublimation. Snow crystals formed by freezing occur when supercooled droplets in the air interfere with frozen droplets or particles and freeze instantaneously. Graupel, ice particles, and hail are examples of such snow shape development during the freezing phenomena. One illustration of rime is available in Figure 2.2. [13, p. 264]



Figure 2.2: A rimed sector plate was taken by Dr. Charles A [13, p.264].

The chemistry of water molecules is further studied to understand the sublimation phenomena. Water is a bent molecule that contains two hydrogen atoms and one oxygen atom and has a dipole moment. The oxygen has a negative partial charge, and the hydrogen atoms carry a positive partial charge. Charges with opposite signs are attached. During the aggregation, water molecules are to be orientated so that the positive charges are directed to the negative charges. A hexagonal pattern appears as a function of this orientation and bent structure, illustrated in Figure 2.3. In other words, water crystallizes in a hexagonal lattice, and it determines the shape of the ice crystals.

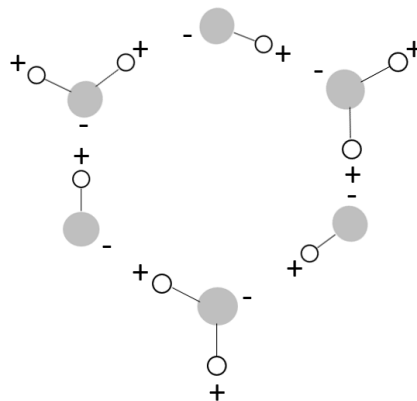



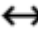


Figure 2.3: Illustrate the structure formed by water molecules [14]

## Literature study

Here, a nucleus or central point is called the substance nucleation site. At this point, the water molecules are merged and form an ice crystal structure. Ice-forming nuclei may originate from soil and clay, industrial plants, water impurities, or combustion products from the earth's surface. As the nucleus is discharged into the atmosphere, it interferes with water molecules and ultimately sticks to each other. The snowflake structure then constantly grows until it reaches a specific size. [14]

Every single snowflake grows uniquely as it is exposed to different air currents, temperatures, and humidity. In slightly warmer regions, the adhesion forces increase and ease water molecule absorption and further growth. A snowflake formed by sublimation can grow from 1 mm to 10 mm in about 20 minutes. Snow crystal shapes such as plate, stellar crystal, column, needle, dendritic, bullet and, malformed are commonly developed by sublimation. Some of the different snowflakes are listed in Table 2.2. [15, p.13]

Table 2.2: Classification of snowflakes [15, p.13]

Precipitation Particles	Shape	Place of formation	Physical process
Columns	 Prism shaped, solid or, hollow	Cloud	Growth from water vapor between -3 and -8 °C and below -30°C
Needles	 Needle shaped	Cloud	Growth from water vapor at supersaturation between -3 to -5°C and below -60°C
Plates	 Hexagonal plate-shaped	Cloud	Growth from water vapor at 0 to -3°C and -8 to -70 °C
Stellars, Dendrites	 Planar star-shaped	Cloud	Growth from water vapor at supersaturation between 0 to -3 and -12 to -16°C

In the 1930s, Ukischiro Nakaya performed a laboratory study of different snow crystal growth by controlling environmental conditions such as temperature and saturated water.

He categorized the snow crystals formed into a snow crystal morphology diagram illustrated in Figure 2.4. Here, the snow crystal is plotted as a function of temperature and supersaturation. It has to be pointed out that these snow crystals are synthetically made where the usage of nucleation seeds is not presented. [12]

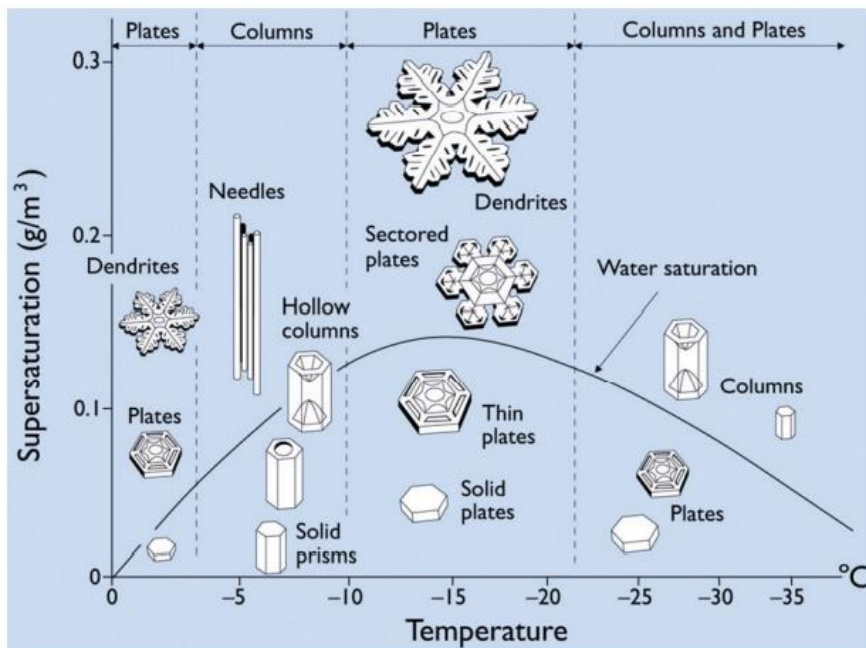


Figure 2.4: Snow crystal morphology diagram [12]

## 2.3 Artificial snow

Artificial snow production technologies are divided into two categories: temperature independent and temperature-dependent technologies. Temperature-independent technologies are based on ice crystal production. The production itself is placed inside a confined container or room. Here, water is sprayed onto cold surfaces, usually cooling elements or filled into molds. When solid ice is obtained, it is usually scraped off the surface and crushed by a grinder into powder-shaped ice. The ice shape can vary with a size range from small ice particles to 200 kg blocks.

TechnoAlpin, SnowMagic Inc, IDE Technologies Ltd, and SnowTec are examples of vendors which deliver such temperature-independent systems. The main advantage of such a system is that it is temperature independent, making the snow available during the whole year. It is also easy to control the product ice quality and quantity. The main challenges with these systems are the snow quality, transport requirements, storage requirements, and the energy consumption. NTNU and SINTEF are cooperating with federations from Norway to solve such challenges. [16] [17]

This thesis, however, focuses on temperature-dependent technology. Two types of widely used machines for this purpose are low-pressure snow fans and high-pressure lances or towers. Both types are based on the same principle; water is being atomized by forcing pressurized water through nozzles with the combination of pressurized air. The air is either generated through nozzles in lances or by a fan in snow guns. Such air generation is the main difference between the two types. It was previously stated that water might reach the supercooled phase even at a temperature near  $-40^{\circ}\text{C}$  and require some nucleators to activate the freezing process. Some artificial snow machines do thereby add some nucleation kernels to activate the snow formation process. However, such an add-in generates an extra cost for the user. Examples of a snow gun and snow lance are shown in Figure 2.5.



Figure 2.5: Snow gun to the left and snow lance to the right, produced by TechnoAlpin [18][19]

These artificial snow production systems require sufficient flight time to ensure enough heat transfer from the water to the environmental air to freeze the water. Nucleators also need to be present in synthetic or natural forms to activate the snow production process. Also, today's technology requires massive electrical and water consumption to produce snow.

### TT10 Tower Power

A company called TechnoAlpin produces both snowguns and snow lances which is shown in Figure 2.5. TT10 is a fan-based machine mounted on a tower that expands the flight time of the water droplets. The snow gun is assembled with eight nucleators, eight fixed nozzles, sixteen controllable nozzles, a power unit (compressor and turbine), and a heating element. A tilting function is implemented into the tower, which eases maintenance. The power unit requires 22 kW, and the heating element requires 1.3 kW. A water filter is also included, which removes particles larger than 250 microns. The operating water pressure is 8 to 40 bar, and the operating temperature is - 25 to + 2 °C. It is worth mentioning that the vendor did not specify the electrical consumption required to operate the pump, the required relative humidity, the snow density produced, or the nucleator consumption. [18]

### TL 8 Lance

The TL lance series is also produced by TechnoAlpin and is illustrated in Figure 2.5. A Lancehead consists of three nucleators, three fixed nozzles, and nine adjustable nozzles and is mounted on a designed pipe. The pipe consists of a fixed column and a rotating column making the lancehead easy to adjust. A cylinder is connected between the pipe and the supporting legs, making the lance easy to maintain. The operating pressure for such lance is between 20 to 60 bar, and the compressor requires 4.0 kW. At the vendors' webpage is the same lack of information as for the TT10 snow gun. The vendor has not specified the electrical consumption required to operate the pump, the required relative humidity, the snow density produced, or the nucleator consumption. [19]

## Happysnow

A company called Happysnow produces a snow lance which is developed for households. This snow gun is used to produce snow for covering gardens and decoration. The vendor claims that their snow gun produces  $0.7 \text{ m}^3$  snow per hour from below  $-4^\circ\text{C}$  ( $-2^\circ\text{C}$  dry air). A high-pressure washer is required to feed the snow gun 300 l/h of water per hour with a pressure range between 70-129 bar. Also, a compressor feeds the snow gun with 100 l/h of air. Both the compressor and the high-pressure washer require 2.6 kW to operate the snow gun. The vendor claims that snow has been produced with a water temperature of  $6^\circ\text{C}$ . There is no theory or values available at the vendor's website to evaluate the product's snow density or at which relative humidity the snow was produced. One snow lance produced by Happysnow is presented in Figure 2.6. [20]



Figure 2.6: Happysnow model [20]

### 2.3.1 Snow quality

The snow quality can be defined by measuring the density, the liquid water content (LWC), the snow hardness, and snow crystal shape.

Between 2014 and 2017, a snow quality analysis was performed during three different seasons at five different ski resorts at altitudes between 590 to 945 m in Slovakia. Snow depth and density were monitored for both natural and artificial snow by extracting samples from the piste and off-piste. From the analysis, the mean difference between the maximum and minimum density for different types of snow was found and is listed in Table 2.3. It has to be pointed out that the relative humidity was not given regarding this experiment, and the ski resorts are placed in conditions that are not marginal. Based on this analysis, the goal density for this thesis is set below  $500 \text{ kg/m}^3$ , while snow hardness and liquid water content are not considered. [21]

Table 2.3: Snow density measurements from Slovakia [21]

Snow type	Type description	Value
Ski piste snow	Groomed snow with added artificial snow	$420 \pm 87 \text{ Kg/m}^3$
Uncompacted natural snow	Uncompacted natural snow on off-piste sites	$328 \pm 80 \text{ Kg/m}^3$
New artificial snow	Maximum two-day-old machine-made snow	$273 \pm 66 \text{ Kg/m}^3$
New natural snow	Maximum two-day-old snowpack	$211 \pm 59 \text{ Kg/m}^3$

### 2.3.2 Previous studies

A few studies are available on artificial snow production topics, with a lack of the specification of snow technology used in detail or presentation of essential environmental data. Two experimental studies are presented below.

#### Journal from the Austrian Alps (2009)

A journal about the investigation of the snow production potential in the alps was published in 2009. In this journal, the weather conditions were monitored by Austrian stations placed at an altitude between 585 to 3105 meters. The relative humidity and the air temperature were measured to find the wet-bulb temperature between 1948 to 2007. In addition, the World Meteorological Organization (WMO) was used to determine the humidity. Further, an experiment was performed using snow machines to find the correlation between the relative humidity and the snow production potential. The snow production process itself is not well documented since it was not the primary purpose of the investigation but rather to find the maximum wet-bulb temperature for snow production. The snow machines used and the number of nozzles or nucleators were, however, not presented. The parameters used in this journal are given in Table 2.4. [22]

Table 2.4: Parameters from snow production potential investigation [22]

Parameter	Value
Artificial snow production technology	<i>Snow gun and fan gun</i>
Droplet diameter	<i>0.2 to 0.4 mm</i>
Water velocity	<i>&gt; 30 m/s</i>
Water temperature	<i>&gt; 2°C</i>
Water pressure for fan gun	<i>25 barg</i>
Water pressure for air-water gun	<i>25 barg &lt;</i>
The droplets traveling time	<i>10 – 15 s</i>
Mean density of produced snow	<i><math>400 \frac{\text{kg}}{\text{m}^3} (\pm 10\%)</math></i>
Maximum possible production potential at $T > -14^\circ\text{C}$	<i>Fan gun: <math>72 \text{ m}^3/\text{h}</math> Air – water: <math>51 \text{ m}^3/\text{h}</math></i>
Actual wet-bulb threshold temperature value	<i>Fan gun: <math>-1.5 \text{ to } 2^\circ\text{C}</math> Air – water: <math>-1.5 \text{ to } 2^\circ\text{C}</math></i>

## Literature study

As a result of the monitoring weather data between 1980 and 1990, the mean seasonal air and wet-bulb temperature increased between  $+1.5^{\circ}\text{C}$  and  $+3.1^{\circ}\text{C}$ . This temperature increase indicates that the global temperature is increasing and that snowmaking days are decreasing. It was also presented that the relative humidity was playing an essential role in water cooling, where the amount of cooling is directly proportional to the relative humidity. If the humidity decrease, the evaporative cooling increases which gives better snowmaking conditions. The study's author recommended that the maximum air temperature for producing snow is  $-1^{\circ}\text{C}$  with 75% relative humidity but did not specify what weather conditions resulted in the density of  $400\text{ kg/m}^3$ . [22]

### Master thesis at NTNU (2017)

One experimental study on artificial snow production was performed by the cybernetics student Odd Erlend Hansen Berg at NTNU in 2017. He intended to investigate the optimization of snow from several production units at Granåsen ski resort with an altitude of 180 m in Trondheim, which is in marginal conditions. He also wanted to evaluate how snow production influenced the local climate and developed a customized control system. The change of surrounding air temperature as a function of the distance from snowmachines was of interest.

In the cybernetics master thesis, a Northwind 450 snow fan was applied, produced by DemacLenco. The snow fan consists of four rings with 328 nozzles consuming 482 l/m of water at a pressure of 30 bar gauges, including water loss. The lake Leirsjø, nearby the ski resort, was used as a water source with a mean temperature of  $2^{\circ}\text{C}$ . A  $20\text{ }\mu\text{m}$  filter was used to prevent large particles from accumulating in the nozzles. A compressor of the type Atlas Copco SNOW-LE, a motor fan, and a heating element was used, consuming 4.0 kW, 12,5 kW, and 5kW, respectively. A weather station was used to estimate the air temperature and the relative humidity during the experiment. It was estimated that the snow gun produced 868 l/min or  $52\text{ m}^3/\text{h}$  of snow. From a test performed in March month with unknown temperature and relative humidity, the lowest density was defined to be  $811\text{-}936\text{ kg/m}^3$ . [16]

## 2.4 Nedsnødd artificial snow system

In this thesis, a nozzle system developed by the company Nedsnødd is used. The nozzle is assembled of a novel twin-fluid annular sheet nozzle consisting of an inner part, formed with a cone, an outer part, a reverse disk, and a nut as illustrated in Figure 2.7.

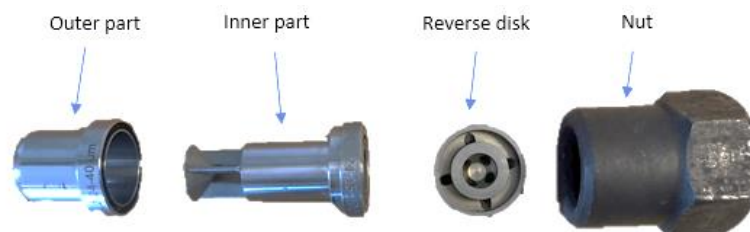


Figure 2.7: Nedsnødd nozzle assembly

The nozzle is designed in such a way that it can be implemented in lance systems. It can also be applied to a snow gun system, however, it requires some modification and supply of compressed air. The fan itself would then act as an extra air supply to increase the flight time of the water droplets.



Water flow supplied by a pump enters the reverse disk and is guided into an annular sheet with a thickness of 24-40  $\mu\text{m}$  defined by the inner and outer parts. When the water is discharged from the annular opening, the water is formed as a corresponding sheet. Pressurized airflow supplied by a compressor enters the reverse disk and is guided into the center of the inner part. It is discharged against the cone and further into the water sheet. The thin sheet of water is then atomized into tiny droplets by interference with the airflow and the cone. The cone contributes to a controlled separation of the water sheet. As the water droplets travel through the air, the droplet release heat to the surrounding air and may transform into solid ice. Some of the water may also sublimate directly from ice particles. However, the sublimation phenomena is not considered in this study.

## 2.5 Nozzle theory

As previously mentioned, snow formation is highly dependent on the air and water temperature, velocity, water droplet size distribution, air humidity, and amount of nucleation kernels. As the snow product is dependent on both initial conditions supplied by the pump and the compressor, nozzle theory is applied to understand the relation between the influent and effluent parameters of the nozzle.

A nozzle is a device that increases fluid velocity as a function of decreased pressure. The conversion is achieved by reducing the cross-sectional area in the flow direction. Figure 2.8 shows the split drawing of the Nedsnødd nozzle illustrating the water and air channel. A derivation of the correlation between the influent and effluent parameters in the nozzle is to be found. Both the compressible and incompressible fluids are considered.

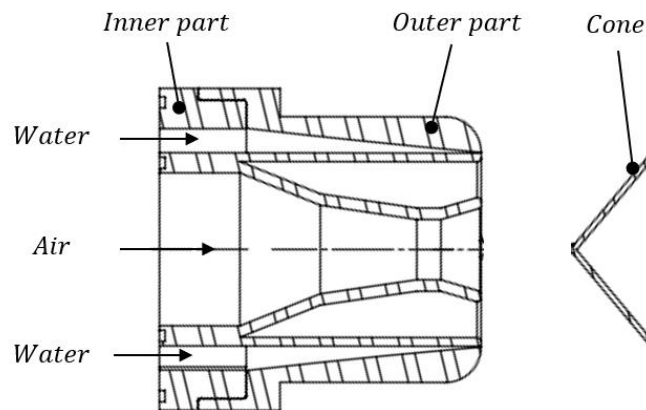


Figure 2.8: Split drawing of the Nedsnødd nozzle

### 2.5.1 Compressible fluid

For simplicity, the air channel is assumed to be designed as an isentropic converging nozzle. The compressible fluid is assumed to be ideal. The converging nozzle has a reservoir with a stagnation pressure  $P_0$ , and a stagnation temperature  $T_0$ . The cross-sectional area decreases towards the throat, which is the narrowest part of the nozzle. The pressure, temperature, and density in the throat are defined as critical properties denoted by a star \*. It is often assumed that the Mach number is equal to 1 at this point, which means that the local velocity  $v$ , of the fluid, is equal to the velocity of sound  $c$ . The Mach number describes the fluid flow regime

where the local velocity is divided by the velocity of sound in the specific fluid, as shown in Equation (2.8). [23, p. 844]

$$Ma = \frac{\text{local speed}}{\text{local speed of sound}} = \frac{v}{c} \quad (2.8)$$

Here, the velocity of sound  $c$  is calculated by Equation (2.9). This correlation is derived in Appendix B, based on the first and second law of thermodynamics and conservation of mass across a pressure wave, propagating through a fluid. [24, p. 182].

$$c = \sqrt{(kRT)_s} = v \quad (2.9)$$

Here, the specific heat ratio  $k$ , for air is 1.4, and the gas constant  $R$ , for air is 287 J/kg.K, and the  $T$  is the temperature of the gas. The subscript  $s$  represents an isentropic process where the change of entropy is zero. [25, p. 898]

As the flow passes the exit plane of the nozzle, it exhausts to a backpressure region  $P_b$ . The relation between the x-direction through the nozzle and the pressure ratio is plotted in Figure 2.9.

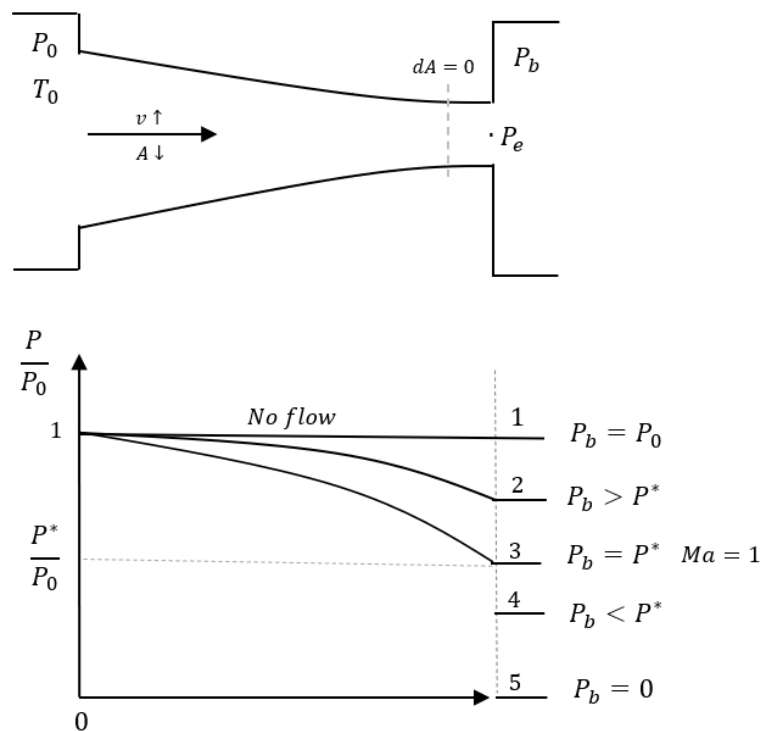


Figure 2.9: Effect of changing the backpressure in a converging nozzle [23, p. 852]

If the backpressure value at point 1 is equal to the stagnation pressure, the mass flow is zero, and the pressure along the nozzle cross-sectional area is uniform. Further, if the back pressure is reduced to  $P_2$ , the pressure at the exit is also reduced to  $P_2$ , and a pressure gradient is developed through the nozzle, which results in mass flow. The back pressure can be reduced until it equals the critical pressure  $P^*$ . At this pressure ratio, the Mach number is equal to 1, and the flow is said to be sonic or choked. If the Mach number is less or more than 1, the flow is said to be subsonic or supersonic, respectively. [23, p. 852]

To determine the effluent parameters such as airflow velocity, temperature, and pressure, the derived Equations (2.10) to (2.12) are used. These equations describe the ratio of the stagnation value to a static value. The derivation of these correlations is available in Appendix B. [23, p. 850]

$$\frac{T_0}{T} = \frac{(k-1)}{2} Ma^2 + 1 \quad (2.10)$$

$$\frac{P_0}{P} = \left[ 1 + \frac{k-1}{2} Ma^2 \right]^{\frac{k}{k-1}} \quad (2.11)$$

$$\frac{\rho_0}{\rho} = \left[ 1 + \frac{k-1}{2} Ma^2 \right]^{\frac{1}{k-1}} \quad (2.12)$$

For a steady flow, the mass flow  $\dot{m}$ , is determined by using Equation (2.13).

$$\dot{m} = \rho AV = \left( \frac{P}{RT} \right) A_{a,n} (Ma \sqrt{kRT}) \quad (2.13)$$

By solving for temperature and pressure in Equation (2.10) and (2.11) and combining Equation (2.13), the following expression in Equation (2.14) for the mass flow at any cross-sectional area within the nozzle is obtained. [23, p. 852]

$$\dot{m} = \frac{A_{a,n} Ma P_0 (Ma \sqrt{kRT_0})}{\left[ 1 + (k-1) \frac{Ma^2}{2} \right]^{\frac{(k-1)}{2(k-1)}}} \quad (2.14)$$

It can be seen from Equation (2.14) that the flow rate is regulated by adjusting the stagnation temperature or the stagnation pressure.

## 2.5.2 Incompressible fluid

The water is incompressible and can be calculated using the mass flow formula shown in Equation (2.15). [26, p. 216]

$$\dot{m}_{d,0} = \rho_d A_w u_{d,0} \quad (2.15)$$

For this fluid,  $\rho_d$ , is the density of water and the droplets,  $A_w$ , is the cross-sectional area of the water channel, and  $u_{d,0}$ , is the velocity of the water flow. The density of water is assumed to be constant throughout the nozzle. As the water is discharged through an annulus-formed area, Equation (2.16) is used. The formula is based on subtracting the area of two circles. [27]

$$A_w = \pi(r_{wo}^2 - r_{wi}^2) \quad (2.16)$$

Here,  $r_{wo}$ , is the radius of the largest circle and  $r_{wi}$ , is the radius of the smallest circle. Figure 2.10 illustrates the annulus formed area through which the water is discharged from the nozzle.

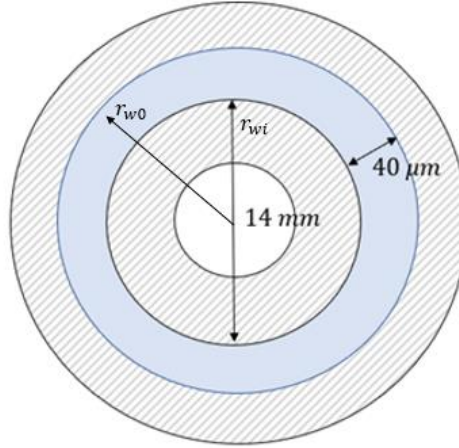


Figure 2.10: Annulus area of the water flow channel in nozzle

If the mass flow is not directly measurable, the formula for the volume flow  $\dot{V}_d$ , can be measured by using Equation (2.17). [26, p. 216]

$$\dot{V}_d = \frac{\Delta V_t}{t_t} \quad (2.17)$$

Here, the volume of water consumed  $\Delta V_t$ , may be found by measuring the change of water level  $\Delta h_t$ , within a buffer tank from which the water is supplied. The time used to obtain the volume change is  $t_t$ . If there is any leakage  $L_l$ , the following volume formula is used as shown in Equation (2.18) to include the lost water between the nozzle and the buffer tank.

$$\Delta V_t = \left(\frac{d_t}{2}\right)^2 \pi \Delta h_t - L_l \quad (2.18)$$

The mass flow of water  $\dot{m}_{d,0}$  is calculated by using Equation (2.19).

$$\dot{m} = \rho_d \dot{V}_d \quad (2.19)$$

## 2.6 Droplet distribution

Knowledge about the droplet distribution is essential when evaluating the heat and mass transfer between the dispersed droplet and the continuous phase. As the investigation of the atomization efficiency is a study of its own, the Weibull distribution (Rosin Rammler) is applied to give a rough estimate. This empirical equation has been used to characterize the powdered coal size distribution. It comes in different forms, and for this purpose, the probability density function (pdf) is used. The Weibull distribution formula is given in Equation (2.20).

$$f(x; \eta, \beta) = \frac{dF(x)}{dx} = \frac{\beta}{\eta} \left[\frac{x_d}{\eta}\right]^{\beta-1} e\left[-\left(\frac{x_d}{\eta}\right)^\beta\right] \quad (2.20)$$

In general,  $\eta$ , is a scale parameter,  $x$ , is quantity, and  $\beta$ , is called the shape parameter also known as the Weibull slope.

The probability density function is applied by changing the parameters for the droplet size distribution. Thus, the shape parameter  $\beta$ , may be defined as  $1.5 \eta$ , as the Sauter mean droplet size  $d_{32}$ , and  $x$ , represents a specific droplet size. [29, p.75]

The Sauter mean diameter is commonly applied for mass transfer and reaction calculations and is given in Equation (2.21). The numerator represents the sum of the volumes of droplets, and the denominator represents the sum of surface areas of the droplets. [30, p.17 ]

$$d_{32} = \frac{\sum N_i D_i^3}{\sum N_i D_i^2} \quad (2.21)$$

Here,  $i$ , is the size range considered,  $N_i$ , is the number of droplets in the size range and  $D_i$ , represent the middle diameter of the size range. Also, the arithmetic mean diameter  $d_{10}$ , is commonly used and represents the linear average value of all droplets in the spray and is given in Equation (2.22).

$$d_{10} = \left[ \frac{\int_{D_{min}}^{D_{max}} D \left( \frac{dN}{dD} \right) dD}{\int_{D_{min}}^{D_{max}} \left( \frac{dN}{dD} \right) dD} \right]^{0.5} \quad (2.22)$$

Here,  $D_{max}$  and  $D_{min}$  represents the maximum and minimum drop diameter, respectively. [29]

## 2.7 Droplet trajectory and heat transfer modes

The product snow is highly dependent on whether the water droplets freeze or not. As the water sheet is discharged to the atmosphere, a heat and mass transfer process begins as a function of the droplet size and velocity, the ambient temperature, and the relative humidity.

In this chapter, a theoretical model is developed to analyze the trajectory and heat and mass balance of a single droplet discharged from the nozzle. The phenomena of air entrainment and change in relative humidity in the spray are presented. A more detailed derivation of the model is available in Appendix C. Also, a developed Matlab code for executing the model is available in Appendix D.

The following assumptions are made regarding the development of the velocity expression. The spray of water is assumed to be monodispersed, where all of the droplets are uniform-sized. Also, the droplets of a specific size are assumed to have the same velocity independent of the position within the spray cross-sectional area. For simplicity, the droplet trajectory is simulated in two dimensions. Also, the collision between the droplets throughout the trajectory is neglected. The droplet is also assumed to be spherically shaped throughout the trajectory.

First, an expression for the acceleration is found by applying Newton's second law on a droplet, as shown in Figure 2.11. Here, the drag, gravity, and buoyancy forces are included.

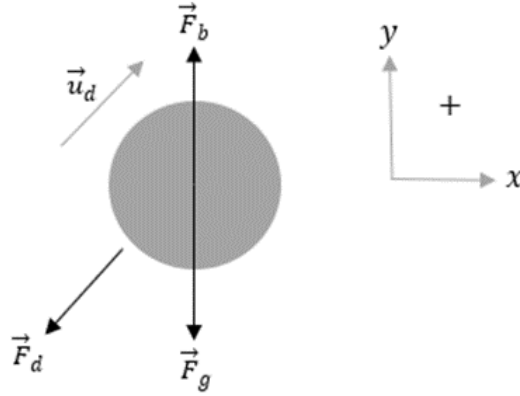


Figure 2.11: Free body diagram of a water droplet

Notice that if the drag force is equal to the gravity force, the acceleration is zero, and the terminal velocity is said to be obtained [31, p. 170]. However, the differential equations for calculating the acceleration of the droplet in x and y-direction are obtained, as shown in Equation (2.23) and (2.24). [32]

$$\frac{d^2x}{dt^2} = -\frac{3}{4} \frac{C_d}{D} \frac{\rho_{mix}}{\rho_d} \left( \frac{dx}{dt} - u_{rx} \right) \sqrt{\left( \frac{dx}{dt} - u_{rx} \right)^2 + \left( \frac{dy}{dt} - u_{ry} \right)^2} \quad (2.23)$$

$$\frac{d^2y}{dt^2} = g \left( \frac{\rho_{mix}}{\rho_d} - 1 \right) - \frac{3}{4} \frac{C_d}{D} \frac{\rho_{mix}}{\rho_d} \left( \frac{dy}{dt} - u_{ry} \right) \sqrt{\left( \frac{dx}{dt} - u_{rx} \right)^2 + \left( \frac{dy}{dt} - u_{ry} \right)^2} \quad (2.24)$$

The density of mixed air around the droplet is  $\rho_{mix}$  and  $\rho_d$ , is the density of the droplet. In this thesis, the symbols, which contain subscript  $d$ , represent the droplet and water. The droplet velocity in the x-direction  $\frac{dx}{dt}$  and y-direction  $\frac{dy}{dt}$ , is called  $u_x$  and  $u_y$ , respectively. Further, the velocity of air in the x and y-direction is represented by  $u_{rx}$  and  $u_{ry}$ .

In this paper, the air represents a mixture of entrained air from the surroundings, and air from the nozzle is denoted. The velocity of the mixed air is denoted  $u_{x,air}$ . The droplet speed is then calculated by using Equation (2.25). [32]

$$u_d = \sqrt{u_x^2 + u_y^2} \quad (2.25)$$

To determine the drag coefficient  $C_d$ , which is a function of the Reynolds number  $Re$ , the Schiller Neumann model is applied as shown in Equation (2.26). [33]

$$C_d = \begin{cases} \frac{24}{Re}, & Re \leq 1 \\ \frac{24}{Re} (1 + 0.15Re^{0.687}), & 1 < Re \leq 1000 \\ 0.44 & Re > 1000 \end{cases} \quad (2.26)$$

The last unknown term in the velocity expression is the droplet diameter  $D$ . When the droplet is discharged from the nozzle, the heat transfer influences the droplet size. In this model, convection and evaporation are considered, while conduction and radiation are neglected. It is assumed that the droplet evaporated from positive centigrades, called state 1, until it obtains  $0^\circ\text{C}$ . At state 2, the droplets are considered to be frozen at  $0^\circ\text{C}$ . Also, the temperature of the droplets is assumed to be uniform throughout the volume of the droplet. The change of uniform temperature and the heat transfer modes are illustrated in Figure 2.12.

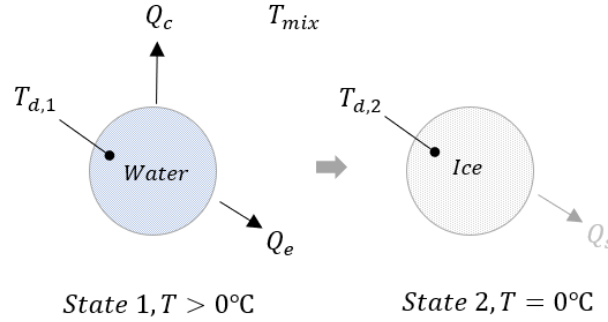


Figure 2.12: Illustrates the heat transfer modes of state 1 and 2

A premade expression is used to calculate the change of the droplet temperature, given in Equation (2.27). [32]

$$\frac{dT_d}{dt} = \left[ \frac{3\dot{m}_v}{4\pi\rho_d r_d^3} \right] T_d - \frac{3}{\rho_d c_{p,d} r_d} (Q_e + Q_c) \quad (2.27)$$

Here,  $\dot{m}_v$ , is the evaporation rate from the droplet surface to mixed air,  $Q_e$ , is evaporative of heat loss from the droplet to the mixed air and  $Q_c$ , is the convective heat loss from the surface of the droplets to the mixed air.  $r_d$ , is the droplet radius and  $c_{p,w}$ , is the specific heat capacity of water. The heat capacities for the airflow water and entrained air are assumed to be constant throughout the process. The change of the droplet diameter is calculated by using Equation (2.28).

$$\frac{dD}{dt} = - \frac{\dot{m}_v}{\rho_d \pi D^2} \quad (2.28)$$

Further, the temperature and the relative humidity of the mixed air must be determined to execute the model.

As the nozzle spray is discharged to the atmosphere, the outside flow boundary air is drawn into the main streamflow due to viscous interactions and pressure difference of the spray. This phenomenon is called air entrainment. Entrainment is an important jet flow characteristic that increases the mass flow rate in the flow direction. Different nozzle configurations and initial flow rates highly influence the mixing effect as the jet develops downstream.

Both the velocity of the spray and the outward jet spread is influenced by the entrained air, which results in different mixing effects. The mixing of the airflow from the nozzle and the surrounded air is illustrated in Figure 2.13.

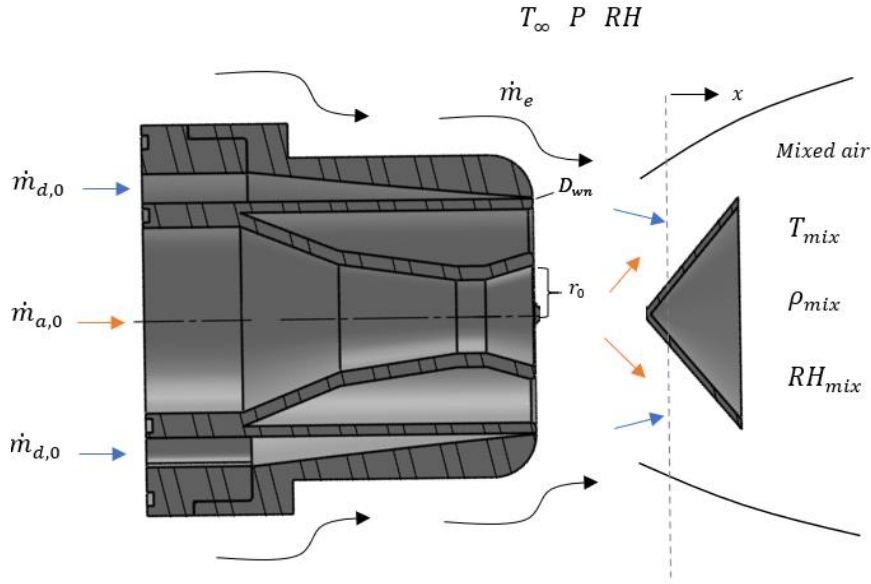


Figure 2.13: Mixture of the airflow and water flow from the Nedsnødd nozzle and entrained air

As the air entrainment develops, the more surrounded air is mixed into the spray of water droplets, which further changes relative humidity. The change of relative humidity does again influence the heat and mass transfer of the droplets. Equation (2.29) is used to find the entrained mass caused by the airflow and water flow from the nozzle. [34]

$$E = dQ(x) = C \left( \frac{\dot{m}}{D} \right) \left( \frac{\rho_\infty}{\rho_0} \right)^{0.5} dx \quad (2.29)$$

By integrating Equation (2.29) for both airflow and the water flow, the following expression shown in Equation (2.30) is obtained.

$$\dot{m}_e = C \left( \frac{\dot{m}_{a,0}}{2r_0} \right) x + C \left( \frac{\dot{m}_{d,0}}{D_{wn}} \right) \left( \frac{\rho_\infty}{\rho_d} \right)^{0.5} x \quad (2.30)$$

Here,  $\rho_\infty$ , is the density of the ambient air and  $r_0$ , is the radius of the air channel at the exit plane of the nozzle. Further,  $D_{wn}$ , is the nozzle diameter of the water sheet at the exit plane of the nozzle and  $\dot{m}_{a,0}$  and  $\dot{m}_{d,0}$  represents the mass flow of both the air and water discharged from the nozzle. The density of the air from the nozzle and the surrounded air is assumed to be equal. Also, the  $C$ , is an experimental entrainment constant based on the spray discharged from a nozzle with a specific geometry. The entrainment constant is usually defined between 0.3-0.4 for both gas and water jets based on the nozzle geometry. [34]

The average velocity of the mixed air is further calculated by simply applying the momentum balance shown in Equation (2.31) and Equation (2.32). [35, p. 273]

$$\vec{p}_a + \vec{p}_d = \vec{p}_a + \vec{p}_d + \vec{p}_e \quad (2.31)$$

$$\dot{m}_{a,0} \vec{u}_{a,0} + \dot{m}_{d,0} \vec{u}_{d,0} = \dot{m}_{a,0} \vec{u}_{x,air} + \dot{m}_d \vec{u}_d + \dot{m}_e \vec{u}_{x,air} \quad (2.32)$$



In Equation (2.29), the terms to the left represent the initial momentum of the air, and the water flow discharged from the nozzle. On the right-hand side of the equation, the momentum of the water flow, airflow, and air-entrained are presented. The average velocity of the air,  $\bar{u}_{x,air}$ , is then calculated using Equation (2.33).

$$u_{xair} = \frac{\dot{m}_{d,0}u_{d,0} + \dot{m}_{a,0}u_{a,0} - \dot{m}_{d,0}u_d}{\dot{m}_{a,0} + \dot{m}_e} \quad (2.33)$$

As the mixed air moves with a step change  $dx$  away from the nozzle, the relative humidity, and temperature of the mixed air changes. Relative humidity described in Chapter 2.1 is written for the air mixture as shown in Equation (2.34). Condensation is not taken into account.

$$RH_{mix} = \frac{P_w}{P_{v,sat@T_{mix}}} 100\% \quad (2.34)$$

Here, the partial vapor pressure of water  $P_w$ , is found by Equation (2.35).

$$P_w = \frac{n_w}{n_{tot}} P \quad (2.35)$$

Further, the total number of moles  $n_{tot}$ , in the flow is estimated by Equation (2.36).

$$n_{tot} = \frac{\dot{m}_{air,0} + \dot{m}_e}{M_{air}} + n_w \quad (2.36)$$

The moles of water,  $n_w$ , in the airflow from the nozzle, the entrained air and the water droplets are determined by Equation (2.37). The molar weight of the air is assumed to be constant. [2, p.127]

$$n_w = \frac{\dot{m}_{air,0}}{M_{air} \cdot y_{w,n}} + \frac{\dot{m}_e}{M_{air} \cdot y_{ent}} + N_d \left( \rho_d \frac{3}{4} \pi \frac{\left(\frac{D_0}{2}\right)^3 - \left(\frac{D}{2}\right)^3}{M_w} \right) \quad (2.37)$$

The last term in Equation (2.34) represents the number of water molecules evaporated into the air mixture. To find the total number of droplets  $N_d$ , Equation (2.38) is used. [2, p.136]

$$N_d = \frac{\dot{m}_{d,0}}{\rho_d V_d} \quad (2.38)$$

Further, the fraction of the water in the airflow from the nozzle,  $y_{w,n}$ , is estimated by using Equation (2.39).

$$y_{w,n} = \frac{P_{v,sat@T_{a,n}}}{P} \quad (2.39)$$

Equation (2.3) and (2.4) are used to determine the partial vapor pressure at the airflow temperature from the nozzle. The water fraction in the entrained air  $y_{ent}$ , is determined. It is assumed that the entrained air had the same temperature as the ambient temperature  $T_\infty$ . [2, p.150]

$$y_{ent} = \frac{P_{v,sat@T_\infty} RH_0}{P} \frac{1}{100} \quad (2.40)$$

The only missing unknown left is the temperature and density of the mixed spray and the entrained air. The heat transferred from the droplet to the mixed air was not taken into account. First, Newton's first law of thermodynamics is applied for a closed system presented in Equation (2.41). [36, p. 27]

$$U = Q - W \quad (2.41)$$

It is assumed that no heat is transferred from the mixed air to the surroundings, which gives the following expression.

$$U = -W \quad (2.42)$$

The formula for enthalpy is shown in Equation (2.43).

$$U + PV = H \quad (2.43)$$

At constant pressure, the enthalpy for the ideal mixture is calculated by Equation (2.44). [36, p. 42]

$$\Delta H = \dot{m} C_p dT \quad (2.44)$$

The following expression in Equation (2.45), solved the enthalpy of an ideal gas.

$$\dot{m}_{air,0} \cdot C_{p,a}(T_{mix} - T_{air,0}) - \dot{m}_e C_{p,e}(T_{mix} - T_{ent}) = 0 \quad (2.45)$$

The mixing temperature  $T_{mix}$ , is further isolated as shown in Equation (2.46). The specific heat of the entrained  $C_{p,ent}$ , air and air  $C_{p,a}$ , is assumed to be constant and equal.

$$T_{mix} = \frac{\dot{m}_{air,0} \cdot C_{p,a}(T_n + 273.15) + \dot{m}_e \cdot C_{p,a}(T_a + 273.15)}{C_{p,a}(\dot{m}_e + \dot{m}_{air,0})} - 273.15 \text{ K} \quad (2.46)$$

Finally, the mixture's density is calculated for an ideal gas, given in Equation (2.47).

$$\rho_{mix} = \frac{P_\infty}{R_a} (T_{mix} + 273.15) \quad (2.47)$$

The model developed to simulate the droplet's trajectory, change in temperature and diameter with a given time, required initial conditions.

The model is executed in Matlab using the constants and initial conditions summarized in Table 2.5. These initial conditions are either measured during the experiments or determined in Appendix C. The Matlab code is available in Appendix D.

Table 2.5: Constants, initial conditions, and differential equations used in the model

Constant	Value	Units	References
$C_{p,a}$	1.005	[J/kg · K]	[25]
$C_{p,d}$	4180	[J/kg · K]	[25]
$C$	3.6	[-]	Defined
$g$	9.81	[m/s <sup>2</sup> ]	[25]
$H_{vap}$	$22.6 \cdot 10^5$	[J/kg]	[25]
$k_a$	$8 \cdot 10^{-5} \cdot T_{mix} + 0.0244$	[W/mK]	[32]
$M_a$	0.02896	[kg/mol]	[25]
$M_w$	0.018	[kg/mol]	[25]
$\mu_0$	$1.8325 \cdot 10^{-5}$	[Pa · s]	[32]
$P$	101325	[Pa]	[25]
$R_a$	0.287	[J/kg K]	[25]
$R_u$	8.3144	[J/mol · K]	[25]
$RH_0$	79	[-]	Measured
$\rho_d$	1000	[Kg/m <sup>3</sup> ]	[25]
$T_\infty$	-3	[°C]	Measured
$T_o$	296.16	[K]	[32]
$T_f$	0	[°C]	Defined
$T_{a,n}$	-37.19	[°C]	Equation (2.10)
$\nu_a$	$1/(80711.7 - 766.15)T_{mix}$	[m <sup>2</sup> /s]	[32]
<i>Initial conditions</i>			
$P_{a,0}$	1.94	[barg]	Measured
$\dot{m}_{a,0}$	$4.983e - 3$	[kg/s]	Equation (2.13)
$u_{a0}$	307.9	[m/s]	Equation (2.9)
$P_{d,0}$	4.65	[barg]	Measured
$T_0$	1	[°C]	Measured
$\dot{m}_{d,0}$	0.0166	[kg/s]	Equation (2.15)
$u_{d,0}$	9.43	[m/s]	Equation (2.15)
$\theta_a$	50	[°]	Nozzle geometry
$\theta_n$	50	[°]	Nozzle geometry
$x_{01}$	0	[m]	Defined
$x_{02}$	$u_{d0}$	[m/s]	Defined
$y_{01}$	1.324	[m]	Measured
$y_{02}$	0	[m/s]	Defined
$r_0$	0.0105/2	[m]	Nozzle geometry
$D_0$	40, 50, 120, 170 and 360 $\mu\text{m}$	[m]	Defined
$t$	30	[s]	Defined

The differential equations used in the trajectory and heat transfer modes -model are listed in Table 2.6.

Table 2.6: Differential equations used [32]

---

*Differential equations solved in the model*

---

$$\frac{d^2x}{dt^2} = -\frac{3}{4} \frac{C_d}{D} \frac{\rho_{mix}}{\rho_d} \left( \frac{dx}{dt} - u_{rx} \right) \sqrt{\left( \frac{dx}{dt} - u_{rx} \right)^2 + \left( \frac{dy}{dt} - u_{ry} \right)^2} \quad (2.23)$$

$$\frac{d^2y}{dt^2} = g \left( \frac{\rho_{mix}}{\rho_d} - 1 \right) - \frac{3}{4} \frac{C_d}{D} \frac{\rho_{mix}}{\rho_d} \left( \frac{dy}{dt} - u_{ry} \right) \sqrt{\left( \frac{dx}{dt} - u_{rx} \right)^2 + \left( \frac{dy}{dt} - u_{ry} \right)^2} \quad (2.24)$$

$$\frac{dT_d}{dt} = \left[ \frac{3\dot{m}_v}{4\pi\rho_d r_d^3} \right] T_d - \frac{3}{\rho_d c_{p,d} r_d} (Q_e + Q_c) \quad (2.27)$$

$$\frac{dD}{dt} = -\frac{\dot{m}_v}{\rho_d \pi D^2} \quad (2.28)$$


---

## 3 Experimental setup

In this chapter, the experimental hypothesis, equipment list, and procedures are presented. A test matrix template available in Appendix G was created to document the findings throughout the experiments.

### 3.1 Experimental rig

The Nedsnødd company created a snow-producing rig on a car trailer, making it possible to perform experiments worldwide. In short, the rig contained two aggregates, a water tank, a pump, a compressor, an electric converter, a dryer, water, and air hoses, sensors, lance, and a nozzle. The workflow of the rig is illustrated in Figure 3.1.

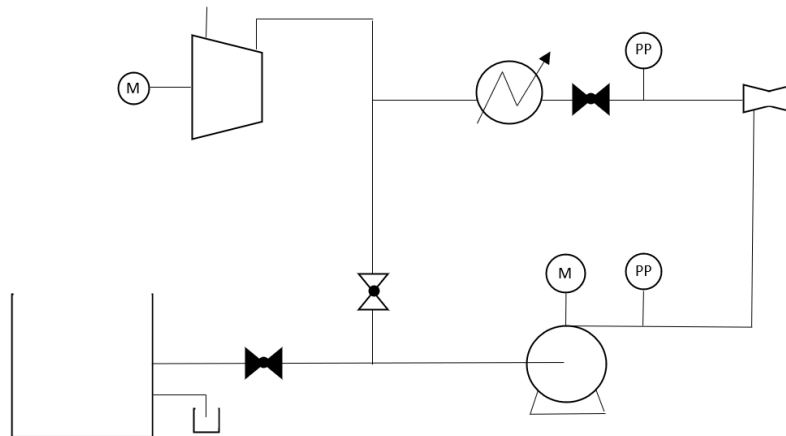


Figure 3.1: Illustration of the experimental setup in P&ID format

Compressed air was fed through a heat exchanger and further into the nozzle by an electrically driven compressor. A heat exchanger was implemented to reduce the compressed air temperature but was not used during the experiments. Further, water was pumped into the nozzle from a water tank by an electrically driven pump. Two aggregates were used as electrical feeds for the compressor, the pump, and the monitoring system. A pressure sensor was placed on both the water and air hose to monitor the nozzle's inlet conditions.

#### Centrifugal Pump

A Desmi DPVCF 2/8 B vertical centrifugal pump from Desmi was used to transport water from the buffer tank of water to the nozzle. The pump specifications are given in Table 3.1.



Figure 3.2: DESMI centrifugal pump [37]

Table 3.1: Characteristic of the DESMI Pump [37]

<i>Characteristic</i>	<i>Value</i>	<i>Unit</i>
Model key	DPVCF 2/8 B	
Installed motor power	0.55	kW
Nominal frequency	50	Hz
Optimum capacity running at a fixed velocity ( $Q^3$ ) (see fig. x Duty point)	1.86	M <sup>3</sup> /h
Optimum head running at a fixed velocity (H) (see fig. x Duty point).	47.2	m
Rotation speed indication at which Q/H are given	2900	rpm
Maximum efficiency index	53.7 % (MEI $\geq$ 0.70)	
Maximum pressure at the mentioned temperature range	PN10 – 20/+120°C	

An electrical frequency converter was connected between the aggregate and the pump motor, which made it easy to regulate the rotational pump speed. The duty point of the pump is illustrated in Figure 3.3. [37]

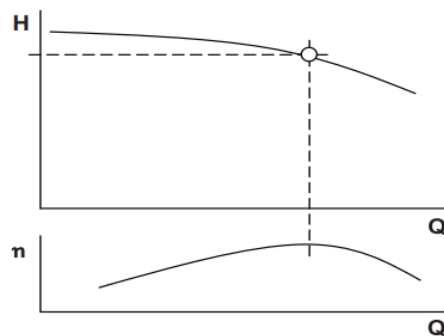


Figure 3.3: Duty point for DESMI DPVCF 2/8 B Centrifugal Pump [37]

### Piston compressor

A Luna 4.0/360 piston compressor was used to feed the nozzle with pressurized air. Some of its characteristics are given in Table 3.2. [38]



Figure 3.4: Luna 4.0/360 Piston compressor [38]

Table 3.2: Characteristics of the Luna compressor [38]

<i>Characteristic</i>	<i>Value</i>	<i>Unit</i>
Model key	21225-0203/ACB4.0-90T 400 -3	
Installed motor power	3	kW
Maximum pressure	11	Barg
Noise level	96	dB(A)
Operating temperature range	-10 - 100	°C
Max rotational speed	1450	RPM

### Pressure sensor

Pressure sensors of type Baumer PFMN-54.BC4R.C1573.41211.20001 were used to measure the influent water and air pressure into the nozzle system. This model has  $\pm 0,25$  % FS (full scale) accuracy with a pressure range of -1.0 to 20.0 bar absolute. [39]



Figure 3.5 Pressure values used in Arabygdi and Kviteseid.

### High-velocity camera and flash

Photron APX-RS was used to record the droplet size and velocity within the spray. The camera can capture 3000 frames per second at a resolution of 1024p x 1024p and 10000 frames per second at 512 x 512 pixels. Also, it has a 16 GB memory option. An advanced 10-bit CMOS sensor provides high light sensitivity with 17 $\mu$ m pixels 16.7 ms and 2 $\mu$ s global electronic shutter. Photron FASTCAM Viewer 3 application was used to control the camera. [40] [30, p.34 ]



Figure 3.6: Photron APX RS High-velocity camera [40]

The MultiLED QT was used to supply enough light to the fast-velocity camera to ensure a fully close aperture at microseconds of exposure time. It has down to 200 nanosecond strobe and delivers a lumen flux of 12 000 Lm white. Continuous lightning was used during the experiment. [41]



Figure 3.7: MultiLED QT [41]

### Lense

A Navitar 12x zoom microscope lens was applied to the high-velocity camera to capture images of the water droplets with a size of around 40  $\mu$ m. It has a zoom ratio of 12:1 and a resolution of 0.004-0.550 numerical aperture. [42] [30, p.36 ]

Numerical aperture represents angular acceptance for the light which enters the lens.[44]



Figure 3.8: Navitar 12x zoom lense [44]



### Aggregates

Two electrical sources supplied the pump, the compressor, sensors, and the camera with electricity. Gasoline generator 62760 could supply 5500/500 watts to the compressor, and another standard 230V supplied the pump, monitoring system, high-high velocity camera, and the MultiLED. It has both power outlets to 400 and 230 V (AC) and 40 V (DC). [45]



Figure 3.9: Gasoline generator 62760 [45]

### Thermographic camera

The FLIR i7 camera was used to find the temperature gradient along with the nozzle and the spray. It has a thermal accuracy of  $\pm 2^{\circ}\text{C}$  and a measurement range of  $-20$  to  $250^{\circ}\text{C}$ . The camera is illustrated in Figure 3.10. [46]



Figure 3.10: FLIR i7 [46]

### Weight scale

SF-400 Electronic Kitchen scale was used to measure the weight of the produced snow. It has an accuracy of 1 g. [47]

### Laser level

Bosh GLL 3-80P Professional was used to position the high-velocity camera. It has an accuracy of  $\pm 0,2$  mm/m. [48]

Equipment list

The following list in Table 3.3 contains additional equipment that was used.

Table 3.3: Equipment list

Equipment	
Nedsnødd snow production rig	Nikon camera
Air hose	Tarpaulin
Water hose	Earmuffs
Yoga Slim 7	Safety goggles
Measuring tape	Watch
Tripod for high-velocity camera and slash	Is drill
Weather.com	Car and its thermometer
Curtain stairs	Plastic strips
Screwdriver	Straps
Towel	Battery
Fuel tank	Flash light

### 3.2 Procedure

In this subchapter, the procedure for operating the snow production rig and carrying out experiments is presented.

1. The environmental temperature, humidity, and wind velocity were measured. Also, the wet-bulb temperature was calculated using Equation (2.4)
2. The nozzle was assembled and mounted to the lance placed on the rig.
3. The high-velocity camera was installed 41 centimeters out from the nozzle tip. The MultiLED flash was placed on the opposite side of the high-velocity camera.
4. The pump, sensors, the computer, the MultiLED flash, and the high-velocity camera were connected to the mobile aggregate.
5. Both the air hose and water hose were mounted to the lance.
6. The water tank was filled to  $\frac{3}{4}$  of the tank height.
7. The valve between the water tank and the pump was opened to fill the pump. The pump casing plug was also opened to increase the water level by supplying water by a deciliter measure.
8. The pump was then started, and the mass flow of water was regulated by adjusting the electrical converter between the pump and the aggregate.
9. The compressor was started, and the valve between the compressor and the lance was opened.
10. When the effluent water from the nozzle obtained a uniform sheet, the pressure and temperature values on the sensors were noted.
11. The mass flow  $\dot{m}_{d,0}$  of water was estimated by measuring the change of the water level in the buffer tank within a specific time interval  $t_t$ . The leakage collected between the buffer tank and nozzle was subtracted from the total volume change of water. See Chapter 2.5.2.
12. A measuring tape was used to measure the total length of the spray and the width.
13. The thermographic camera was used to investigate the temperature gradient with the nozzle and spray.
14. A tarpaulin was placed below the spray to measure the amount of snow produced. After 1.5 hours, the produced snow was collected in the middle of the tarpaulin and formed like a cone. Both the diameter and the height were measured. The formula for calculating the volume of a cone was applied to find the volume produced.
15. One liter of snow was filled into a deciliter measure and placed on a precalibrated kitchen scale to find the density of the produced snow.
16. When the experiment was finished, the rig was shut down and drained.

### 3.3 Image processing

One essential investigation of this project was to estimate the droplet diameter and velocity. As already mentioned, a high-velocity camera was used for this purpose. Figure 3.11 shows one of the positions used, trying to capture the droplet motion and distribution.



Figure 3.11: Example of the high-velocity and LED light position

#### 3.3.1 Camera setup

The high-velocity camera was placed 41 cm from the nozzle's tip, 20 cm from the center of the nozzle in the z-direction and, 16 cm above the nozzle center, as illustrated in Figure 3.12. This position was used to record the droplets in the x-direction and avoid most of the back swirled droplets induced by the air entrainment. The camera was positioned by using a laser and measuring tape.

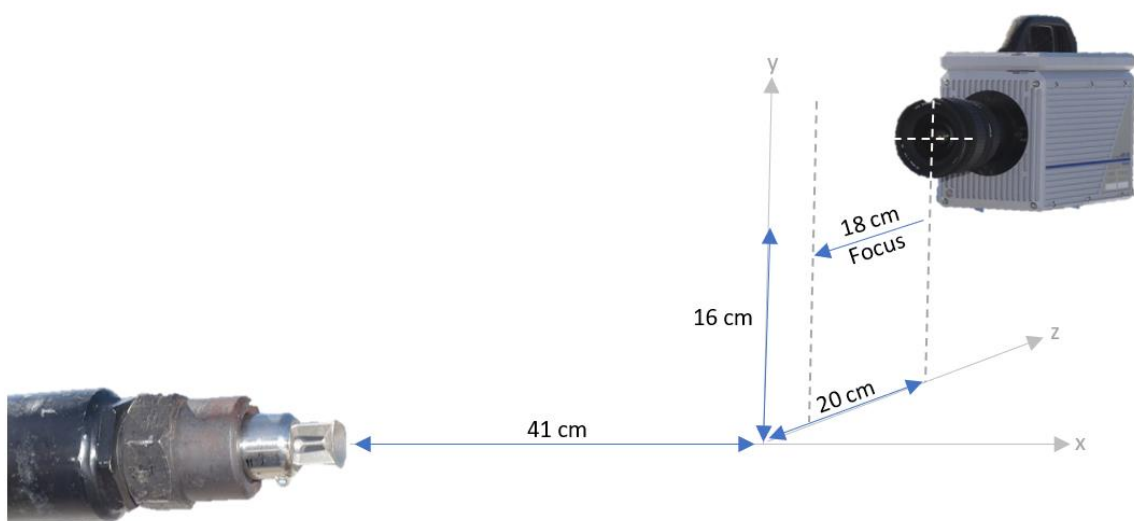


Figure 3.12: Camera setup

## Experimental setup

A Patterson globe was used for calibration and to determine a scaling of  $10,1 \mu\text{m}$  per pixel. The snapshot of the Patterson globe taken by the high-velocity camera is shown in Figure 3.13: Snapshot of the Patterson globe

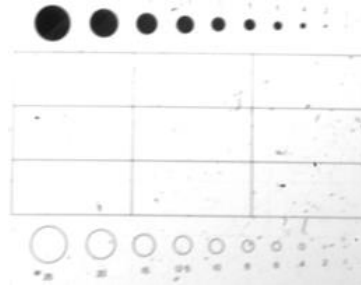


Figure 3.13: Snapshot of the Patterson globe

### 3.3.2 Photron setup

The following setup in Photron FASTCAM Viewer 3 was used to record the experiments.

Table 3.4: Photron setup

Fastcam – APX RS model 250K		
Frame rate	5000	fps
Shutter velocity	1/50000	sec
Resolution	512 x 1024	
Recording time	0.1144	s

### 3.3.3 Analysis

The video recording was imported to Photron FASTCAM Viewer 3 and analyzed. For this experiment, a recording within the time interval of 0 to 0.1144 seconds was used. After the specified time interval, recirculation of the droplets was observed. The recirculation would lead to increased residence time and is not taken into account in this thesis. A series of RAEE images were generated from the specific recording and further implemented into a pre-made MatLab code created by Joachim Lundberg. The code is available in Appendix E. Here, the droplets were manually isolated by clicking on two points on the arc of the droplets in the shadow image, as shown in Figure 3.14.

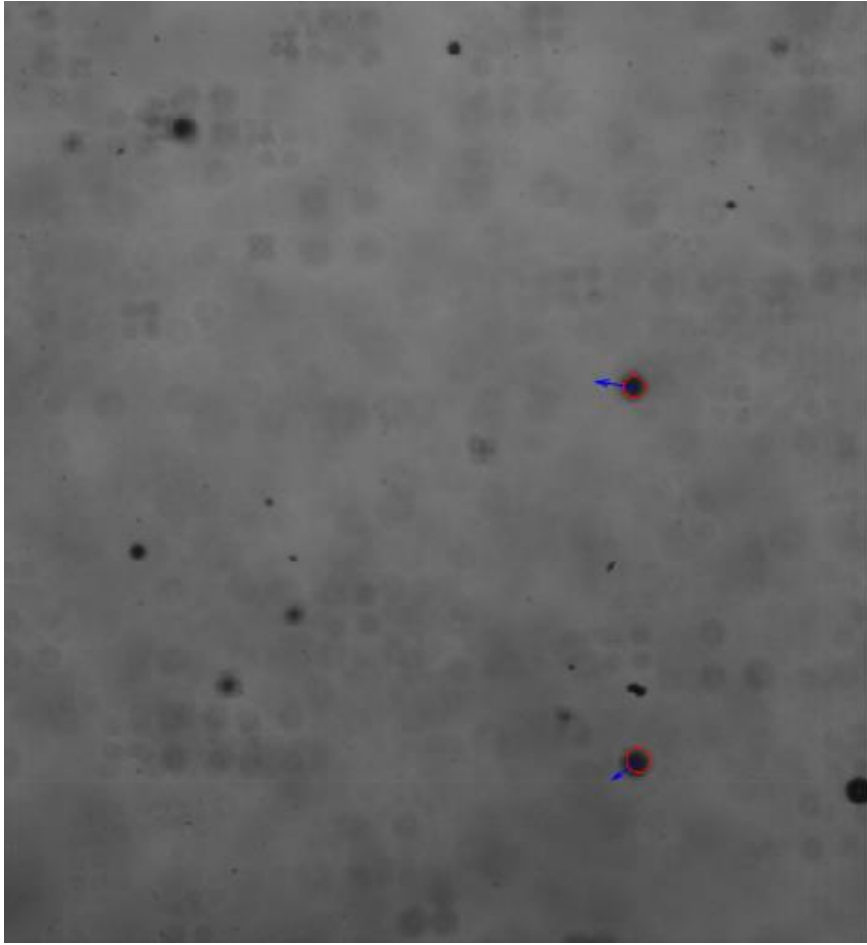


Figure 3.14: Illustration of droplet isolation during the image processing

Further, the code jumped to the subsequent frame. Here, the droplet velocity was found by clicking on the center of the same isolated droplet, which had moved a specific distance from the previous image. Only droplets that kept a clear and dark shape while passing through the screen were analyzed as they indicate a straightforward displacement compared to the droplets fading out of the camera focus. The same operation was performed for multiple droplets for several frames.

## 4 Results

In this chapter, the experimental and modeling results are presented. The data presented in the experimental results are carried out from the second experiment in Arabygdi if nothing else is specified.

### 4.1 Experimental results

Three experiments were performed during this thesis. One in Porsgrunn, one in Arabygdi, and one in Kviteseid. The only experiment yielding snow was the Arabygdi experiment performed the evening of the 18<sup>th</sup> throughout the early morning of 19<sup>th</sup> of March 2021. The ambient conditions and the pressure parameters in each experiment are given in Table 4.1.

Table 4.1: Experimental parameters

Place	<i>Porsgrunn</i>	<i>Arabygdi</i>	<i>Kviteseid</i>
Date performed	13.03.2021	18-19.03.21	21.03.2021
Altitude	7 m	687 m	307 m
Ambient temperature	- 2.6 °C	- 2,5 to - 4 °C	-1 to 1 °C
Relative Humidity	96%	79 %	64 %
Wind velocity	0-0,83 m/s	0-1,66 m/s	5 m/s
Water flow pressure	2,66 bar gauge	4.64 bar gauge	4.64 bar gauge
Water flow temperature	Assumed 10 °C	1 °C	2 °C
Airflow pressure	5.38 bar gauge	1.95 bar gauge	1.95 bar gauge
Airflow temperature	10 °C	10 °C	10 °C
Wet- bulb temperature	-3.05 °C	- 4.6 °C	-3.64 °C

#### 4.1.1 Water mass flow

The diameter of the water buffer tank was measured to be 38.8 centimeters. During a time interval of 105 s, the water level was measured to decrease by 2.0 cm. In addition, the amount of water leakage between the buffer tank and the nozzle was collected at the bottom of the snow production rig. During 105 s, the deciliter measure was filled with 6 dl water. Figure 4.1 illustrates the dimensions of the buffer tank and the volume consumed.

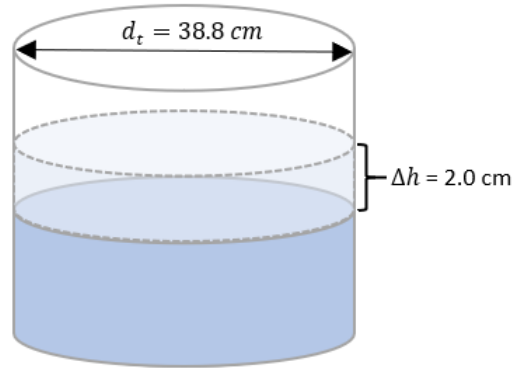


Figure 4.1: illustrates the change of water level in the water buffer tank

The volume of water consumed was determined by using Equation (2.18)

$$\Delta V_{d,0} = \pi \left( \frac{0.38}{2} \right)^2 0.02 - 0.0006 = 0.00176 m^3$$

Further, the volume of water consumed  $\dot{V}_d$ , was calculated by using Equation (2.17).

$$\dot{V}_d = \frac{0.00176}{105} = 1.68 \cdot 10^{-5} \frac{m^3}{s}$$

The mass flow of water  $\dot{m}_{d,0}$  was calculated using Equation (2.15).

$$\dot{m}_{d,0} = 1.68 \cdot 10^{-5} \cdot 1000$$

$$\dot{m}_{d,0} = 0.01664 \frac{kg}{s} \approx 60 \frac{kg}{h}$$

The water mass flow was calculated to be 60 kg/h. From this, the velocity of the water discharged from the nozzle was determined by using Equation (2.15). The water channel area in the nozzle was formed as an annulus and was calculated using Equation (2.16). The inner diameter of the nozzle was measured to be 14 mm, and the width of the sheet was 40  $\mu m$  resulting in s inner radius  $r_{wi}$ , of 7 mm, and outer diameter  $r_{wo}$ , of 7.04 mm

$$A_w = \pi ( (7.04 \cdot 10^{-3})^2 - (7 \cdot 10^{-3})^2 )$$

$$A_w = 1.764 \cdot 10^{-6} m^2$$

Further, the initial velocity of the droplet was calculated by using Equation (2.15).

$$u_{d,0} = \frac{\dot{m}_{d,0}}{\rho_d A_w}$$

$$u_{d,0} = \frac{0.01664}{1000 \cdot 1.764 \cdot 10^{-6}} = 9.43 m/s$$



#### 4.1.2 Initial conditions for the airflow

The temperature of the airflow inside the throat was determined by Equation (2.10). Here, the stagnation temperature  $T_0$  supplied by the compressor was assumed to be  $10^\circ\text{C}$ . Also, the Mach number in the throat at the nozzle exit was assumed to be 1.

$$T_{a,t} = \frac{T_0 + 273.15}{\left[\frac{k-1}{2}Ma^2 + 1\right]} - 273.15 \text{ K} \quad (2.10)$$

$$T_{a,t} = \frac{10 + 273.15}{\left[\frac{1.4-1}{2}1^2 + 1\right]} - 273.15 \text{ K} = -37.19^\circ\text{C}$$

The airflow temperature in the throat was used to calculate the velocity by using Equation (2.9)

$$u_{a,t} = \sqrt{kRT} \quad (2.9)$$

$$u_{a,t} = \sqrt{1.4(287)(-37.19 + 273.15)} = 307.9 \text{ m/s}$$

Also, the air pressure within the throat was calculated using Equation (2.11). The stagnation pressure was measured to be 2.95 bar absolute from the compressor.

$$P_{a,t} = \frac{P_0}{\left[1 + \frac{k-1}{2}Ma^2\right]^{\frac{k}{k-1}}} \quad (2.11)$$

$$P_{a,t} = \frac{2.95 \cdot 10^5}{\left[1 + \frac{1.4-1}{2}1^2\right]^{\frac{1.4}{1.4-1}}} = 1.558 \cdot 10^5 \text{ Pa}$$

By using Equation (2.13), the mass flow was determined. The diameter of the airflow channel at the throat was measured to be 3 mm.

$$\dot{m}_{a,0} = \rho AV = \left(\frac{P}{RT}\right) A_{a,n} (Ma\sqrt{kRT}) \quad (4.13)$$

$$\dot{m}_{a,0} = \left(\frac{1.558 \cdot 10^5}{287(-37.19 + 273.15)}\right) \left(\frac{0.003}{2}\right)^2 \pi(307.9)$$

$$\dot{m}_{a,0} = 4.98 \cdot \frac{10^{-3} \text{ kg}}{\text{s}} \approx 18 \text{ kg/h}$$

### 4.1.3 Spray dimension

The spray was measured to have a total length of approximately 80 centimeters, as shown in Figure 4.2. At a distance of 50 centimeters from the nozzle, the width of the spray was measured to be approximately 30 centimeters. The measurement was performed at zero wind velocity.

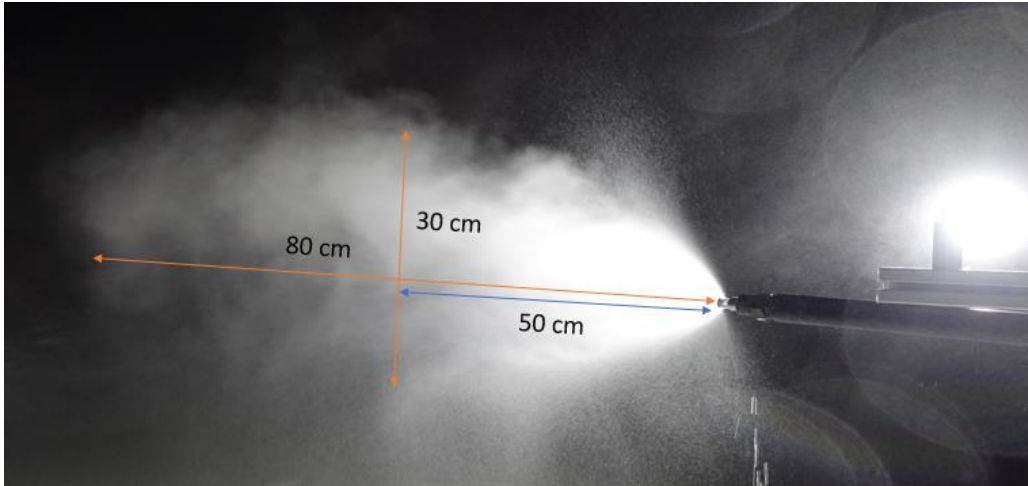


Figure 4.2: Spray dimension measurements performed in Arabygdi

The spray shapes obtained during the experiments in Porsgrunn and Arabygdi were taken, as shown in Figure 4.3 and Figure 4.4. The two sprays are a function of two different pressure settings in addition to ambient conditions, as specified in Table 4.1. The spray obtained in Porsgrunn looks purely foggy, while the spray in Arabygdi looks foggy with a tendency of generated precipitates.



Figure 4.3: Spray shape obtained during the experiment in Porsgrunn



Figure 4.4: Spray shape obtained during the experiment in Arabygdi

#### 4.1.4 Droplet size, distribution, and velocity

From the video recorded in Arabygdi, image processing was performed. Here, 77 droplets were isolated and saved into a table available in Appendix F. The uncertainty was estimated to be approximately 20% based on the shutter velocity.

The experimental droplet distribution from the image processing was found by filtering the 77 droplets based on the droplet size. In addition, the Weibull distribution was generated based on the different droplet sizes measured. Here, the shape parameter  $\beta$  was defined as 1.5. The Sauter Mean diameter of  $119 \mu\text{m}$  was used as the scale parameter  $\eta$ , generated by the premade image processing code in Appendix E. Other average data generated by the image processing code is listed in Table 4.2.

Table 4.2 Average data from the Image processing

$D_{10}$ [ $\mu\text{m}$ ]	Sauter mean $D_{32}$ [ $\mu\text{m}$ ]	Mass average velocity m/s	Direction
68,69	119,10	1,06	7,65

Both the experimental distribution and Weibull distribution was merged into a droplet distribution plot, shown in Figure 4.5.

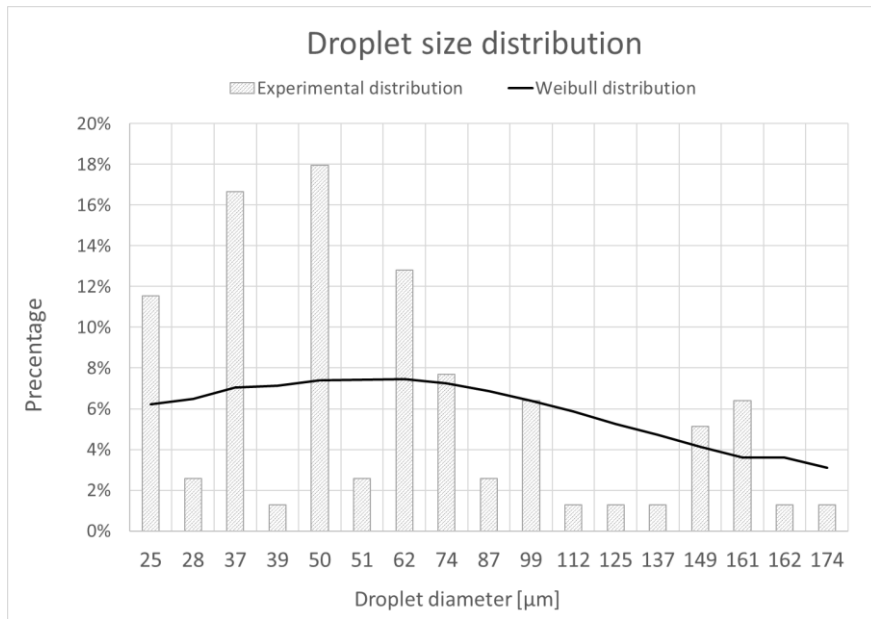


Figure 4.5: Droplet distribution comparison

In Figure 4.5, the experimental distribution is presented in the histogram, while the Weibull distribution is the continuous black curve. The experimental data and the Weibull distribution curve seem to show the same trend, however, the distribution values are not consistent. For instance, the most numerous droplet size, 50 μm, consists of 18 % and 7.4 % for the experimental Weibull distribution, respectively. The lowest counted droplet size of 174 μm was presented by 1.2 % in the experimental distribution and 3.1 % as the lowest value in the Weibull distribution.

Further, the droplet velocities measured during the image processing were plotted as shown in Figure 4.6

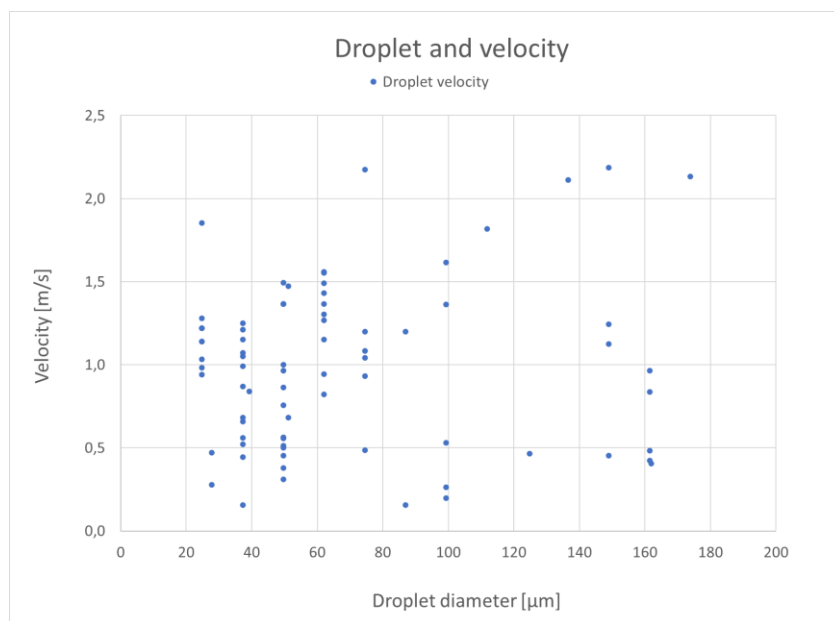


Figure 4.6: Droplet size and corresponding velocity measured in the image processing

## Results

Figure 4.6 shows that there is a significant spread in the droplet velocity for the same droplet size. For instance, the highest and lowest measured velocities for the 50  $\mu\text{m}$  droplet were 0.3 and 1.5 m/s, respectively. The median and average velocities for the same droplet size were calculated to be 0.66 m/s and 0.8 m/s.

Figure 4.7 shows the average droplet velocity as a function of droplet size. The linear trendline may indicate an increasing droplet velocity with increasing droplet size.

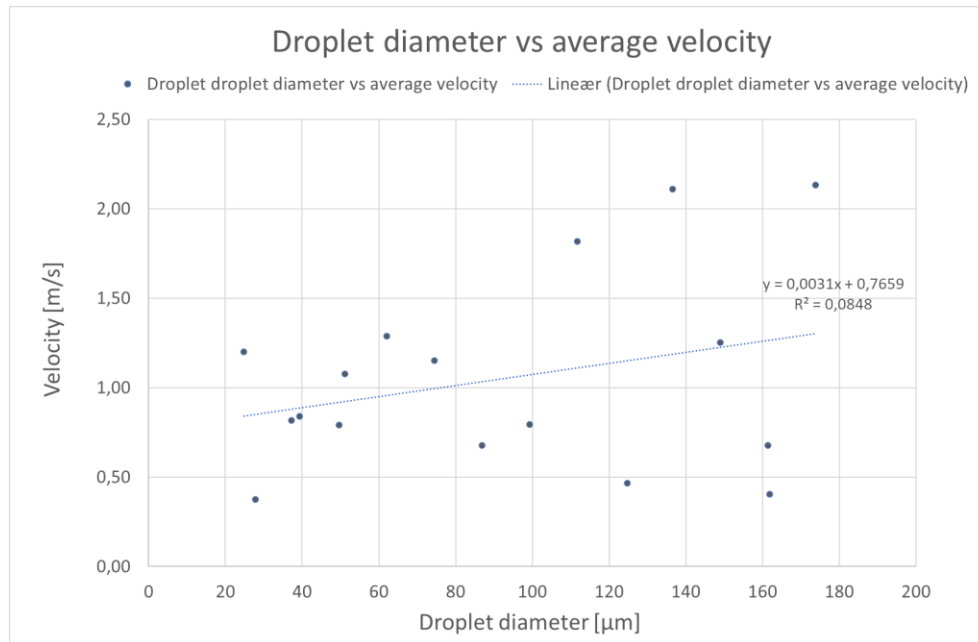


Figure 4.7: Velocity of droplets of different sizes, 41 cm away from the nozzle

### 4.1.5 Air and water outlet temperature

The temperature at the nozzle tip was measured to be  $-35.7^{\circ}\text{C}$ , as shown in Figure 4.8.



Figure 4.8: Temperature measured at nozzle tip in Arabygdi

## Results

The temperature of the water sheet, approximately 1 cm from the nozzle's exit plane, was measured to be approximately  $-1.4\text{ }^{\circ}\text{C}$ , as shown in Figure 4.9. By increasing the air pressure, ice accumulation was observed to occur between the exit plane and the nozzle cone.

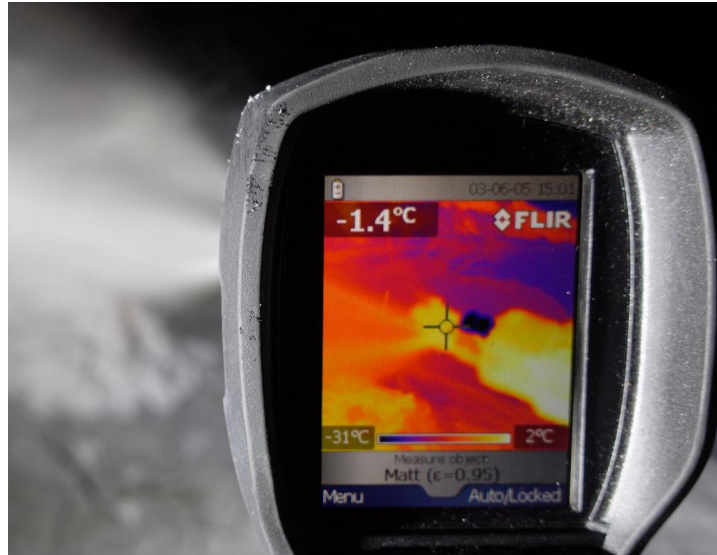


Figure 4.9: Temperature measured of the discharged water sheet in Arabygdi

### 4.1.6 Snow shape and density

The snow shape produced in Arabygdi was documented by the photographs shown in Figure 4.10 and Figure 4.11. In the photographs, it seems like ice droplets are stacked on each other.

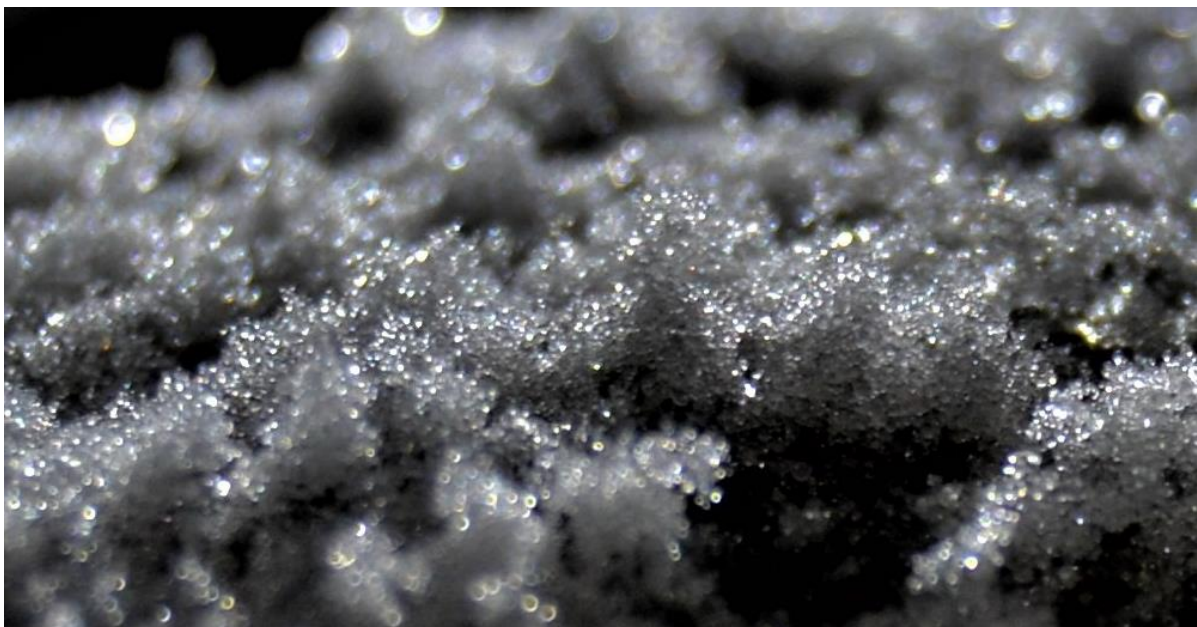


Figure 4.10: Rime shaped snow in Arabygdi



Figure 4.11: Rime shaped snow in Arabygdi

Within the time interval 01:30-03:00, approximately  $0.065 \text{ m}^3$  was produced with a density of  $489 \text{ kg/m}^3$ . The conical-shaped volume of snow collected in the middle of the tarpaulin and the density measurement are shown in Figure 4.12.

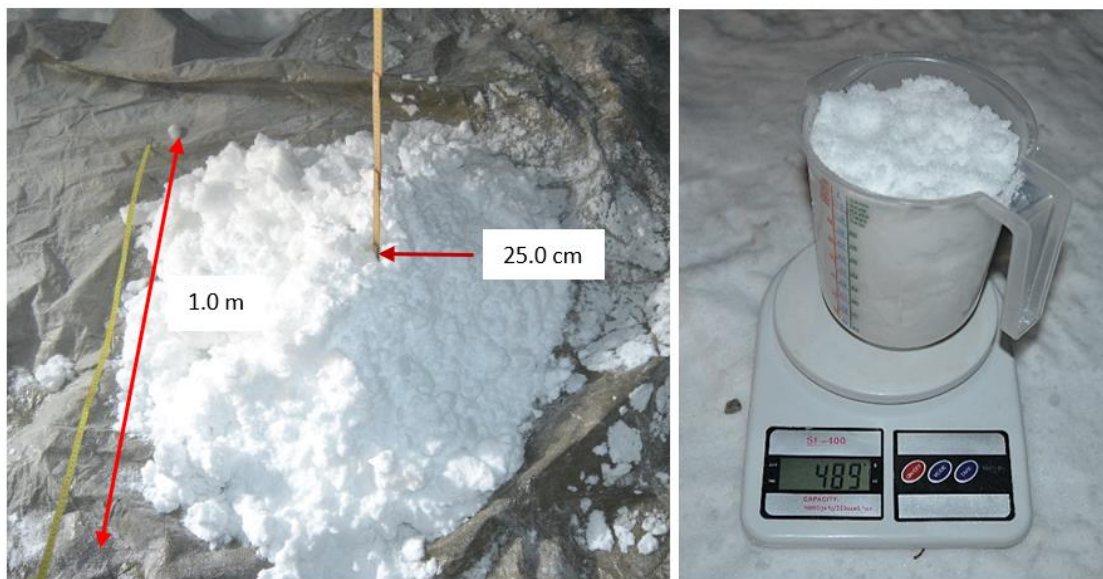


Figure 4.12: Volume and density of snow produced in Arabygdi

To summarize the effect of the nozzle system, it produced roughly  $0.065 \text{ m}^3$  of snow within 1.5 h with a density of  $490 \text{ kg/m}^3$ . This is a total of 32 kg of snow, which is produced by 90 kg of water supplied from the pump.

## 4.2 Modeling results

The purpose of the simulations was to verify if the model developed in Chapter 2.7 was representative of the actual spray and snow generation achieved by the Nedsnødd snow system. The Matlab code is available in Appendix D.

### 4.2.1 The motion of the droplets

The trajectory, flight time, and velocity profile obtained using the initial conditions were simulated for droplets with the diameter of 40, 50, 120, 170, and 360  $\mu\text{m}$ . The range of 40 – 170  $\mu\text{m}$  droplet sizes were defined based on the image processing performed in Arabygdi. The 360  $\mu\text{m}$  was used to investigate how larger droplets influenced heat and mass transfer.

In this study, the entrainment constant,  $C$ , was estimated based on velocity simulations of the 50  $\mu\text{m}$  droplets, which was further compared to the corresponding experimental median droplet velocity. The simulation result of the velocity and displacement obtained by changing the entrainment constant is presented in Figure 4.13. During the 50  $\mu\text{m}$  simulations, the entrainment constant was varied between 0.3 to 0.4, which is a commonly applied range for nozzles [34].

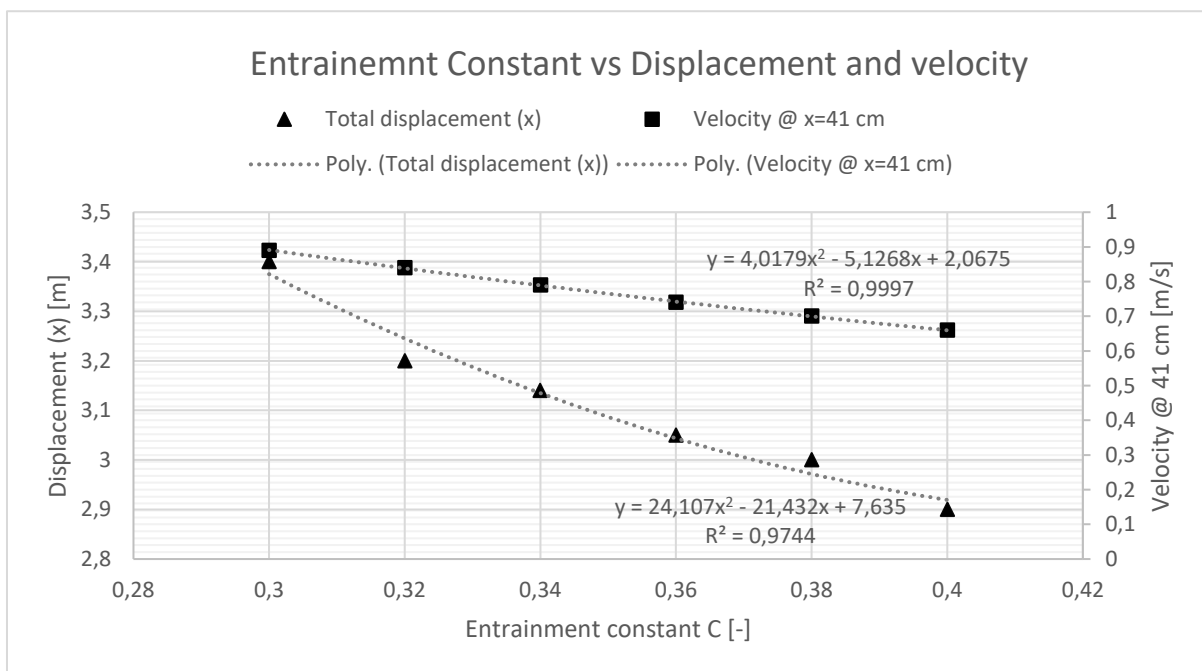


Figure 4.13: Result of displacement and velocity obtained by the 50  $\mu\text{m}$  droplets as a function of the entrainment constant

Figure 4.13 shows that the displacement and velocity of the 50  $\mu\text{m}$  droplets decrease by increasing the entrainment constant. The median experimental droplet velocity was obtained with an entrainment constant of 0.4. The value of 0.4 is therefore used in all the following simulations. The change in the maximum relative humidity in the mixed air by adjusting the entrainment constant is presented in Figure 4.13. As with the droplet velocity, the maximum relative humidity decreases with increasing entrainment constant.



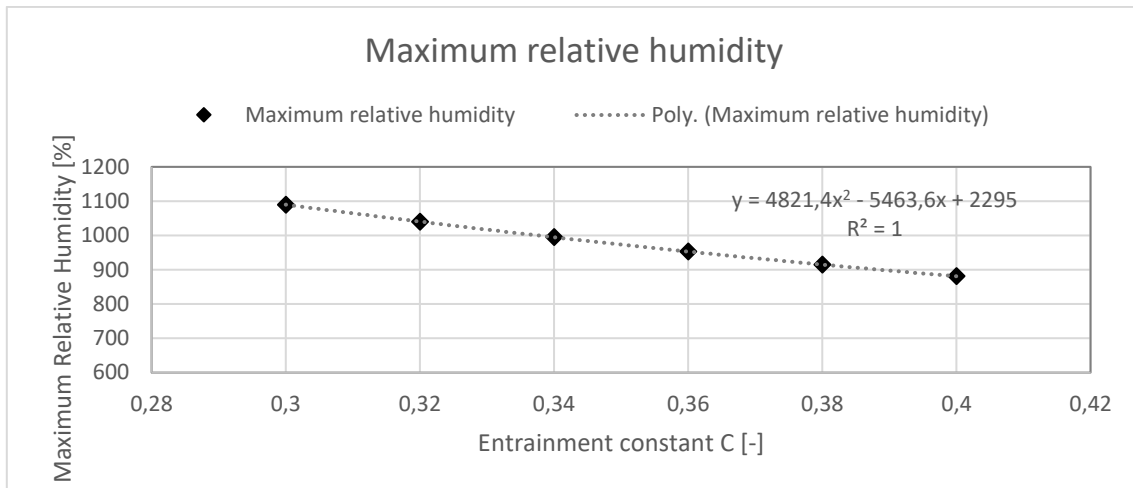


Figure 4.14: Result of maximum relative humidity obtained by the 50 µm droplets as a function of the entrainment constant

After defining the entrainment constant, the trajectory obtained by the 40, 50, 120, 170, and 360 µm droplets were modeled as shown in Figure 4.15.

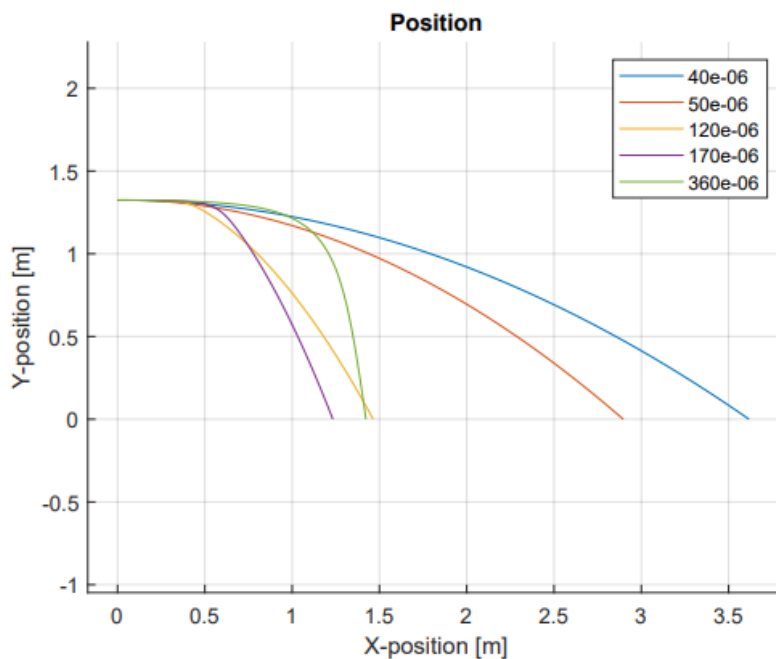


Figure 4.15: Position of the modeled droplets

The initial angle of the droplet trajectory was set to 0°. Also, the initial height of the droplets was defined as 1.324 m, which was the nozzle position measured during the experiment.

The droplet of 40 µm and 50 µm obtained the most significant displacement of 3.6 m and 2.9 m, respectively. The droplet of 360 µm landed at 1.4 m, the 170 µm droplet at 1.2 m and the 120 µm droplet at 1.5 m. The 360 µm droplet breaks the trend of obtaining higher displacement by decreasing droplet size.

## Results

Further, the flight time of each droplet was simulated, as shown in Figure 4.16. Here, the flight time obtained decreased by increasing the droplet size. The 360  $\mu\text{m}$  droplet reached the ground after 1.1 s while the 40  $\mu\text{m}$  droplet used 24 s.

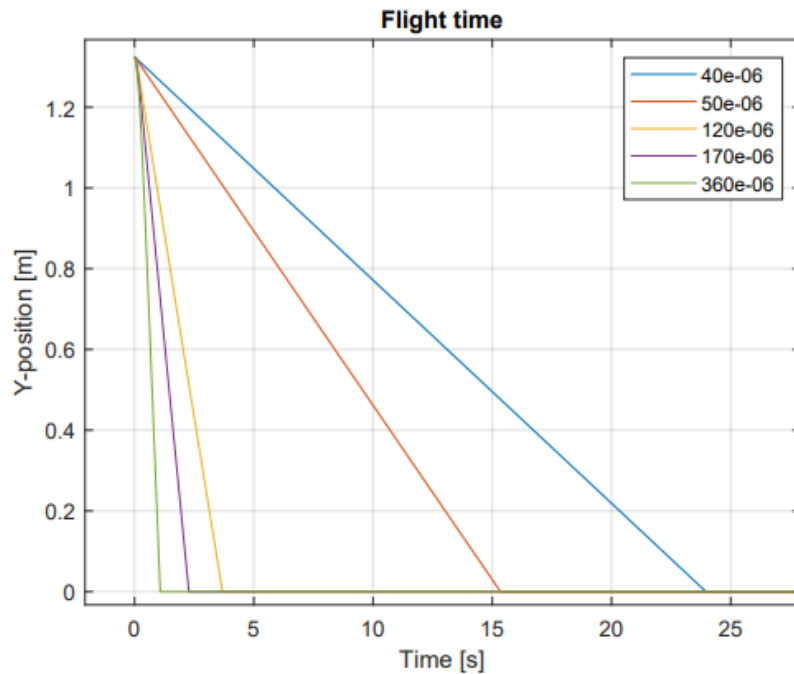


Figure 4.16: Flight time obtained by the modeled droplets

The velocity profile of each droplet was plotted as shown in Figure 4.17.

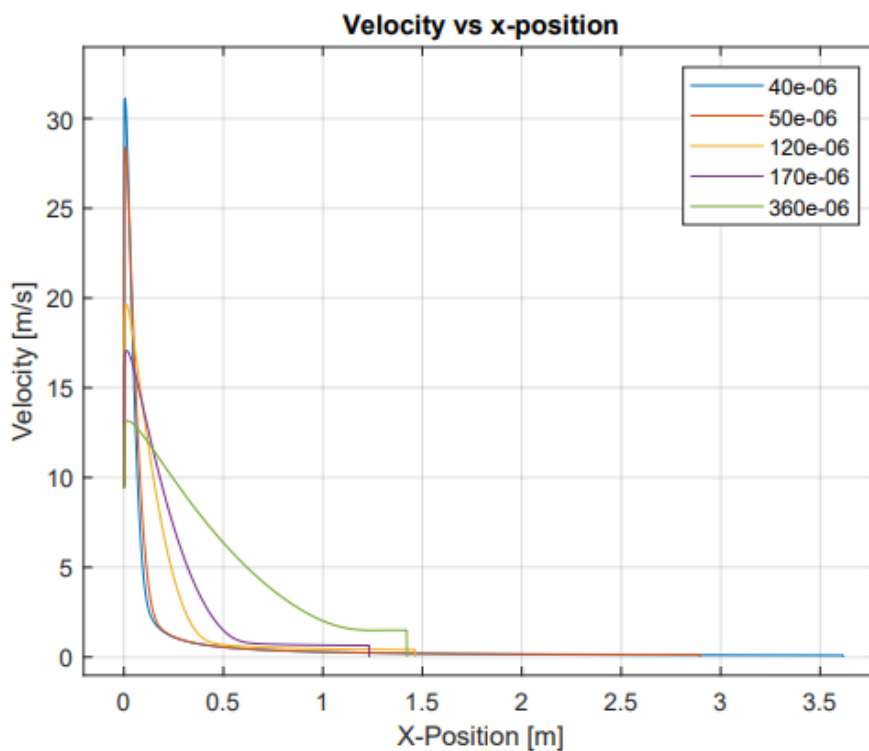


Figure 4.17: Velocity profile of the modeled droplets concerning the x-position of the droplets

## Results

In Figure 4.17, the velocity of the droplets starts at 9.43m/s and is further accelerated to a maximum velocity within 30-70 ms before it decreases down to the terminal velocity.

The flight time, displacement, maximum velocity, and terminal velocity are summarized in Table 4.3.

Table 4.3: Velocity and displacement measurements of the modeled droplets

Parameter					
Droplet diameter [ $\mu\text{m}$ ]	40	50	120	170	360
Flight time [s]	24	15	3.6	2.3	1.1
Travel length [m]	3.6	2.9	1.5	1.2	1.4
Max velocity [m/s]	31.1	28.4	19.6	17.0	13.1
Terminal velocity [m/s]	0.09	0.13	0.41	0.64	1.49

Table 4.3 shows that the maximum velocity and the flight time increase with decreasing droplet size. The terminal velocity increased by increasing droplet size. Further, the significant maximum velocity, flight time, and displacement obtained by the tiniest droplets were investigated by plotting the 40  $\mu\text{m}$  velocity profile against the mixed air velocity, as shown in Figure 4.18.

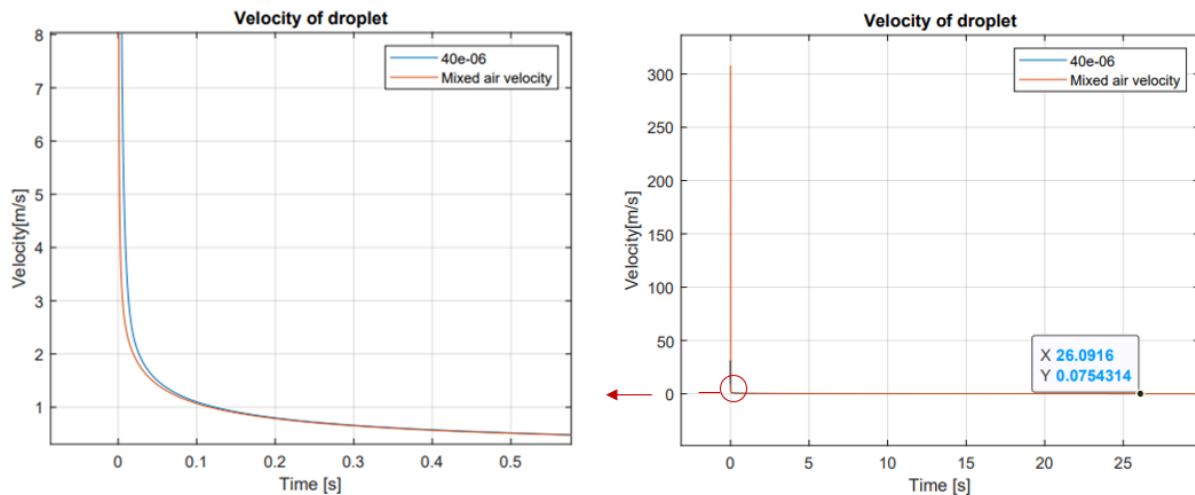


Figure 4.18: Velocity profile of mixed air and 40  $\mu\text{m}$  modeled droplets

Figure 4.18 shows that the velocity of the mixture starts at 307 m/s and decelerates down to a steady velocity of 0.07 m/s. The 40  $\mu\text{m}$  droplet starts at 9.43 m/s, accelerates up to 31 m/s before it deaccelerates down to the steady velocity of 0.07 m/s. It is also observed that the 40  $\mu\text{m}$  droplet follows the velocity profile of the mixed air.

The velocities obtained by the modeled droplets and the measured droplets from the image processing, 41 cm from the nozzle, are listed in Table 4.4. *I* represents image processing results, and *S* represents the modeling results. *D* is the droplet diameter and  $u_d$  is the droplet velocity. The median velocities were given for the image processing columns.

Table 4.4: Comparison of the velocity obtained by the modeled and measured droplets.

Parameter	I	S	I	S	I	S	I	S
$D$ [ $\mu\text{m}$ ]	37.2	40	50	50	124	120	174	170
$u_d$ [m/s]	0.9	0.67	0.66	0.66	0.5	0.95	2.1	2.84
Deviation of I to S	25 %		0 %		47 %		26 %	

### 4.2.2 Heat and mass transfer

The change in droplet temperature with time was simulated, as shown in Figure 4.19

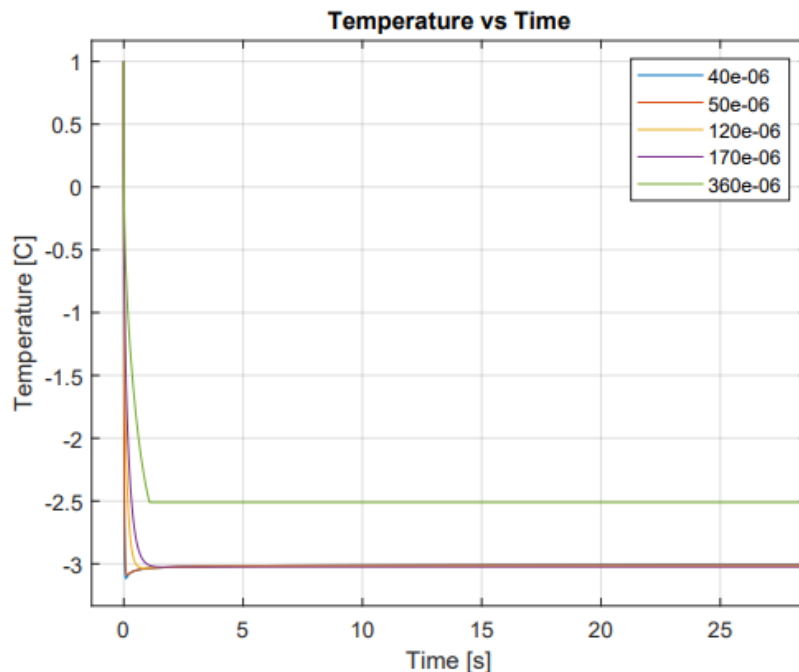


Figure 4.19: Temperature change of the modeled droplets as a function of time

In Figure 4.19, the initial temperature of the droplets is 1 °C. The droplets are cooled down to 0 °C within microseconds before the temperature is further decreased. Figure 4.20 shows how the temperature of the droplets converges to its final temperature.

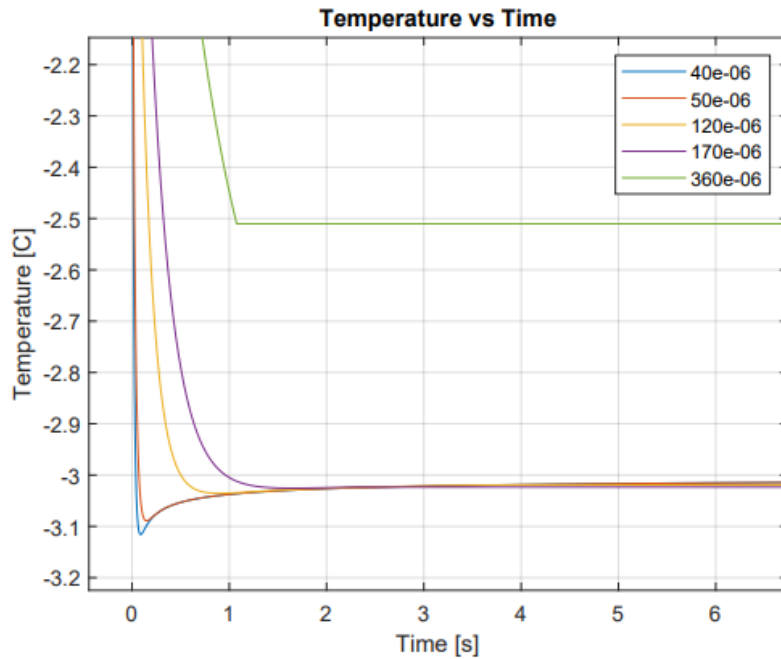


Figure 4.20: Zoomed-in plot of Figure 4.19

Figure 4.20 shows that the 360  $\mu\text{m}$  droplet does not reach the same final temperature as the other droplets. All droplets, except the 360  $\mu\text{m}$  droplet, were cooled down to a temperature just below the ambient temperature of  $-3^\circ\text{C}$  before hitting the ground. The droplet temperature as a function of travel length is illustrated in Figure 4.21.

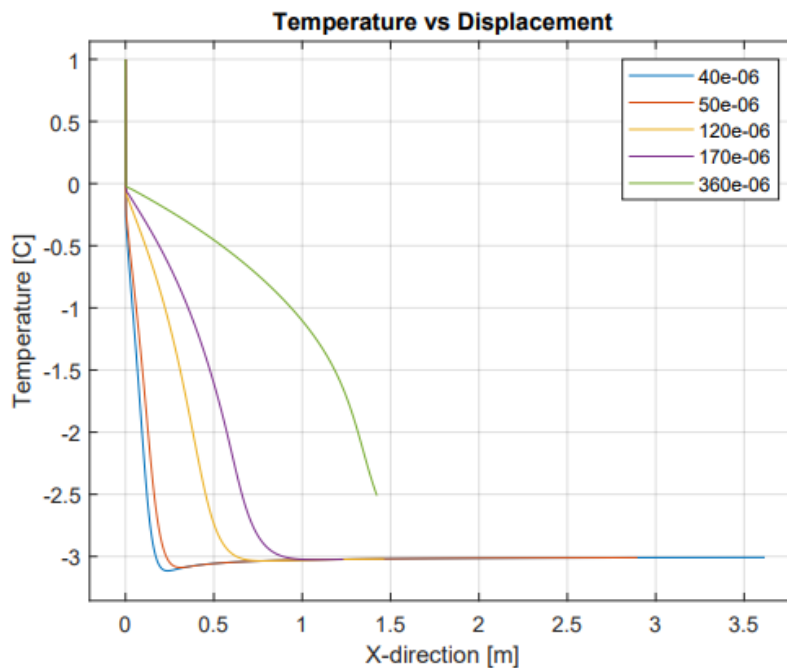


Figure 4.21: Temperature change concerning the motion of modeled droplets in the x-direction

Figure 4.21 shows that the temperature decrease as the droplets move away from the origin. The measured values from the temperature simulations are listed in Table 4.5.

Table 4.5: Temperature correlated measurements of the modeled droplets

Parameter					
Droplet diameter [ $\mu\text{m}$ ]	40	50	120	170	360
Flight time [s]	24	15	3.6	2.3	1.1
Cooling time ( $0^\circ\text{C}$ ) [ $\mu\text{s}$ ]	28	33	83	90	146
Temperature at $x = 10 \text{ mm}$ [ $^\circ\text{C}$ ]	-0.1	-0.07	0.02	0.03	0.1
Lowest obtained T [ $^\circ\text{C}$ ]	-3.1	-3.08	-3.03	-3.02	-2.5

Table 4.5 indicates that all of the simulated droplets are cooled down to  $0^\circ\text{C}$  within a maximum of  $146 \mu\text{s}$ . The lowest temperature obtained is achieved by the smallest droplet and is increasing with increasing diameter. In addition, the diameter reduction due to evaporation was simulated and listed in Table 4.6. The droplets were reduced by 0.05-0.06 % during the flight time.

Table 4.6 Droplet size-reduction of the modeled droplets

Droplet size-reduction					
Initial D [ $\mu\text{m}$ ]	40	50	120	170	360
Final D $\mu\text{m}$	39.98	49.97	119.93	169.90	359.78
Reduction %	0.05	0.06	0.58	0.058	0.06

Further, the relative humidity change in the mixed air due to evaporation was simulated for the 40 ad 360  $\mu\text{m}$  droplets, as shown in Figure 4.22.

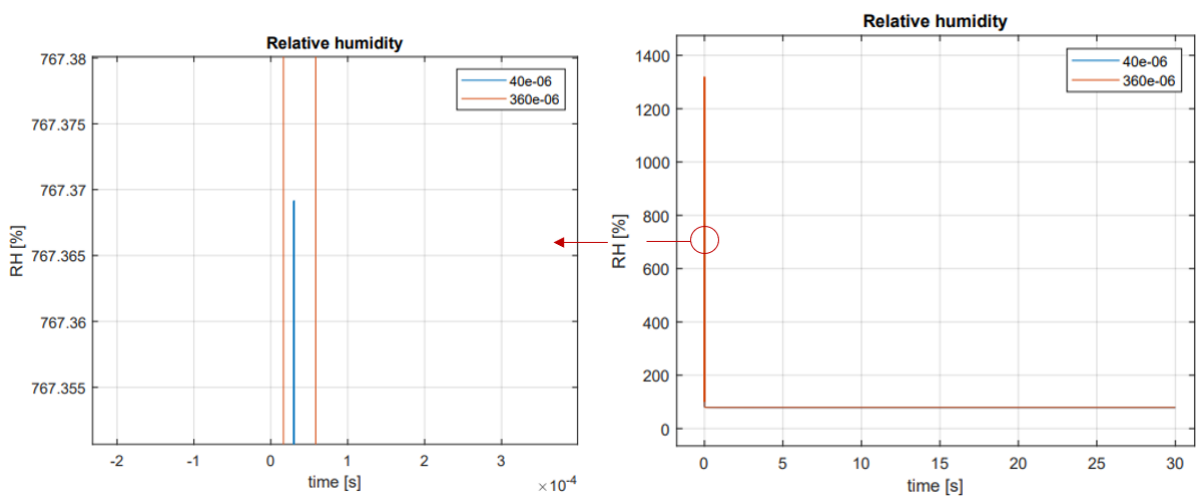


Figure 4.22: Relative humidity of mixed air with 40 and 360  $\mu\text{m}$  droplets

## Results

The relative humidity of the mixture with 40 and 360  $\mu\text{m}$  droplets, increases from 99 % to 767 and 1317 %, respectively, within 30  $\mu\text{s}$ , before it converges down to a steady value of 78.7 %.

Further, the 40 and 360  $\mu\text{m}$  droplets were simulated with the ambient temperature and relative humidity measured during the experiments in Porsgrunn and Arabygdi. The same pressure parameters were applied for both of the simulations. Table 4.7 contains the initial condition used and the results obtained.

Table 4.7: Measured parameters of the 40 and 360 droplets exposed to the different weather conditions in Porsgrunn and Arabygdi

Parameter	Porsgrunn		Arabygdi	
$RH_0$	96 %		79 %	
$T_\infty$	-2.6 °C		- 3 °C	
Droplet size [ $\mu\text{m}$ ]	40	360	40	360
$RH_{mix,max}$ [%]	782	1317	767	1319
Flight time [s]	23	1.1	23	1.1
Cooling time (0°C) [ $\mu\text{s}$ ]	30	200	28	146
Droplet reduction [%]	0.04	0.06	0.04	0.06
The lowest temperature obtained [°C]	-2.7	- 2.2	-3.1	-2.5

Table 4.7 shows that the maximum obtained relative humidity was similar for the 360  $\mu\text{m}$  droplets in both simulations. In contrast, the relative humidity value was higher for the 40  $\mu\text{m}$  droplets in Porsgrunn. The droplet diameter reduction of the 40 and 360  $\mu\text{m}$  droplet was equal in both simulations. In addition, the 40  $\mu\text{m}$  droplets obtained a temperature lower than the ambient temperature in each simulation. On the other hand, the 360  $\mu\text{m}$  droplets did not reach the ambient temperature in either case.

## 5 Discussion

### 5.1 Findings from the literature study:

This paper aimed to perform a literature study on artificial snow production and perform an experimental study on snow generation with the snow system developed by Nedsnødd. There was, however, little literature on this specific topic. The theory was therefore mainly written based on natural snow formation, starting by investigating the water cycle process. Cloud types and precipitation particles were categorized, which are the sources of natural snow formation. Tiny water droplets in the cloud can reach a temperature as cold as  $-40\text{ }^{\circ}\text{C}$  without freezing, which is a supercooled state. The snow formation processes were presented, where tiny droplets in the cloud have been observed to reach a supercooled state at a temperature as cold as  $-40\text{ }^{\circ}\text{C}$  without freezing. The supercooled droplets that fall from the cloud may freeze and grow a snowflake as they interfere with other frozen droplets or natural nuclei, which activate the freezing process. The other way of growing a snowflake is with the help of sublimation. In this process, the sublimated molecules attach to the nuclei and each other, and grows the snowflake. Comparing the natural snow formation process with the artificial process, the most obvious difference is the time available to form a snowflake. For natural snow, the residence time in the air can be as long as 20 minutes, while artificial snow must be produced in seconds.

Artificial snow production is divided into temperature-dependent and temperature-independent technologies. This thesis focuses on snow guns and lances, which are examples of temperature-dependent technologies. The temperature-dependent part implies that snow production relies on the ambient conditions to produce snow and work on the same principles. Water is discharged to the ambient air through nozzles and then further atomized and accelerated by compressed air or a fan. The droplet cools down during the trajectory towards the ground and may freeze depending on if they interfere with either natural or synthetic nucleus or other frozen droplets. Some of the machines are delivered with so-called nucleators, which discharge such nuclei powder. The Nedsnødd artificial snow system used in this thesis was described. The unique part of this system was the novel-twin-fluid annular sheet nozzle. Here, water is discharged through an annular sheet and further atomized by the interference with high-velocity air from the nozzle center. The nozzle is designed with a cone, increasing the interference of the water and airflow, which further increases the atomization.

Two studies performed on the artificial snow production topic were presented, however, these studies did not focus on the snow production process itself. The first study performed in the Austrian Alps produced a mean density snow of  $400\text{ kg/m}^3$  where the droplets had  $0.2\text{-}0.4\text{ mm}$  diameter and a flight time of  $10\text{-}15\text{ s}$ . The second study was performed at the Granåsen ski resort in Trondheim. A mean density of  $811\text{-}936\text{ kg/m}^3$  was produced with a water pressure of  $30\text{ bar}$  gauges supplied to  $328$  nozzles. The water temperatures used for both studies were below  $2\text{ }^{\circ}\text{C}$ . The usage of nucleators, the ambient temperature, and pressure were not defined in either case. Further, the snow quality was determined based on a third study performed in Slovakia. From a density classification developed here, the target density of this thesis was defined as  $500\text{ kg/m}^3$ .



During this thesis, three experiments were performed to verify if the thesis's theory, model, and assumptions were acceptable. The experiments were performed in Porsgrunn, Arabygdi, and Kviteseid. The only experiment yielding snow was the Arabygdi experiment performed the evening of the 18<sup>th</sup> throughout the early morning of 19<sup>th</sup> of March 2021. 0.065 m<sup>3</sup> snow with a density of 490 kg/m<sup>3</sup> was produced in 1.5 hours.

## 5.2 Droplet size, distribution, and velocity.

A video recording created using a high-speed camera during the experiment in Arabygdi was imported into a premade image processing code. The camera was positioned 41 cm away from the nozzle tip. 77 droplets were analyzed and converted to both an experimental and a Weibull distribution plot. Both plots were merged into a comparison chart, indicating that the Weibull and experimental distributions have similar trends. The distribution values were, however, not consistent. This may be due to the inherent uncertainty and limitations of the setup and the small population of droplets analyzed.

Further, the experimental droplet size and velocity measured were plotted and compared to the simulated results. A significant variation in the droplet velocity for similar droplet sizes was observed. The variation of velocity of the same droplet size may indicate that the droplets were exposed to different flow conditions. Some recirculation was observed among the video images used in the image processing, which supports this claim. From the plot of average velocities in Figure 4.7, the trendline indicates increasing droplet velocity with increasing droplet diameter. This is consistent with the model, which shows the same trend in Figure 4.17 after traveling 41 cm in the x-direction. This is probably due to the fact that the drag, according to Equation 2.23, is inversely proportional to the droplet diameter. This also explains why the highest velocity is achieved by the smallest droplet of 40  $\mu\text{m}$  in the same figure.

The entrainment constant was estimated to be 0.4 based on the experimental median velocity of the 50  $\mu\text{m}$  droplets after 41 cm of travel in the x-direction. The median velocity was used instead of the mean velocity to avoid a skewed representation of the typical value. The simulations show that the maximum obtained relative humidity of the mixed air, velocity, and the droplets' travel length increased by decreasing the entrainment constant. These observations may be explained by the increased rate of entrainment with increasing entrainment constant. The maximum relative humidity decreases as the air entrained dilutes the air from the nozzle with low water content. For the velocity and travel length, the momentum balance can explain the observed results. A reduced entrainment rate means that more momentum can be transferred from the nozzle air to the droplets, hence a higher velocity and longer travel length.

After defining an entrainment constant of 0.4, droplets of 40, 50, 120, and 170  $\mu\text{m}$  in diameter were simulated to reflect the droplets observed in the experimental study. In addition, a 360  $\mu\text{m}$  diameter droplet was simulated to investigate how larger droplets compared to smaller ones. The droplet trajectory, flight time, and velocity were then simulated for the droplets. From the trajectory and flight time simulations in Figure 4.15 and Figure 4.16, it can be observed that both the travel length and flight time, excluding the largest droplet for travel length, in general increase with decreasing droplet diameter. However, for the travel length,

there seems to be a point where a larger diameter actually is beneficial. The 360  $\mu\text{m}$  droplet moved 1.4 m in 1.1 s, which is 20 cm farther than the 170  $\mu\text{m}$  droplet. The small droplets traveling so far in the model are mainly due to the mixed air velocity, which never reaches zero. From Figure 4.18, it can be observed that the 40  $\mu\text{m}$  approaches the mixed air velocity and gets carried forward by the drag. However, if the mixed air velocity for instance is assumed to be zero after 1 m, the small droplets almost stop at the spot and drop directly to the ground (see Appendix H). The travel length observed in the model will in this case be increasing with increasing droplet diameter. However, the flight times of the droplets are only slightly affected by this manipulation and still be very similar to the values given in Table 4.3. The travel lengths simulated seem plausible when compared to the spray dimensions in Figure 4.2. Small droplets (fog) or snow particles could also be observed as far as 80 cm away from the nozzle, indicating that the small droplets traveled farther than the big droplets. The flight time of droplets in the real spray was not measured and therefore hard to compare to the simulated results.

The velocity simulation of the droplets in Figure 4.17, shows that the smallest droplet obtains both the maximum velocity and the minimum velocity. This is as mentioned earlier, a result of the inverse proportional relationship between the drag and the droplet diameter. In Figure 4.18, which compares the mixed air velocity with the 40  $\mu\text{m}$  droplet velocity, the mixed air starts at 307 m/s, representing the airflow from the nozzle's throat by assuming the Mach number to be equal to 1. Thus, the mixed air velocity is initially equal to the speed of sound. As the airflow is discharged from the nozzle, it interferes with the water sheet and the surrounding air, creating a mixture. Momentum is thus transferred from the high-velocity airflow to the entrained air and the water droplets, causing the mixed air velocity to approach zero rapidly. When the mixed air in turn has a lower velocity than the droplets, there will be momentum transfer from the droplets to the air, which decelerates the droplets. The terminal velocity achieved by the droplets represented in Table 4.3, represents the velocity where the drag and buoyancy forces are equal to the gravity force. The acceleration is thereby zero.

The entrainment constant was estimated to be 0.4 based on the 50  $\mu\text{m}$  median velocity, and in Table 4.4, the velocities, after 41 cm of travel in the x-direction, obtained by a few simulated and experimental droplet sizes are listed.

The discrepancies between the two velocities are relatively large and may indicate the inherent uncertainty of the setup, the complexity of the spray, and the small droplet population investigated. Another possibility is that the entrainment model is inaccurate.

### 5.3 Heat and mass transfer

Whether or not the droplets would be cooled down to 0 °C before they reached the ground was of interest as it indicates the possibility of snow formation. The airflow temperature inside the nozzle's throat was calculated to be -37.19 °C, assuming an ideal isentropic process and a stagnation temperature from the compressor to 10°C. A thermographic photo taken in Arabygdi shows that the material at the nozzle tip is - 37.5°C, which may indicate that the assumptions were reasonable.

As the water was considered incompressible, which makes the density constant, the temperature through the nozzle was assumed to be isothermal at 1 °C.

A thermographic photograph of the discharged water sheet, 1 cm out from the nozzle exit plane in Arabygdi, indicated that the water had been reduced to roughly - 1.4 °C. The temperature simulation of the droplets showed that the droplets had reached  $0 \pm 0.1$  °C at this point of the nozzle, see Table 4.5 for more information. As the thermographic camera used has an accuracy of  $\pm 2^\circ$ , the result seems reasonable. Also, the temperature simulation showed that all droplets reached 0 °C within 150  $\mu$ s and could freeze before they reached the ground. All droplets except the largest one, reached a temperature lower than the defined ambient temperature as can be seen in Figure 4.19 and Figure 4.20. This may be explained by the temperature of the air mixture which will be lower than the ambient temperature (see Appendix H) as it is a mixture of the cold nozzle air and the entrained ambient air. The 360  $\mu$ m droplet did however not reach the ambient temperature, which probably have to do with the low travel time combined with the inverse proportional relationship between the convective heat transfer coefficient and the droplet diameter (see Appendix C).

The change of the relative humidity of the mixed air with a spray containing 40 and 360  $\mu$ m droplets were also simulated and presented in Figure 4.22. As the airflow discharged from the nozzle was assumed to be saturated, the relative humidity starts at approximately 100 %. The air flow is then mixed with evaporating water and entrained air and the relative humidity increases rapidly to 797 and 1319 %, respectively. The high values of relative humidity might seem unreasonably high, but as condensation is not taken into account in the model, the high relative humidity should rather be interpreted as an indication of fog formation. After the water stops evaporating at 0 °C (defined by the model), the relative moisture rapidly approaches the ambient relative humidity as the entrained air fraction increases. Figure 4.2 and 4.3 may support the high relative humidity simulated as the sprays look foggy.

The evaporation of water from the water droplets results in a reduction in the droplet diameter as the droplet travels through the air. The reductions of the different droplet diameters are listed in Table 4.6. All of the droplet sizes experience the same reduction in size, approximately 0.05-0.06 %. This is consistent with the higher relative moisture content simulated for the 360  $\mu$ m compared to the 40  $\mu$ m, as a reduction of 0.06 % in the droplet diameter represents a larger volume of water for a larger droplet.

The simulations indicate that both the Porsgrunn and Arabygdi experiments had the possibility to produce snow, implying that there may have been other factors that influenced the results. The experiment in Porsgrunn was not performed within a continuous cold period like the experiment performed in Arabygdi. Thus, the ground in Porsgrunn was probably not frozen and may have heated up the falling droplets. In addition, the water used in the experiment in Porsgrunn was supplied by filtered tap water, compared to the water supply used in Arabygdi, which were carried out from the lake. A possible explanation is that the lake contained natural nucleators, which activated the snow formation in Arabygdi. By comparing the photos taken of the sprays obtained in both Porsgrunn and Arabygdi, it seems like the first only contain droplets and fog. The picture of the spray in Arabygdi indicates both fog and a tendency of precipitations.

Further, the snow shape obtained in Arabygdi was photographed. From the picture, frozen droplets are stacked on each other and maybe characterized as rime formation. The characterization seems reasonable as the droplets do not have a growth time of several

## Discussion

minutes. In comparison, dendritic-shaped snowflakes may use 20 minutes from the cloud where it is discharged, down to earth, exposing them to different weather conditions. However, the rime formation confirms that the assumption regarding the continuous spherical shape throughout the trajectory while developing the droplet model seems reasonable.

The Nedsnødd system produced 32 kg of  $490 \text{ kg/m}^3$  within 1.5 h., which satisfied the goal density requirement of less than  $500 \text{ kg/m}^3$ . This snow was produced at low pressures compared to conventional equipment, which possibly can reduce the energy consumption and thus the cost.

## 6 Further work

The number of experiments should be performed numerous times with different relative humidities and ambient temperatures to validate the theoretical model. December to March may be an excellent period to perform tests in marginal conditions as the air is relatively dry. A test matrix that is available in Appendix G may be used for the experiments.

The weather forecast shall be checked before each experiment. Here, the ambient temperature, relative humidity, and wind velocity are essential parameters. Also, if the experiment is carried outside the civilization, the water supply shall be considered for the planning. If more electrical devices than the existing experimental rig, a computer, the high-velocity camera, and the flash are to be used, the electricity available shall be evaluated.

A weather station should be implemented to precisely monitor the weather conditions at the experimental position. A water resistance thermometer should also be placed in the buffer water tank or the water source to measure the temperature of the influent water flow. Suppose natural water from a lake is used. In that case, a filter between the buffer tank and the pump should be implemented, preventing large particles from accumulating inside the nozzle. On the other hand, the filter shall not remove the natural nucleus.

One possibility of running several experiments and manipulating the ambient conditions is performing the experiments in indoor ski facilities.

A water analysis of the water source should be performed to determine the nucleus content. If this is performed for each experiment on different locations with similar ambient temperature and relative humidity and pressures, the influence of the nucleus may be verified.

If the experiments have to be performed outside, a tent should protect electrical devices from the spray.

A thermographic shot shall be taken of the experimental setup as a whole to obtain an indication of the temperature gradients around the rig. Also, the produced snow shall be photographed with a specific time interval to determine the temperature change. A microscope should be used to analyze the size and shape of the product snow.

During each experiment, both the water airflow pressure shall be manipulated to check how the trajectory, width of spray, atomization, and droplet velocity correspond.

Video recordings at specific points along the total spray should be performed for each pressure adjustment to obtain a representative correlation between the droplet trajectory and velocity. The different video recordings can also verify whether the droplets accumulate in the air or on the ground.

When it comes to the modeling part, the growing of crystals with the help of sublimation can be included. The freezing process of the droplets should be implemented into the theoretical model to verify whether the droplets freeze before they reach the ground. In addition, by including the temperature gradient and moving boundaries, the freezing period should be more accurate. The heat transferred from the droplets to the mixed air also be included.

Further, the entrainment constant for the Nedsnødd nozzle should be investigated to obtain the correct droplet trajectory in the model. Condensation of the mixed air can be investigated to achieve a more accurate change in relative humidity.

## 7 Conclusion

This work aimed to perform both literature and experimental study of artificial snow production in marginal geographic conditions. A snow-producing rig designed by a Norwegian developer, Nedsnødd, was used during the experimental study. The innovative part of the rig was the assembled novel twin-fluid annular sheet nozzle, where a thin sheet of water was atomized into droplets by high-velocity air.

As the literature on artificial snow production was limited, the water cycle and natural snow formation were studied to understand artificial snow production. A theoretical model was developed to analyze the trajectory and heat and mass balance of a single droplet discharged from the nozzle. The snow density goal for this thesis was defined to  $500 \text{ kg/m}^3$  based on a snow quality study performed in Slovakia. Three experiments were performed during the project. A high-speed camera was used to record the droplet size and velocity in the spray. The experimental measurements were further used to improve the droplet model.

Only one of the experiments performed in Arabygdi yielded snow with a density of  $490 \text{ kg/m}^3$ , which satisfied the snow density goal of  $500 \text{ kg/m}^3$ . During a time interval of 1.5 h, 32 kg of acceptable snow was produced at low water and air pressures compared to conventional technology. These relatively low water and air pressures may in turn reduce the energy consumption of the snow production and ultimately the cost of the snow.

Due to the short winter season in Porsgrunn during this project, only a few experiments were performed, making this thesis more of a basis for future planned experiments.

## 8 References

- [1] M. Bellis. “Who Invented the Snowmaking Machine?” ThoughtCo. [The History of the Snowmaking Machine \(thoughtco.com\)](https://www.thoughtco.com/history-of-the-snowmaking-machine-1379211/) (accessed Apr. 14, 2021).
- [2] Y. A. Cengel, M. A. Boles and M. Kanoglu, “Properties of pure substances,” in *Thermodynamics an Engineering Approach*, 8<sup>th</sup> ed. New York: McGraw-Hill Education, 2015, pp. 111-161.
- [3] J. Xu, Q. Wei, S. Peng and Y. Yu, “Error of Saturation Vapor Pressure Calculated by Different Formulas and Its Effect on Calculation of Reference Evapotranspiration in High Latitude Cold Region,” *2012 International Conference on Modern Hydraulic Engineering*, vol. 28, Elsevier Ltd, unknown, pp.43-48, 2012. [Online]. Available: doi: [Error of Saturation Vapor Pressure Calculated by Different Formulas and Its Effect on Calculation of Reference Evapotranspiration in High Latitude Cold Region \(sciencedirectassets.com\)](https://doi.org/10.1016/j.icmh.2012.09.001)
- [4] “Water cycle.” [water cycle | Definition, Steps, Diagram, & Facts | Britannica](https://www.britannica.com/science/water-cycle) (accessed Jan. 24, 2021).
- [5] Y. A. Cengel, M. A. Boles and M. Kanoglu, “Gas-vapor mixtures,” in *Thermodynamics an Engineering Approach*, 8<sup>th</sup> ed. New York: McGraw-Hill Education, 2015, pp. 687-758.
- [6] J. Żulawińska. “Wet Bulb Calculator.” [Wet Bulb Calculator \(omnicalculator.com\)](https://www.omnicalculator.com/physics/wet-bulb) (accesses Jan. 20, 2021).
- [7] “Snowmaking Weather Tools.” [SNOWatHOME » Snowmaking Weather Tools - learn when you can make snow at home](https://www.snowat-home.com/snowmaking-weather-tools) (accessed Jan. 8, 2021).
- [8] F. P. Incropera, D. P. Dewitt, T.L. Bergman and A. S. Lavine, “Diffusion Mass Transfer,” in *Incroperas's principles of heat and mass transfer*, 1<sup>st</sup> ed. New York: John Wiley & Sons Inc, 2017, pp. 863-910.
- [9] F. P. Incropera, D. P. Dewitt, T.L. Bergman and A. S. Lavine, “Appendix A,” in *Incroperas's principles of heat and mass transfer*, 1<sup>st</sup> ed. New York: John Wiley & Sons Inc, 2017, pp. 911-942.
- [10] P. K. Wang, “Observation of clouds,” in *Physics and Dynamics of Clouds and Precipitation*, 1<sup>st</sup> ed. New York: Cambridge University Press, 2013, pp. 1-26. [Online]. Available: [ProQuest Ebook Central - Detail page \(usn.no\)](https://www.proquest.com/physics/observation-of-clouds/docview/238444444)
- [11] P. K. Wang, “The shape and size of cloud and precipitation particles,” in *Physics and Dynamics of Clouds and Precipitation*, 1<sup>st</sup> ed. New York: Cambridge University Press, 2013, pp. 27-67. [Online]. Available: [ProQuest Ebook Central - Detail page \(usn.no\)](https://www.proquest.com/physics/the-shape-and-size-of-cloud-and-precipitation-particles/docview/238444444)
- [12] K. G. Libbrecht, “The physics of snow crystals,” *Reports on Progress in Physics*, Pasadena, USA, vol. 68, nr.4, pp. 855-895 2005. [Online], Available: [The physics of snow crystals - IOPscience](https://iopscience.iop.org/article/0034-0022/68/4/R01)

## References

- [13] P. K. Wang, "Collision, coalescence, breakup, and melting," in *Physics and Dynamics of Clouds and Precipitation*, 1<sup>st</sup> ed. New York: Cambridge University Press, 2013, pp. 252-287. [Online]. Available: [ProQuest Ebook Central - Detail page \(usn.no\)](#)
- [14] P. Singh and V. Singh, *Snow and Glacier Hydrology*, 1<sup>st</sup> ed. Dordrecht: Kulwer Academic Publishers, 2001 [Online]. Available: [Snow and Glacier Hydrology - P. Singh - Google Bøker](#)
- [15] C. Fierz et al., "The International Classification for Seasonal Snow on the ground," IHP-VII Technical Documents in Hydrology N°83, IACS Contribution N°1, pp.1-90, 2009. [Online]. Available: [The International classification for seasonal snow on the ground; Technical documents in hydrology; Vol.:83; 2009 - 186462eng.pdf \(unesco.org\)](#)
- [16] O. E. Hansen Berg, "Optimal produksjon av snø fra flere produksjonsenheter i samme område," Master thesis, Department of Engineering cybernetics, Norwegian University of Science and Technology, Trondheim, 2017. [Optimal produksjon av snø fra flere produksjonsenheter i samme område \(ntnu.no\)](#)
- [17] Stian Trædal, "Temperature independent snow production," SINTEF, unknown, Norway, 2017:00874, Dec.19, 2017. [Online]. Available: [Termperature-indepdent-snow-production.pdf \(xn--snkompetanse-wjb.no\)](#)
- [18] "TT10: Tower Power." [TT10 snow gun from TechnoAlpin - a new level!](#) (accessed Apr. 21, 2021).
- [19] "TL lance series: New dimension for snowmaking." [TL series of TechnoAlpin snowmaking lances](#) (accessed Apr. 21, 2021).
- [20] "Happysnow hjemmesnøkanon." [Happysnow hjemmesnøkanon - Happysnow](#) (accessed Apr. 07, 2021).
- [21] M. Mikloš, J. Skvarenina, M. Jančo, and J. Skvareninova, "Density of Seasonal Snow in the Mountainous Environment of Five Slovak Ski Centers," *Water*, vol.12, no.12, p 3563, 2020. [Online]. Available: [Water | Free Full-Text | Density of Seasonal Snow in the Mountainous Environment of Five Slovak Ski Centers \(mdpi.com\)](#)
- [22] M. Olefs, A. Fischer and J.Lang, "Boundary Conditions for Artificial Snow Production in the Austrian Alps," *Journal of applied meteorology and climatology*, vol.49, no. 6, pp. 1096-1113, 2010. [Online]. Available: [Boundary Conditions for Artificial Snow Production in the Austrian Alps \(usn.no\)](#)
- [23] Y. A. Cengel, M. A. Boles and M. Kanoglu, "Compressible flow," in *Thermodynamics an Engineering Approach*, 8<sup>th</sup> ed. New York: McGraw-Hill Education, 2015, pp. 839-896.
- [24] J. M. Smith, H. C. Van Ness, M. M. Abbott and M.T. Swihart, "The Second Law of Thermodynamics," in *Introduction to Chemical Engineering Thermodynamics*, 8<sup>th</sup> ed. Boston: McGraw-Hill Education, 2018, pp. 173-210.
- [25] Y. A. Cengel, M. A. Boles and M. Kanoglu, "Property Tables and charts," in *Thermodynamics an Engineering Approach*, 8<sup>th</sup> ed. New York: McGraw-Hill Education, 2015, s 897-946.



## References

- [26] Y. A. Cengel, M. A. Boles and M. Kanoglu, "Mass and energy Analysis of control volumes," in *Thermodynamics an Engineering Approach*, 8<sup>th</sup> ed. New York: McGraw-Hill Education, 2015, pp. 213-274.
- [27] K. Rottmann, *Matematische Formelsammlung*, 5th ed. Unknown: Spektrum forlag, 1995.
- [28] J I. McCool. "Properties of the Weibull Distribution," in *Using the Weibull Distribution Reliability, Modeling, and Interference*, 1 ed. Hoboken, New Jersey: John Wiley & Sons, Inc 2012, pp.73-79. [Online] Available: [ProQuest Ebook Central - Reader \(usn.no\)](#)
- [29] A. H. Lefebvre and V. G. McDonell, *Atomization and Sprays*, 2<sup>nd</sup> ed. Boca Raton: Taylor & Francis Group, LLC, 2017
- [30] J. Lundberg, "Image-based sizing techniques for fire water droplets," Doctoral thesis, Department of Process-, Energy and Environmental Technology, Telemark University College, Porsgrunn, 2015.
- [31] H. D. Young and R. A. Freedman, "Applying Newton's Laws," in *Sears and Zemansky's University Physics with Modern Physics Technology Update Hugh D. Young Roger A. Freedman Thirteenth Edition*, 13<sup>th</sup> ed. Harlow: Pearson, 2014, pp. 151-196.
- [32] A.R. Dehghani-Sani, Y.S. Muzychka, G.F. Naterer, "Droplet trajectory and thermal analysis of impinging saline spray flow on marine platforms in cold seas and ocean regions," *Ocean Engineering*, vol. 148, pp. 538-547, Jan. 2018. [Online]. Available: [Droplet trajectory and thermal analysis of impinging saline spray flow on marine platforms in cold seas and ocean regions - ScienceDirect](#)
- [33] S. S. Karunaratna and L. Tokheim, "Comparison of the Influence of Drag Models in CFD Simulation of Particle Mixing and Segregation in a Rotating Cylinder," presented at Proceedings of the 58<sup>th</sup> SIMS September 25 th-27<sup>th</sup>, Reykjavik, Iceland, 2017.
- [34] A. Kabanshi and M. Sanberg, "Entrainment and its implications on microclimate ventilation systems: Scaling the velocity and temperature field of a round free jet," *International Journal of Indoor Environment and Health*, vol. 29, nr. 2, pp. 331-346, 2018. [Online]. Available: doi: 10.1111/ina.12524.
- [35] H. D. Young and R. A. Freedman, "Momentum, Impulse and collisions," in *Sears and Zemansky's University Physics with Modern Physics Technology Update Hugh D. Young Roger A. Freedman Thirteenth Edition*, 13<sup>th</sup> ed. Harlow: Pearson, 2014, pp. 267-305
- [36] J. M. Smith, H. C. Van Ness, M. M. Abbott and M.T. Swihart, "The First Law and Other Basic Concepts," in *Introduction to Chemical Engineering Thermodynamics*, 8<sup>th</sup> ed. Boston: McGraw-Hill Education, 2018, pp. 24-67.
- [37] "Vertical multi-stage centrifugal pumps."  
[https://www.desmi.com/media/ymhcdabp/t1392uk\\_dpv.pdf](https://www.desmi.com/media/ymhcdabp/t1392uk_dpv.pdf) (accessed Apr. 14, 2021)
- [38] "Piston compressor Luna 4.0/360." [Piston compressor Luna 4.0 / 360 - PS Auction - We value the future - Largest in net auctions](#) (accessed Apr. 17, 2021)
- [39] "CombiPress-PFHM." [CombiPress PFMH | Pressure and continuous level measurement | Baumer Switzerland](#) (accessed May.10,2021).
- [40] "Photron APX RS high-Velocity." [PHOTRON | FASTCAM APX-RS High Velocity Camera \(techimaging.com\)](#) (accessed Apr. 17.04.2021)

## References

- [41] “Multiled QT- Exchangeable lenses.” MULTILED QT - Motion Engineering | High Velocity Cameras | Imaging (highvelocityimaging.com) (accessed Apr. 17.04.2021)
- [42] “12X Zoom Lens System.” 12X Zoom Lens System - High Mag Zoom & Fixed Lenses | Navitar (accessed Apr. 25, 2021).
- [43] R. Paschotta. “Numerical Aperture.” RP Photonics Encyclopedia - numerical aperture, NA, optical fiber, lens, objective, acceptance angle (rp-photonics.com) (accessed Apr. 25, 2021).
- [44] “Laser components.” LASER COMPONENTS Deutschland (accessed Apr. 25, 2021).
- [45] “Pro Builder –5500w strømaggregat/ generator.” Pro Builder - 5500w strømaggregat / generator | Anvema selger verktøy og maskiner med deg i fokus! (Accessed Apr. 14, 2021).
- [46] ”FLIR i7 Camera 140 x 140 Resolution/9Hz – 60101-0301.” FLIR i7 IR Camera 140 x 140 Resolution/9Hz - 60101-0301 (jjstech.com) (accessed Apr. 22, 2021).
- [47] ”Weighing Scale Machine. ” Weighing Scale Machine - SF-400 Weighing Scale Machine Wholesale Trader from Delhi (viyashaenterprise.com) (accessed Apr. 21, 2020).
- [48] netonnet “Kompakt lasermåler med triple 360°-lasere.” Bosch Professional GLL 3-80 - Kompakt lasermåler med triple 360°-lasere (netonnet.no) (accessed May 07, 2021).
- [49] “Drag force” Lumen Physics.” Drag Forces | Physics (lumenlearning.com) (accessed May.7, 2021).

## 9 Appendices

Appendix A Project description

Appendix B Property relations for the isentropic flow of ideal gases

Appendix C Derivation of model for droplet trajectory and its heat transfer modes

Appendix D MATLAB-code for droplet trajectory, heat and mass transfer modeling

Appendix E MATLAB- code for Image processing

Appendix F Calculation of initial conditions

Appendix G Test matrix template

Appendix H Simulation plots

Appendix I Project Scheduling

# Appendix A



Faculty of Technology, Natural Sciences and Maritime Sciences, Campus Porsgrunn

## FMH606 Master's Thesis

**Title:** Experimental investigation of artificial snow production in marginal geographic conditions

**USN supervisor:** Joachim Lundberg

**External partner:** Inventor Odd Ivar Lindløv

### Task background:

A Norwegian inventor has developed a system for generating artificial snow. The concept / private initiative is to optimize snow production for geographical locations where so-called 'marginal' conditions for snow production dominate the weather picture. Snow production is simple; one sprays water under pressure into cold air. If the water is cold enough, if the air is cold enough, if the drops are small and if the wet bulb temperature is low you will produce snow. In addition, there are factors such as throw length / height, wind, etc. that affect the actual production and the amount of snow produced.

A cooling tower located upstream of the inlet to the snow production plant will lower the temperature of the water. Air temperature and humidity are more difficult to deal with, but you can increase the speed to accelerate the heat transfer from water droplet to air. Atomization of sprays, and then large sprays, is a 'somewhat' strange field. Traditional snow cannons use small nozzles with high pressure; this is a fairly safe method of making 'small enough' drops to make snow. The problem, however, is that the way these nozzles work, they give both small and large drops in the same spray; in addition, there are a number of non-spherical droplets in the spray, which then give volume and mass which do not follow an assumed evaporation process from a droplet surface. Artificial snow is in a way an opposite process of natural snow.

What can accelerate this process is lower temperature and / or - smaller droplet size which will have a smaller surface and hence 'less' need to exchange energy with the surroundings. The literature describes an optimal droplet size in the range 200 - 700 microns. This is to provide a compromise between cooling rate and drop rate; the larger the drop, the longer it has to fall to freeze and vice versa.

Nozzle suppliers often supply the nozzles used by snow production equipment suppliers, and this is unfortunately a generic type of nozzle where drop control is probably not as critical. Some simple tests have been performed on the concept, which showed that at a drop height of about 1.5 meters, with a fountain that kept about + 6 ° C, an air temperature of -3.2 ° C and a humidity of 84% RH. The water pressure was 8 barg, the air pressure 4 barg and the amount of water about 420 kg / h. Then snow was produced with a quality between 3 and 4 according to the "snow scale" which goes from 1 - 9 (1 is powder, 9 is almost rain). Experiments performed in Trondheim in 2017 (NTNU, Odd Erlend Hansen Berg), with fan gun, under similar conditions (however, the water temperature was + 2 ° C) were in borderland for production under these conditions. It is thus convinced that the potential for using self-produced nozzles in snow production will be able to compete, if not exceed, the capacity of fan guns - at a fraction of the price.

Further plan is to complete the development of specific design, including droplet size optimization (against wet ball temperature for marginal production) and the interface between the air used for nucleation and the water droplets.

Small-scale testing is performed as soon as climatic conditions allow. A launch of the concept is then planned for the spring of 2021, with the hope of installing / modifying facilities in the autumn of 2021 for snow production in the 2021/22 season.

**Task description:**

The student will perform a literature study of artificial snow production and perform an experimental study on snow generation with the new system.

**Student category:** PT or EET students

**Is the task suitable for online students (not present at the campus)?** No

**Practical arrangements:**

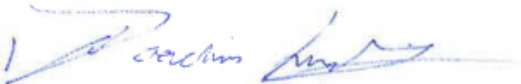
The experimental research involve outdoor activity and the candidate needs warm socks.

**Supervision:**

As a general rule, the student is entitled to 15-20 hours of supervision. This includes necessary time for the supervisor to prepare for supervision meetings (reading material to be discussed, etc).

**Signatures:**

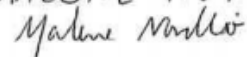
Supervisor (date and signature):

29/1-21 

Student (write clearly in all capitalized letters):

MALENE NORDBO

Student (date and signature):

29.01.2021 

## Appendix B

From thermodynamics, a unit mass of a fluid that undergoes a reversible process in a closed system, the first law of thermodynamics can be written as shown in Equation (B.1).

[24, p. 182]

$$dU = dQ_{rev} - Pdv \quad (B.1)$$

The enthalpy for a closed-system reversible process is given by Equation (B.2).

$$dH = dU + d(PV) \quad (B.2)$$

$$dH = dU + PdV + VdP$$

By inserting the internal energy term  $dU$  in Equation (B.2), it gives the following expression presented in Equation (B.3).

$$\begin{aligned} dH - PdV - VdP &= dQ_{rev} - Pdv \\ dQ_{rev} &= dH - VdP \end{aligned} \quad (B.3)$$

Here, the enthalpy can be written as  $dH = C_p dT$ . Also, the formula for an ideal gas is known as  $V = RT/P$ . Equation (B.3) is thereby written as shown in Equation (B.4).

$$dQ_{rev} = C_p dT - \frac{RT}{P} dP \quad (B.4)$$

By dividing each term on the absolute temperature, Equation (B.5) is obtained.

$$\frac{dQ_{rev}}{T} = C_p \frac{dT}{T} - R \frac{dP}{P} \quad (B.5)$$

As the change of entropy is known as  $dS = dQ_{rev}/T$ , Equation (B.5) could be transformed to Equation (B.6).

$$dS = C_p \frac{dT}{T} - R \frac{dP}{P} \text{ or } dS = \frac{C_p}{R} \frac{dT}{T} - d \ln P \quad (B.6)$$

Integrating Equation (B.6) from the initial temperature and pressure to the final state gives the following relation.

$$\frac{\Delta S}{R} = \int_{T_0}^T \frac{C_p}{R} \frac{dT}{T} - \ln \frac{P}{P_0} \quad (B.7)$$

Further, the gas constant and specific heat ratio can be written from thermodynamics as shown in Equation (B.8). [24, p. 182]

$$R = C_p - C_v \text{ and } k = \frac{C_p}{C_v} \quad (B.8)$$

The following expression is obtained by inserting the specific heat ratio into the gas constant formula (B.8). [24, p. 183]

$$\frac{R}{C_p} = 1 - \frac{1}{k} = \frac{k-1}{k} \quad (\text{B.9})$$

The heat capacity for constant pressure is thereby written as shown in Equation (B.10).

$$C_p = \frac{kR}{k-1} \quad (\text{B.10})$$

For ideal gas and constant heat capacities for an isentropic process, the following expression is developed. [24, p. 183]

$$\frac{P_0}{P} = \left(\frac{T_0}{T}\right)^{\frac{k}{k-1}} = \left(\frac{\rho_0}{\rho}\right)^k \quad (\text{B.11})$$

One important parameter to understand in the compressible flow study is the velocity of sound. By definition, the velocity of sound represents how a pressure wave travels through a fluid. [23, p. 843]

A pressure wave can be generated by disturbances within the medium, which may increase the local pressure. An expression for the velocity of sound is therefore of interest. A filled pipe with fluid with zero flow is considered, as shown in Figure 0.1. An applied disturbance at one side of the fluid generates a pressure wave that travels with sound velocity in the opposite direction. Imagine that a control volume is attached to the pressure wave. [23, p. 843]

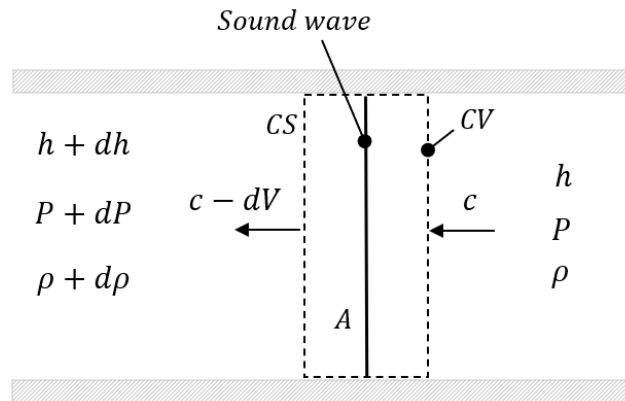


Figure 0.1: Pressure wave and its control volume [23, p.843]

First, the conservation of mass for this is applied to the control volume expressed in Equation (B.12).

$$\dot{m}_{in} = \dot{m}_{eff} \quad (\text{B.12})$$

$$\rho A c = (\rho + d\rho)(c - dv)A$$

Solving Equation (B.12) gives the following expression shown in Equation (B.13).

$$0 = d\rho c - \rho c v \quad (\text{B.13})$$

The energy balance for steady-flow is also applied as shown in Equation (B.14).

$$q_{in} + w_{in} + (h_{0in} + gz_{in}) = q_{eff} + w_{eff} + (h_{0eff} + gz_{eff}) \quad (\text{B.14})$$

Heat  $q$ , work  $w$ , and potential energy  $gz$  are neglected across the boundary. The stagnation enthalpy  $h_0$ , which represents the total energy of a flowing fluid is expressed in Equation (B.15).

$$h_0 = h + \frac{v^2}{2} \quad (\text{B.15})$$

By combining the Equation (B.14) and (B.15) across the pressure wave, expression (B.16) is obtained.

$$h + \frac{c^2}{2} = h + dh + \frac{(c - dV)^2}{2} \quad (\text{B.16})$$

The higher-order term  $dV$  is significantly small and is thereby neglected, which give the following expression. [23, p. 843]

$$dh - c dV = 0 \quad (\text{B.17})$$

Also, the second law of thermodynamics is used. [23, p. 844]

$$T ds = dh - \frac{dP}{\rho} \quad (\text{B.18})$$

By assuming that the pressure wave does not generate a significant amount of heat, the system can be assumed to be isentropic ( $\Delta S = 0$ ) which yields the Equation (B.19).

$$dh = \frac{dP}{\rho} \quad (\text{B.19})$$

The expression for the speed of sound  $c$ , is finally obtained by combining Equation (B.13), (B.16), and (B.19).

$$c^2 = \left(\frac{\partial P}{\partial \rho}\right)_s \text{ or } c = \sqrt{\left(\frac{dP}{d\rho}\right)_s} \quad (\text{B.20})$$

The subscript  $s$ , indicates constant entropy. Equation (B.20) can also be written as follows.

$$c^2 = k \left(\frac{\partial P}{\partial \rho}\right)_T = k \left[\frac{\partial(\rho RT)}{\partial \rho}\right]_\rho = kRT \quad (\text{B.21})$$

$$c = \sqrt{kRT} \quad (\text{B.22})$$

From Equation (B.22), it was possible to state that sound velocity is a function of absolute temperature. Further, it is known from physics that the Mach number is the local velocity divided by the velocity of sound. [23, p. 844]

$$Ma = \frac{\text{local speed}}{\text{local speed of sound}} = \frac{v}{c} \quad (\text{B.23})$$

The Mach number is used to describe the fluid flow regime. When  $Ma=1$ , the flow is said to be sonic, and the local velocity of sound is equal to the local velocity. If  $Ma < 1$ , the flow is subsonic, and finally, if  $Ma > 1$ , the flow is supersonic. [23, p. 844]



Further, a relation between temperature, density, and pressure is to be investigated. If a fluid flow from point one to point two is considered, where point two is assumed to be a stagnation point, the velocity  $v_0$ , comes to rest at zero. It is brought to rest adiabatically, which means that no heat is transferred. The conservation of energy is used to develop the properties. The following expression is obtained by assuming steady flow, zero work, heat, and change in elevation. [23, p. 850]

$$C_p T + \frac{V_1^2}{2} = C_p T_0 + \frac{V_0^2}{2} \quad (\text{B.24})$$

Equation (B.24) is solved for the stagnation temperature  $T_0$ .

$$\frac{T_0}{T} = \frac{V^2}{2C_p T} + 1 \quad (\text{B.25})$$

Further, the expression for the velocity of sound is used in the velocity term  $V$ . By inserting Equation (B.22) into Equation (B.25), the expression for the stagnation temperature ratio is found. [23, p. 850]

$$C_p T = \left[ \frac{kRT}{k-1} \right] = \frac{c^2}{k-1} \quad (\text{B.27})$$

$$\frac{T_0}{T} = \frac{(k-1)}{2} Ma^2 + 1 \quad (\text{B.28})$$

By inserting Equation (B.28) into Equation (B.11), the ratio of stagnation to static pressure  $P_0$ , and density  $\rho_0$ , is found.

$$\frac{P_0}{P} = \left[ 1 + \frac{k-1}{2} Ma^2 \right]^{\frac{k}{k-1}} \quad (\text{B.29})$$

$$\frac{\rho_0}{\rho} = \left[ 1 + \frac{k-1}{2} Ma^2 \right]^{\frac{1}{k-1}} \quad (\text{B.30})$$

The density  $\rho$ , of the compressible fluid, is also determined by using (B.31). [23, p. 859]

$$\rho = \frac{P}{RT} \quad (\text{B.31})$$

## Appendix C

First, a free body diagram is drawn of a general water droplet with a defined coordinate system, as shown in Figure 2.11. Here, the trajectory is a function of drag, gravity, and buoyancy force. The droplet is assumed to be spherically shaped throughout the trajectory.

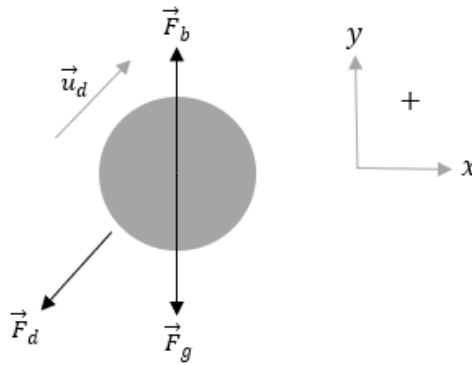


Figure 2.11

The drag force,  $\vec{F}_d$ , is given by Equation (C.1), the buoyancy force  $\vec{F}_b$ , is given by Equation (C.2), and finally, the gravity force  $\vec{F}_g$ , is given by Equation (C.3). [49]

$$\vec{F}_d = \frac{1}{2} C_d \rho_a v_d^2 A_d \quad (\text{C.1})$$

$$\vec{F}_g = m_d g \quad (\text{C.2})$$

$$\vec{F}_b = \rho_a V_d g \quad (\text{C.3})$$

The formula for calculating the volume and the droplet area is given in Equation (C.4) and (C.5). [27]

$$V_d = \frac{4}{3} \pi r_d^3 = \frac{4}{3} \pi \frac{D^3}{8} = \frac{1}{6} \pi D^3 \quad (\text{C.4})$$

$$A_d = \pi r^2 = \frac{1}{4} \pi D^2 \quad (\text{C.5})$$

Newton's second law is further applied to sum the forces in x and y-direction.

$$F_{tot,x} = \vec{F}_d \quad (\text{C.6})$$

$$F_{tot,y} = -\vec{F}_g + \vec{F}_b - \vec{F}_d \quad (\text{C.7})$$

The differential equations for calculating the acceleration of a droplet in x and y-direction are obtained by combining Equation (C.4), (C.5), (C.6) and (C.7). The expression for the acceleration is presented in Equation (C.8) and (C.9). [32]

$$\frac{d^2x}{dt^2} = -\frac{3}{4} \frac{C_d}{D} \frac{\rho_{mix}}{\rho_d} \left( \frac{dx}{dt} - u_{rx} \right) \sqrt{\left( \frac{dx}{dt} - u_{rx} \right)^2 + \left( \frac{dy}{dt} - u_{ry} \right)^2} \quad (C.8)$$

$$\frac{d^2y}{dt^2} = g \left( \frac{\rho_{mix}}{\rho_d} - 1 \right) - \frac{3}{4} \frac{C_d}{D} \frac{\rho_{mix}}{\rho_d} \left( \frac{dy}{dt} - u_{ry} \right) \sqrt{\left( \frac{dx}{dt} - u_{rx} \right)^2 + \left( \frac{dy}{dt} - u_{ry} \right)^2} \quad (C.9)$$

The density of mixed air around the droplet is  $\rho_{mix}$ , and  $\rho_d$ , is the density of the droplet. The droplet velocity in the x-direction  $\frac{dx}{dt}$  and y-direction  $\frac{dy}{dt}$ , is called  $u_x$  and  $u_y$ , respectively. Further, the velocity of air in the x-direction is represented by  $u_{rx}$ , and the air velocity in the y-direction is represented by  $u_{ry}$ . Both of these are expressed in Equation (C.10) and (C.11). [32]

$$u_{rx} = u_{x,w} + u_{x,air} \quad (C.10)$$

$$u_{ry} = u_{y,w} \quad (C.11)$$

The wind speed is decomposed in x and y-direction, denoted  $u_{x,w}$  and  $u_{y,w}$ . In this paper, the air represents a mixture of entrained air, airflow, and water flow from the nozzle and is denoted  $u_{x,air}$ . To determine the droplet velocity, Equation (C.12) is used.

$$u_d = \sqrt{u_x^2 + u_y^2} \quad (C.12)$$

The drag coefficient  $C_d$ , which is a function of the Reynolds number  $Re$ , is also calculate by using the Schiller Neumann model as shown in (C.13). [33]

$$C_d = \begin{cases} \frac{24}{Re}, & Re \leq 1 \\ \frac{24}{Re} (1 + 0.15Re^{0.687}), & 1 < Re \leq 1000 \\ 0.44, & Re > 1000 \end{cases} \quad (C.13)$$

The Reynolds number, which is the ratio for the inertia and viscous forces around the droplets, is calculated by Equation (C.14)

$$Re = \frac{u_{eff} D}{\nu_a} \quad (C.14)$$

Here,  $\nu_a$ , is the kinematic air viscosity and  $u_{eff}$ , represents the effective velocity, which is the droplet's velocity relative to the airflows (nozzle air and air-entrained) in the system. The effective droplet velocity is decomposed and calculated by combining Equation (C.15), (C.16), and (C.17).

$$u_{eff} = \sqrt{u_{x,eff}^2 + u_{y,eff}^2} \quad (C.15)$$

$$u_{x,eff} = |u_x - u_{x,w} - u_{x,air}| \quad (C.16)$$

$$u_{y,eff} = |u_y - u_{y,w}| \quad (C.17)$$

The kinematic viscosity of air  $\nu_a$ , was found during premade experiments as presented in Equation (C.18). [32]

$$\nu_a = \frac{1}{(80711.7 - 766.15 \cdot T_{mix})} \quad (C.18)$$

#### *Heat transfer expression*

Figure 2.12 illustrates the heat transfer modes before and after the droplet reaches a temperature of 0°C. First, the heat loss forced by convection  $Q_c$ , is given by Equation (C.19).

$$Q_c = h_c(T_d - T_{mix}) \quad (C.19)$$

Here, the convective heat transfer coefficient  $h_c$ , of the droplet is presented in Equation (C.20).

$$h_c = \frac{Nu k_a}{D} \quad (C.20)$$

Thermal conductivity  $k_a$ , characterizes the boundary layer. It was found during premade experiments for air between -25 to 5 °C which is given in Equation (C.21). [32]

$$k_a = 8 \cdot 10^{-5} T_{mix} + 0.0244 \quad (C.21)$$

Further, the Nusselt number  $Nu$ , represented the ratio of convection to the pure conduction heat transfer of the droplet and calculated using Equation (C.22).

$$Nu = 2.0 + 0.6Pr^{0.33}Re^{0.5} \quad (C.22)$$

Prandtl number  $Pr$ , is the ratio of momentum and thermal diffusivities, given in Equation (C.23).

$$Pr = \frac{\mu_a}{\rho_{mix} \alpha} \quad (C.23)$$

Also, the dynamic viscosity of air  $\mu_a$ , is given by Equation (C.24). [32]

$$\mu_a = \mu_o \left[ \frac{T_\infty + 120}{T_{mix} + 273.15 + 120} \left( \frac{T_{mix} + 273.15}{T_\infty} \right)^{1.5} \right] \quad (C.24)$$

To determine the thermal diffusivity of air  $\alpha$ , Equation (C.25) is used. [32]

$$\alpha = \frac{1}{57736 - 585.78 T_{mix}} \quad (C.25)$$

The evaporative heat loss  $Q_e$ , was given by Equation (C.26). This heat transfer was assumed to process from positive centigrades until the droplet reached 0°C. It was also assumed that the droplet was converted to solid ice at this final state.

$$Q_e = h_c \left( \frac{Pr}{Sc} \right)^{0.63} \frac{\epsilon H_{vap}}{P C_{p,a}} \left( P_d - \left( \frac{RH}{100} \right) P_{sat,T_{mix}} \right) \quad (C.26)$$

Here,  $H_{vap}$ , is the latent heat of water,  $P_d$ , is the saturated vapor pressure,  $C_{p,a}$ , is the specific heat capacity of air and  $RH_{mix}$ , is the relative humidity of the mixed air. The ratio of the molecular weight of vapor and dry  $\epsilon$ , is further calculated by Equation (C.27). [32]

$$\epsilon = \frac{M_w}{M_a} \quad (C.27)$$

The Schmidt number  $Sc$ , which is the ratio of momentum and mass diffusivities, is determined by Equation (C.28).

$$Sc = \frac{\mu_a}{\rho_{mix} D_{ab}} \quad (C.28)$$

The binary diffusion coefficient  $D_{ab}$ , is calculated using Equation (2.7). Using the binary diffusion coefficient at one atmosphere where substance A is water and B is air, give the following relation shown in Equation (C.29). [8, p. 867] [9, p. 936]

$$D_{ab} = 0.26 \cdot 10^{-4} \left( \frac{T_{mix} + 273.15}{273} \right)^{1.5} \quad (C.29)$$

The cooling process of the droplet due to convection and evaporation heat loss from the droplet surface is expressed by Equation (C.30). [32]

$$\rho_a c_{p,d} \frac{d(V_d T_d)}{dt} = -A_s (Q_e + Q_c) \quad (C.30)$$

Here, the  $A_s$ , is the surface area of a spherical droplet,  $c_{p,d}$ , is the specific heat capacity of the droplet. The surface area  $A_s$ , is determined as shown in Equation (C.31). [27]

$$A_s = 4\pi r_d^2 \quad (C.31)$$

Also, the evaporation rate  $\dot{m}_v$ , from the droplet surface is found by using Equation (C.32)

$$\dot{m}_v = \frac{Q_e}{H_{vap}} A_s \quad (C.32)$$

Further, the decrease of droplet diameter  $D$ , as a function of evaporation, is calculated using Equation (C.33).

$$\frac{dD}{dt} = -\frac{2\dot{m}_v}{\rho_d \pi D^2} \quad (\text{C.33})$$

The change in droplet temperature is finally expressed as given in Equation (C.34) [32]

$$\frac{dT_d}{dt} = \left[ \frac{3\dot{m}_v}{4\pi\rho_d r_d^3} \right] T_d - \frac{3}{\rho_d c_{p,d} r_d} (Q_e + Q_c) \quad (\text{C.34})$$

# Appendix D

```

%% Solver for droplet trajectory and its heat transfer modes %%
%% Created by Malene Nordbø, March 2021

clear all;
clc;

global theta Mw Mair R RHOd RHOamb T0 Ta Hvap Hfus Cpw Cpair E RH_0 uxwind
uywind theta To my0 g P Mwair Tf r0 mair0 Re uair0 md0 ud0 Tnozzle Psata
Psatn D0 ynozzle yent Dwn C Nd Vd

%Call all the constants used in the program
%-----
constant

%Wind velocity in x and y-driection
%-----
uxwind = 0; % [0 .2 .4 .6 .8 1 1.2 1.4]; % Wind velocity in x direction [m/s]
uywind = 0; % Wind velocity in y direction [m/s]

%Time span
%-----
t=linspace(0,30,10^6);

% Initial conditions
%-----
mair0 = 0.004983; % Initial air flow [kg/s]
uair0 = 307.9; % Initial air velocity [m/s]
md0 = 0.0166; % Initial water mass flow [kg/s]
ud0 = 9.43; % Initial droplet velocity [m/s]
theta = 50; % Air cone angle [degrees]
theta_n = 50; % Nozzle cone
x01 = 0; %x position at t=0 [m]
x02 = ud0; %cos(theta_n/180*pi);% ud0;%* %dxdt at t=0 [m/s]
y01 = 1.324; %y position at t=0 [m]
y02 = 0; %*sin(theta_n/180*pi) %dydt at t=0 [m/s]
r0 = 0.0105/2; %Radius of airflow-exit at the nozzle (at t=0) [m]
T0 = 1; %Droplet initial temperature[C]

for D0 = [40e-06, 50e-06, 120e-06, 170e-06, 360e-06]; %Droplet initial
diameter based on image processing [m];

Vd = 4/3*pi*(D0/2)^3; % Volume per droplet[m^3]
Nd = md0/(RHOd*Vd); % Number of droplets [droplets/s]

X0 = [x01;x02;y01;y02;D0;T0];

% Solver
%-----
option = odeset('reltol',1e-12,'abstol',1e-14);
[t,X] = ode45(@derZ,t,X0,option);

% Unpacking result matrix
%-----
y =X(:,3); % y position

```

```

Stop = y>0.0000000001;
x = X(:,1); % x position
ux = Stop.*X(:,2); % x velocity
y = Stop.*X(:,3); % y position
uy = Stop.*X(:,4); % y velocity
D = X(:,5); % Droplet diameter
T = X(:,6); % Droplet temperature

% Droplet velocity
%-----
ud = sqrt(ux.^2+uy.^2); %[m/s]

% Relative humidity and evaporation rate
%-----
% [~,RH1,dvap1,uxair1] = cellfun(@(t,X) derZ(t,X.'), num2cell(t),
num2cell(X,2), 'uni', 0);
% RH = cell2mat(RH1);
% dvap = cell2mat(dvap1);
% uxair = cell2mat(uxair1);

% Plotting results
%-----

hold on
figure(1);
plot (x,y);
title ('Position');
grid on;
xlabel('X-position [m]');
ylabel('Y-position [m]');
xlim([-0.5 2.5]);
ylim([-0.5 2]);
legend ('40e-06', '50e-06', '120e-06', '170e-06', '360e-06');
%
hold on
figure(2);
plot (t,y);
title ('Flight time');
grid on;
xlabel('Time [s]');
ylabel('Y-position [m]');
legend ('40e-06', '50e-06', '120e-06', '170e-06', '360e-06');
%
hold on
figure(3);
plot (x,ud);
title ('Velocity vs x-position');
grid on;
xlabel('X-Position [m]');
ylabel('Velocity [m/s]');
xlim([-1 20]);
ylim([-1 20]);
legend ('40e-06', '50e-06', '120e-06', '170e-06', '360e-06');
%
hold on
figure(4);
plot (t,T);

```



```

title ('Temperature vs Time');
grid on;
xlabel('Time [s]');
ylabel('Temperature [C]');
legend ('40e-06', '50e-06', '120e-06', '170e-06', '360e-06');
%
hold on
figure(5);
plot (x,T);
title ('Temperature vs Displacement');
grid on;
xlabel('X-direction [m]');
ylabel('Temperature [C]');
legend ('40e-06', '50e-06', '120e-06', '170e-06', '360e-06');
%
hold on
figure(6);
plot (t,D);
title ('Droplet diameter');
grid on;
xlabel('Time [s]');
ylabel('Diameter [m]');
legend ('40e-06', '50e-06', '120e-06', '170e-06', '360e-06');
%
hold on
figure(7);
plot (t,dvap);
title ('Evaporation rate');
grid on;
xlabel('time [s]');
ylabel('Evaporation [kg/s]');
legend ('40e-06', '120e-06', '240e-06', '360e-06');
legend ('40e-06');
%
% Uncomment line 67-70 and comment out line 75-134 to plot Figure 7-9
% figure(8);
% plot (t,RH);
% title ('Relative humidity');
% grid on;
% xlabel('time [s]');
% ylabel('RH [%]');
% legend ('50e-06');
%
% hold on
% figure(9);
% plot (t,ud, t,uxair);
% title ('Velocity of droplet');
% grid on;
% xlabel('Time [s]');
% ylabel('Velocity[m/s]');
% legend ('40e-06', 'Mixed air velocity');
%
end

%%%%%%%%%%%%%%%%%%%%%%%%%%%%%%%%%%%%%%%%%%%%%%%%%%%%%%%%%%%%%%%%%%%%%%%%

```

```

%% Equations which is exported to runmod-code %%
%% Created by Malene Nordbø, March 2021

function [dXdt, RH, dvap, uxair] = derZ(t,X)

global RHOd Ta Hvp Mair RHOamb Cpw Cpair uxwind uywind g Tf theta r0
mair0 uair0 md0 ud0 Tnozzle P D0 ynozzle yent Mw Dwn C Nd Vd
%constant

%Splits the X-vector in droplet diameter, velocity and temperature
%-----
[m,n] = size(X);
%dXdt = zeros(m,n); % This initialises dXdt to be a column vector
%16 degrees angle for air nozzle and 10.5 mm at mach 1

x = X(1,1); % X position
ux = X(2,1); % X velocity
y = X(3,1); % Y position
uy = X(4,1); % Y velocity
D = X(5,1); % Droplet diameter
T = X(6,1); % Droplet temperature

% Wind velocity relative to moving object
%-----
ud = (ux^2+uy^2)^0.5; % Droplet speed [m/s]
mass_e = C*(mair0/(r0^2))*x + C*((md0/(Dwn))*(RHOamb/RHOd)^0.5)*x; %Mass
entrained [kg/s]
uxair = (md0*ud0+mair0*uair0-md0*ud)/(mair0+mass_e); %air velocity based on
momentum balance

% Mixed air temperature and density
%-----
Tmix =
(mair0*Cpair*(Tnozzle+273.15)+mass_e*Cpair*(Ta+273.15))/(Cpair*(mass_e+mair
0))-273.15; % Temperature of mixed air [centigrades]
RHOmix = P/287.04/(Tmix+273.15); %Density air[kg/m3]

%Change of relative humidity of mixed air
%-----
    if Tmix > 0
        Psat = 611.15*exp((18.678-(Tmix/234.5))*Tmix/(257.14+Tmix));
%Saturated water pressure at Tmix [Pa]
    elseif Tmix < 0
        Psat = 611.15*exp((23.036-(Tmix/333.7))*Tmix/(279.82+Tmix));
%Saturated water pressure at Tmix [Pa]
    end

nwater = mair0/Mair*ynozzle + mass_e/Mair*yent + Nd*(RHOd*4/3*pi*((D0/2)^3-
(D/2)^3)/Mw); % Moles of water in the mixed air [mole]
ntot = (mair0 + mass_e)/Mair + nwater; % Total number of moles
Pw = nwater/ntot*P; %Partial pressure of water [Pa]
RH = Pw/Psat*100; % Relative humidity [%]

% Wind velocity relative to moving object
%-----
Urx = 0+uxwind+uxair; %[m/s]
Ury = 0+uywind; %[m/s]

```

```

% Effective droplet velocity
%-----
u_xeff = ux-uxwind-uxair;
u_yeff = uy-uywind;

ueff = (u_xeff^2+u_yeff^2)^0.5; % [m/s]

% Kinematic viscosity
%-----
vis = 1/(80711.7-766.15*Tmix); % [m^2/s]

% Reynolds number
%-----
Re = D*ueff/vis;

% Drag coefficient
%-----
if y>0.000000000001
Cd = Drag(Re);
else
    Cd=0;
end

%Volume and surface area of droplet
%-----
rd = D/2;
As = 4*pi*rd^2; % [m^2]

%Evaporation rate from droplet`s surface [kg/s]
%-----
[Qc,Qe] = heat(D,T,Re,Tmix,Psat,RHOMix,RH); %%Qe til null

dvap = Qe/Hvap*As;

%Change of droplet diameter
%-----
dDdt = -dvap/RHod*2/(pi*D^2);

%Change in droplet temperature
%-----
dTdt = (3*dvap/(4*pi*RHod*rd^3))*T-(3/(RHod*Cpw*rd)*(Qc+Qe));

% Reformulating the second order differential equations into a system of
% first order differential equations
%-----
if y>0.000000000001
    dxdt = ux;
    dxdt = (-3/4)*(Cd/D)*(RHOMix/RHod)*(ux-Urx)*((ux-Urx)^2+(uy-
Ury)^2)^0.5;
    dydt = uy;
    dydt = g*((RHOMix/RHod)-1)-((3/4)*(Cd/D)*(RHOMix/RHod)*(uy-Ury)*((ux-
Urx)^2+(uy-Ury)^2)^0.5);
else
    uy = 0;
    ux = 0;

```

```

    dxdt = 0;
    dxdttt = 0;
    dydt = 0;
    dydttt = 0;
    dDdt = 0;
    dTdt = 0;
end

dXdt = [dxdt; dxdttt; dydt; dydttt; dDdt; dTdt];

end

%%%%%%%%%%%%%%%%%%%%%%%%%%%%%%%%%%%%%%%%%%%%%%%%%%%%%%%%%%%%%%%%%%%%%%%%

% % Drag coefficient function % %
% % Created by Malene Nordbø, March 2021

function Cd=Drag(Re)

if (Re) < 1
    Cd=24/(Re);
elseif 1<(Re)<=1000
    Cd = 24/(Re) * (1+0.15*(Re)^0.687);
else (Re)>1000
    Cd = 0.44;
end
end

%%%%%%%%%%%%%%%%%%%%%%%%%%%%%%%%%%%%%%%%%%%%%%%%%%%%%%%%%%%%%%%%%%%%%%%%

% % Equations for heat transfer % %
% % Created by Malene Nordbø, March 2021
function [Qc,Qe]=heat(D,T,Re,Tmix,Psat,RH0mix,RH)

global P E Hvap Cpair To my0 Tf RH_0

Td=T; %Droplet temperature
alpha = 1/(57736-585.78*Tmix); %Thermal diffusivity of air [m^2/s]
Dab = 0.26E-4*((Tmix+273)/273)^1.5; % Diffusivity of air-water vapour
[m^2/s]

    if Td > 0
        Pd = 611.15*exp((18.678-(Td/234.5))*Td/(257.14+Td)); %Saturated
water pressure at Tmix [Pa]
    elseif Td < 0
        Pd = 611.15*exp((23.036-(Td/333.7))*Td/(279.82+Td)); %Saturated
water pressure at Tmix [Pa]
    end
%Dynamic viscosity of air
%-----
mya = my0*((To+120)/(Tmix+273.15+120))*((Tmix+273.15)/To)^1.5; %[Pa.s]

%Prandtl number
%-----
Pr = mya/(RH0mix*alpha);

```

```

%Nusselt number for droplet
%-----
Nu = 2.0+0.6*Pr^0.33*Re^0.5;

%Schmidt number
%-----
Sc = mya/(RH0mix*Dab);

%Thermal conductivity of air for -25 to 5 C
%-----
ka = 8E-5*Tmix+0.0244; %[W/m.K]

%Convective heat transfer coefficient of the droplet
%-----
hc = Nu*ka/D; %[W/m^2.K]

%Convective heat loss
%-----
Qc = hc*(Td-Tmix); %[W/m^2]

%Evaporative heat loss
%-----
if T>Tf
    Qe = hc*(Pr/Sc)^0.63*E*Hvap/(P*Cpair)*(Pd-(RH/100)*Psat); %[W/m^2]
else Qe = 0;
end

%%%%%%%%%%%%%%%%%%%%%%%%%%%%%%%%%%%%%%%%%%%%%%%%%%%%%%%%%%%%%%%%%%%%%%%%

% % List of constants used % %
% % Created by Malene Nordbø, March 2021

RH_0 = 79; %Relative humidity [%]
Ta = -3; % Ambient air temperature [centigrades]
Tnozzle = -37.5; % Temperature of air coming from nozzle [centigrades]
Psata = (RH_0/100)*611.15*exp((23.036-(Ta/333.7))*Ta/(279.82+Ta)); % Vapor
pressure for ambient air [Pa]
Psatn = 611.15*exp((23.036-(Tnozzle/333.7))*Tnozzle/(279.82+Tnozzle)); %
Saturated vapor pressure for nozzle air[Pa]
P = 101325; %Ambient air pressure [Pa]
ynozzle = Psatn/P; %Fraction of water in air from nozzle
yent = Psata/P; %Fraction of water in ambient air
To = 296.16; %Reference temperature for thermal diffusivity [K]
Tf = 0; %Freezing temperature
Mw = 0.018; %Molar weight water [kg/mol]
Mair = 0.02896; %Molar weight of dry air [kg/mol]
R = 8.3144; %Gas constant [J/mol.K]
RH0d = 1000; %Density liquid water [kg/m3]
RH0amb = P/287.04/(Ta+273.15); %Density air[kg/m3]
Hvap = 22.6E+5; %Latent heat of water [J/kg]
%Hfus = 3.34E+5; %Latent heat of fusion [J/kg] add if the code is to be
%developed further
Cpw = 4180; % Specific heat of liquid water [J/kg.K]
Cpair = 1.005; %Specific heat of air [J/kg.K]
%kw = 0.55575; %Thermal conductivity of water [W/m.K]
my0= 1.8325E-5; %Reference dynamic viscosity for thermal diffusivity [Pa.s]

```

```
E = Mw/Mair; %Ratio of molecular weight of water vapour and dry air
g = 9.81; %Gravity [m/s^2)
Dwn = 40E-6; %Nozzle diameter of water sheet [m]
C = 0.4;% Entrainment constant [-]
```

# Appendix E

```

%% Image processing code %%
%% Created by Joachim Lundberg April 2021

%% %%%%%%%%%%%%%%%%%%%%%%%%%%%%%%%%%%%%%%%%%%%%%%%%%%%%%%%%%%%
%% clear all
%% PROPS=[0 0 0 0]
%% save('2021MaleneDATA.mat','PROPS')
%% %%%%%%%%%%%%%%%%%%%%%%%%%%%%%%%%%%%%%%%%%%%%%%%%%%%%%%%%%%%

clc
clear all
close all

mupp=10.1;
scaleImage=40; %scale of image, light
jump= 20;

Filename='test1604_43CM';
info=dir([Filename '\*.cih']);
INFO=readtable([Filename '\ info.name'],'FileType','text');
liste=dir([Filename '\*.raww']) % Listing. raww files

%%
B(:,:)=0;
start_frame=1;
sep=200; %µs
i=start_frame;
%Resolution of image
height=512 %str2num(INFO{20,2}{1})
width=1024 %str2num(INFO{21,2}{1})
t = 0:0.1:2*pi;

ParticleData=[0,0,0,0,0,0,0,0,0,0,0];

while i<115 %antall bilder

    ex=0;
    DATA=[0,0,0,0,0,0,0,0,0,0];

    file1 = liste(i).name;
    fid1 = fopen([Filename '\ file1], 'r'); %open file
    x1 = fread(fid1, [height*width], '*uint16'); % Read binarydatatodouble
    fclose ('all');

    file2 = liste(i+1).name;
    fid2 = fopen([Filename '\ file2], 'r'); %open file
    x2 = fread(fid1, [height*width], '*uint16'); % Read binarydatatodouble
    fclose ('all');

    [I0] = reshape(x1(1:end),[height width]); % Red channel
    [I1] = reshape(x2(1:end),[height width]); % Red channel
    figure(1),
    while ex<1

```

```

p1 = DATA(:,1:2); % First Point
p2 = DATA(:,3:4); % Second Point
dp = (p2-p1).*1; % Difference

imshow(uint16(I0*scaleImage))
hold on
text(50,50,'1','Color','r','FontSize',24)
quiver(p1(:,1),p1(:,2),dp(:,1),dp(:,2),0,'Color','b')

if size(DATA,1)>1
    for j=1:size(DATA,1)

        x=DATA(j,9)./2./mupp.*cos(t);
        y=DATA(j,9)./2./mupp.*sin(t);
        plot(x+p1(j,1),y+p1(j,2),'Color','r')
    end
end
[x1,y1]=ginput(1)
plot(x1,y1,'+')

[x2 y2]=ginput(1);
plot(x2,y2,'+')
center=[x1-(x1-x2)./2 y1-(y1-y2)./2];
r=sqrt(((x1-x2)./2)^2+((y1-y2)./2)^2);
x = r*cos(t);
y = r*sin(t);
plot(x+center(1),y+center(2),'Color','r')

pause(0.1)
imshow(uint16(I1*scaleImage))
text(50,50,'2','Color','r','FontSize',24)
quiver(p1(:,1),p1(:,2),dp(:,1),dp(:,2),0,'Color','b')
plot(x+center(1),y+center(2),'Color','r')
for j=1:size(DATA,1)

    x=DATA(j,9)./2./mupp.*cos(t);
    y=DATA(j,9)./2./mupp.*sin(t);
    plot(x+p1(j,1),y+p1(j,2),'Color','r')
end
[x3,y3]=ginput(1);

if or(y1>1000,y3>1000)
    ex=1;
elseif or(x1<10,x3<10)
    ex=1;
    i=i+1;
    ParticleData=[0,0,0,0,0,0,0,0,0,0];
    DATA=[0,0,0,0,0,0,0,0,0,0];

else
    mov=[x3,y3]-center;
    v=sqrt(mov(1).^2+mov(2).^2).*mupp./sep;

    if and(mov(1)<=0,mov(2)<=0)
        dirdeg=-asin(mov(2)/sqrt(mov(1).^2+mov(2).^2))*180/3.14;
    end
end

```



```

elseif and (mov (1)>0,mov (2)<=0)
dirdeg=180+asin (mov (2)/sqrt (mov (1) .^2+mov (2) .^2) ) *180/3.14;

elseif and (mov (1)>0,mov (2)>0)
dirdeg=180+asin (mov (2)/sqrt (mov (1) .^2+mov (2) .^2) ) *180/3.14;

elseif and (mov (1)<=0,mov (2)>0)
dirdeg=360-asin (mov (2)/sqrt (mov (1) .^2+mov (2) .^2) ) *180/3.14;

end

data=[center (1) ,center (2) ,x3,y3,mov,i,v,r.*2.*mupp,dirdeg];

DATA=[DATA;data];

end
no=(size (ParticleData,1)+size (DATA,1)-1)
if no>100
ex=1;
i=1000;
close all
end
end
if sum (DATA (:,1))>0
ParticleData=[ParticleData;DATA];
ParticleData=ParticleData (find (ParticleData (:,1)),: )
end

[d10,d32,vma,avdir] = SauterMean (ParticleData);
%%% eksempel på hvordan lagre
%%data=[center (1) ,center (2) ,x3,y3,mov,i,v,r.*2.*mupp,dirdeg];
sav=[Filename '.mat'];
save (sav,'ParticleData');%%%%%%%%%%
load ('2021MaleneDATA.mat')
i=i+jump;

end
props=[d10 d32 vma avdir]
PROPS=[PROPS;props];
%%%%%%%%[P100 T0001 d10 d32 vma average_dir]%%%%%%%%%%
save ('2021Mat','PROPS')

```

```

%%%%%%%%%%%%%%%%%%%%%%%%%%%%%%%%%%%%%%%%%%%%%%%%%%%%%%%%%%%%%%%%%%%%%%%%
% % Sauter mean - code % %
% % Created by Joachim Lundberg April 2021

function [d10 d32 vma avdir] = SauterMean(ParticleData)
%SAUTERMEAN Summary of this function goes here
% Detailed explanation goes here

d=ParticleData(find(ParticleData(:,8)),9);
v=ParticleData(find(ParticleData(:,8)),8);

ang=(ParticleData(:,10));
angmax=max(ang);
angmin=min(ang);
if and(angmax>270,angmin<90);
    x=sum(ParticleData(:,5));
    y=sum(ParticleData(:,6));
    if and(x<=0,y<=0)
        avdir=atan(y/x)*180/3.14;

    elseif and(x>0,y<=0)
        avdir=180-atan(-y/x)*180/3.14;

    elseif and(x>0,y>0)
        avdir=180+atan(y/x)*180/3.14;

    elseif and(x<=0,y>0)
        avdir=360-atan(y/-x)*180/3.14;

    end

else
    avdir=mean(ang);
end

d10=sum(d)./sum(size(d,1));
d32=sum(d.^3)./sum(d.^2);
vma=sum(d.^3.*v)./sum(d.^3);
end

```

# Appendix F

Table 0.1: Data from the image processing.

C 1	C 2	X3	Y3	x	y	Im no	Vel. [m/s]	Diameter [ $\mu$ m]	Dir.
404,63	712,87	381,27	706,73	-23,36	-6,15	21,00	1,22	24,83	14,75
445,20	164,61	424,30	156,01	-20,90	-8,61	41,00	1,14	24,83	22,39
354,23	392,03	338,25	380,97	-15,98	-11,06	41,00	0,98	24,83	34,71
335,79	857,93	312,43	851,78	-23,36	-6,15	41,00	1,22	24,83	14,75
463,64	301,06	446,43	290,00	-17,21	-11,06	1,00	1,03	24,83	32,75
434,13	180,59	413,23	171,99	-20,90	-8,61	41,00	1,14	24,83	22,39
405,86	41,68	370,21	33,08	-35,65	-8,61	41,00	1,85	24,83	13,58
71,49	380,97	46,91	374,82	-24,59	-6,15	41,00	1,28	24,83	14,04
92,39	739,92	73,95	737,46	-18,44	-2,46	61,00	0,94	24,83	7,60
236,83	341,63	227,61	340,40	-9,22	-1,23	61,00	0,47	27,76	7,60
277,40	787,86	271,87	787,86	-5,53	0,00	81,00	0,28	27,76	0,00
242,36	274,63	231,30	274,02	-11,06	-0,61	21,00	0,56	37,25	3,18
423,07	262,34	404,63	255,58	-18,44	-6,76	1,00	0,99	37,25	20,15
429,22	588,10	407,09	578,88	-22,13	-9,22	1,00	1,21	37,25	22,63
140,33	57,05	118,20	51,52	-22,13	-5,53	21,00	1,15	37,25	14,04
78,87	476,24	70,26	465,79	-8,61	-10,45	41,00	0,68	37,25	50,55
486,99	155,39	462,41	152,32	-24,59	-3,07	61,00	1,25	37,25	7,13
247,28	127,12	230,07	127,73	-17,21	0,61	81,00	0,87	37,25	357,95
137,87	495,90	128,04	498,98	-9,83	3,07	81,00	0,52	37,25	342,64
448,88	331,18	440,28	329,34	-8,61	-1,84	101,00	0,44	37,25	12,10
389,88	288,15	371,44	277,71	-18,44	-10,45	41,00	1,07	37,25	29,55
50,59	170,14	30,92	176,90	-19,67	6,76	81,00	1,05	37,25	341,02
83,78	269,71	71,49	274,02	-12,29	4,30	101,00	0,66	37,25	340,70
148,94	457,80	148,94	460,87	0,00	3,07	101,00	0,16	37,25	269,95
117,59	214,40	100,99	215,01	-16,60	0,61	61,00	0,84	39,26	357,88
279,24	101,92	257,11	82,25	-22,13	-19,67	1,00	1,50	49,66	41,65
284,16	199,03	257,11	199,03	-27,04	0,00	1,00	1,37	49,66	0,00
423,07	505,12	420,61	495,29	-2,46	-9,83	61,00	0,51	49,66	76,00
321,04	489,14	311,20	487,91	-9,83	-1,23	61,00	0,50	49,66	7,13
108,37	451,04	81,33	449,81	-27,04	-1,23	61,00	1,37	49,66	2,60
420,61	238,37	400,94	240,83	-19,67	2,46	81,00	1,00	49,66	352,87
223,92	646,49	215,32	648,95	-8,61	2,46	81,00	0,45	49,66	344,05
46,91	608,38	35,84	608,38	-11,06	0,00	81,00	0,56	49,66	0,00
255,89	735,00	242,36	748,52	-13,52	13,52	81,00	0,97	49,66	314,98
323,50	207,64	308,74	210,09	-14,75	2,46	101,00	0,76	49,66	350,53
327,18	705,50	334,56	706,73	7,38	1,23	101,00	0,38	49,66	189,47
96,08	110,52	81,33	101,92	-14,75	-8,61	1,00	0,86	49,66	30,27
311,20	180,59	311,20	174,44	0,00	-6,15	81,00	0,31	49,66	90,05
217,78	290,00	206,71	291,23	-11,06	1,23	101,00	0,56	49,66	353,66
191,35	126,50	164,92	138,80	-26,43	12,29	81,00	1,47	51,19	335,04



# Appendix G

Date:		T <sub>env</sub> :			RH:	
ID	What to measure?	Tool/ parameter used	Hypothesis	Variables	Values	As expected?
1.1	Effluent air temperature	Pressure sensor	<i>If the influent compressed air pressure increases, the effluent air temperature is expected to decrease regarding the isothermal expansion</i>	Compressors discharged air		
1.2	Condensation and freezing in the nozzle	Temperature out from compressor	<i>If the compressor's effluent temperature is not below the temperature at which the airflow is discharged, condensation is expected to occur.</i>	-		
1.3	The temperature of the spray	Thermographic camera	<i>If the displacement of the droplets increases away from the nozzle, then the temperature of the droplets is expected to decrease.</i>	Distance from nozzle		
1.4	The temperature of snow product	Thermographic camera and watch	<i>If the snow produced is exposed to the surrounding with a time t, then the temperature of the product snow is expected to decrease</i>	Time and weather conditions		
1.5	Water quality and nucleus content	Microscope, lab	<i>If the water supplied to the snow system contain a natural nucleus, then the snow formation is expected to increase</i>			
1.6	Change of relative humidity	Hygrometer	<i>If the water mass flow is increased, then the relative humidity of the mixed air is expected to increase.</i>	Pump frequency		

1.7	Width of spray and droplet diameter	Laser /High-speed camera and measuring tape	<i>If the water's mass flow is kept constant and the airflow is increased, then atomization of water droplets is expected to increase</i>	Influent air pressure		
				Constant value of water		
1.8	Length of spray	Measuring tape	<i>If the airflow is kept constant and the water flow increases, then the spray's displacement is expected to increase.</i>	Influent air pressure		
				Constant value of water		
				Constant water flow		

*Product measurement*

Product	
Production time:	
Volume produced:	
Density:	
Snow crystal shape:	

# Appendix H

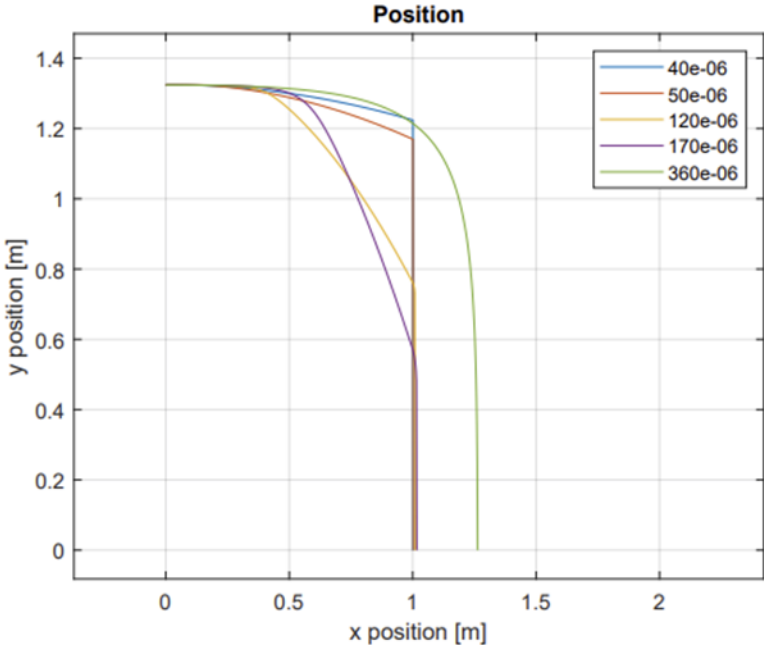


Figure 0.1: Velocity vs. distance, assuming mixed air velocity equals zero beyond 1 m

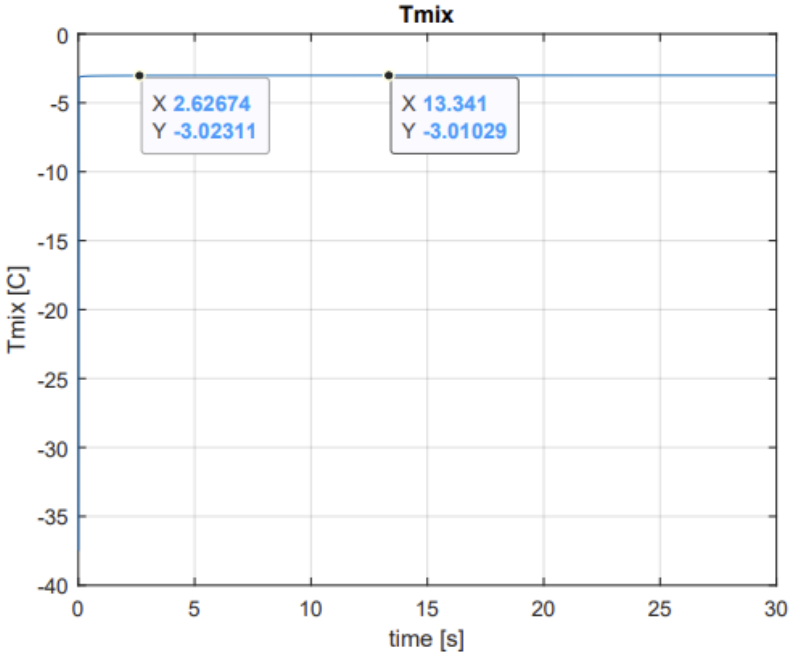


Figure 0.2: Chang of mixed air temperature with time

# Appendix I

ID	Task Mode	Task Name	Duration	Start	Finish
1	👤	1st meeting with supervisor	0 wks	Thu 07.01.21	Thu 07.01.21
2	👤	Deadline for signing final project description	0 wks	Mon 01.02.21	Mon 01.02.21
3	👤	<b>Introduction</b>	2 wks	Mon 01.03.21	Fri 12.03.21
4	👤	<b>Theory</b>	15,2 wks	Thu 07.01.21	Thu 22.04.21
5	👤	Calculate effluent nozzle parameter	4 wks	Thu 07.01.21	Wed 03.02.21
6	👤	Calculate increase in RH	2 wks	Wed 27.01.21	Wed 10.03.21
7	👤	Calculate moisture content in airflow	1 wk	Thu 07.01.21	Wed 13.01.21
8	👤	Describe snow quality measurement	2 wks	Thu 07.01.21	Wed 20.01.21
9	👤	Explain natural snow phenomenon	2 wks	Thu 07.01.21	Thu 04.03.21
10	👤	Calculate the droplet distribution	1,2 wks	Fri 26.02.21	Fri 05.03.21
11	👤	Calculate change in airflow velocity	0,5 wks	Mon 08.03.21	Wed 10.03.21
12	👤	Calculate change in surrounded air velocity	0,5 wks	Wed 10.03.21	Fri 12.03.21
13	👤	Calculate change in droplet velocity	0,5 wks	Mon 15.03.21	Wed 17.03.21
14	👤	Determine a scientific model for droplet change with respect to heat transfer	4 wks	Wed 17.03.21	Wed 14.04.21
15	👤	Determine snow crystal growth	0,5 wks	Fri 09.04.21	Tue 13.04.21
16	👤	Determine the probability for collision between droplets	1 wk	Tue 13.04.21	Tue 20.04.21
17	👤	Calculate change of relative humidity	0,6 wks	Tue 20.04.21	Thu 22.04.21
18	👤	Theory document	14,6 wks	Tue 12.01.21	Thu 22.04.21
19	👤	Test experiment	0 wks	Thu 11.02.21	Thu 11.02.21
20	👤	1st formal meeting	0 wks	Fri 26.02.21	Fri 26.02.21
21	👤	2nd formal meeting	0 wks	Tue 30.03.21	Tue 30.03.21
22	👤	<b>Method</b>	9 wks	Fri 26.02.21	Thu 29.04.21
23	👤	Create test matrix	1 wk	Fri 26.02.21	Thu 04.03.21
24	👤	Create hypothesis	1 wk	Fri 26.02.21	Thu 04.03.21
25	👤	Prepare for experiment	0 wks	Wed 10.03.21	Wed 10.03.21
26	👤	Experiment in Porsgrunn	0,2 wks	Fri 12.03.21	Fri 12.03.21
27	👤	Experiment in Arabygdli	0,4 wks	Thu 18.03.21	Fri 19.03.21
28	👤	Experiment in Kviteseid	0,2 wks	Sun 21.03.21	Sun 21.03.21
29	👤	Image Processing	0,6 wks	Thu 22.04.21	Sun 25.04.21
30	👤	Equipment list	0,5 wks	Thu 11.03.21	Mon 15.03.21
31	👤	Procedure	0,7 wks	Thu 11.03.21	Tue 23.03.21
32	👤	Method document	1 wk	Fri 23.04.21	Thu 29.04.21
33	👤	<b>Result</b>	1 wk	Fri 30.04.21	Thu 06.05.21
34	👤	Decide presentation date	0 wks	Mon 26.04.21	Mon 26.04.21
35	👤	<b>Discussion</b>	0,5 wks	Fri 07.05.21	Tue 11.05.21
36	👤	<b>Conclusion</b>	0,2 wks	Fri 07.05.21	Fri 07.05.21
37	👤	<b>References</b>	0,2 wks	Mon 10.05.21	Mon 10.05.21
38	👤	<b>Plagiarism</b>	0,1 wks	Tue 11.05.21	Tue 11.05.21
39	👤	<b>Proofreading</b>	1 wk	Tue 11.05.21	Tue 18.05.21
40	👤	Submit thesis (14:00)	0 wks	Wed 19.05.21	Wed 19.05.21
41	👤	<b>Presentation</b>	3,5 wks	Wed 19.05.21	Fri 11.06.21
42	👤	Animation/ movie	1,5 wks	Tue 11.05.21	Thu 20.05.21
43	👤	EXPO	0 wks	Tue 25.05.21	Tue 25.05.21
44	👤	Power point	1 wk	Wed 19.05.21	Tue 25.05.21
45	👤	Final presentation	0 wks	Fri 11.06.21	Fri 11.06.21

